MAPPER lithography

TU Delft Delft University of Technology

Department of Precision and Microsystems Engineering

Dynamic analysis of a piezoelectric ultrasonic motor

With application to the design of a compact high-precision positioning stage

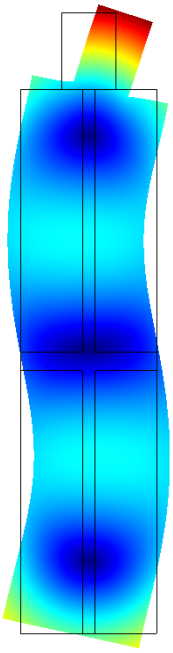

Name: Teunis van Dam

Report no: ME 11.036
Coach: R. Ellenbroek
Professor: prof. ir. R. H. Munnig Schmidt
Specialization: Mechatronics
Type of report: Masters Thesis
Date: Delft, November 22, 2011

Preface

This thesis describes the work I have done at Mapper Lithography B.V. in Delft, as a final project for my masters Precision and Microsystems Engineering at Delft University of Technology, faculty 3mE.

This project is part of the process of designing a high-precision linear positioning stage for a wafer scanner using electron beam lithography. The first part of my work is focused on the conceptual design of this stage, in which choosing the actuator type plays a dominant role. The second and largest part is focused on detailed analysis of the dynamic behavior of the selected actuator, a piezoelectric ultrasonic motor, by building a simulation model of the motor and validating this model by experiments.

I want to thank my professor, Robert Munnig Schmidt, and my supervisor at Mapper Lithography, Rogier Ellenbroek, for their support and valuable feedback on my work. Furthermore I would like to thank my design leader at Mapper Lithography, Jerry Peijster, and my other colleagues, for granting me this opportunity and for the pleasant cooperation.

Teunis van Dam

Contents

1 Introduction **6**
- 1.1 General introduction . . . 6
- 1.2 Machine description and problem statement . . . 6
- 1.3 Overview of contents . . . 7

2 Stage requirements **9**
- 2.1 Functionality . . . 9
- 2.2 Environment . . . 11
- 2.3 Miscellaneous . . . 11

3 Design concepts **12**
- 3.1 Basic alternatives . . . 12
- 3.2 Main concepts . . . 13
- 3.3 Concept choice . . . 16

4 Piezoelectric motors **18**
- 4.1 Introduction and classification . . . 18
- 4.2 Characteristics of linear ultrasonic motors . . . 20

5 Simulation model **23**
- 5.1 Introduction . . . 23
- 5.2 Method . . . 24
- 5.3 Results . . . 29
- 5.4 Discussion . . . 34

6 Measurements **37**
- 6.1 Experimental setup description . . . 37
- 6.2 Measurement description and results . . . 39
- 6.3 Interpretation . . . 43
- 6.4 Model validation . . . 44

7 Conclusion and recommendations **48**
- 7.1 Conclusion . . . 48
- 7.2 Recommendations . . . 48

A Literature study to topics related to compact stage design **51**
- A.1 Contents . . . 51
- A.2 Important issues and limitations in high vacuum environment . . . 51
- A.3 Actuators in high vacuum environment . . . 52
- A.4 Feedthrough mechanisms . . . 53
- A.5 Transmission elements . . . 58

A.6 Linear guidings in vacuum environment . . . 61
A.7 Errors and vibrations in high precision positioning systems in vacuum . . . 61
A.8 Magnetic fields . . . 64

B Duty cycle calculation regarding overheating 69

C Dimensions and material properties for the simulation model 71
C.1 Dimensions . . . 71
C.2 Material properties . . . 71

D Detailed model description 73
D.1 Notation . . . 73
D.2 Unconstrained equations of motion . . . 73
D.3 Constraints and contact model . . . 77
D.4 Solving the model . . . 81
D.5 Postprocessing . . . 83

E Extended resonance analysis 85
E.1 Influence of support parameters on resonance frequency . . . 85
E.2 Input sensitivity at different support parameters . . . 85
E.3 Conclusion . . . 87

Bibliography 89

Chapter 1

Introduction

1.1 General introduction

Wafer scanners are used in photolithography to write complicated 2D patterns on a silicon wafer in order to fabricate microchips. In this process, a layer of photoresist material is exposed to the optical image of a mask that contains the desired pattern. Removing the material only at the exposed area's by chemical etching and repeating this process multiple times leads to complicated semi-3D structures that give the chip its functionality [1].

An alternative to this process is electron beam lithography: instead of light, electron beams are used to expose the wafer, which results in a very different process. In e-beam lithography the electron beams expose the wafer 'pixel by pixel', similar to a TV-tube. In this process, actively controlling the electron beams allows the machine to write 'black' and 'white' pixels according to the desired pattern, so that no mask is needed. If large area's are to be exposed, the wafer is moved relative to the electron beam by a high-precision positioning stage.

E-beam lithography has two main advantages over traditional lithography. In the first place, the wavelength of electrons is much smaller than that of light waves, so the features of the pattern on the wafer can be scaled down to a smaller size. In the second place, the costs for creating a mask are very high, so especially in small batch production, where these costs are divided over a small amount of products, maskless lithography provides a significant cost reduction.

The main limitation of e-beam lithography is the limited throughput: compared to photolithography it takes a very long time to expose a certain wafer area. Therefore this technique is not yet used in mass production of integrated circuits. It is, however, applied in the production of the masks used for photolithography and in low-volume production of integrated circuits. Currently, high-throughput e-beam lithography machines are in development that use a large amount of parallel electron beams to allow higher throughput rate, for instance at the Dutch company Mapper Lithography B.V. [2]. These developments show that in a next generation of wafer scanners the e-beam technology should be able to compete with the conventional technology.

1.2 Machine description and problem statement

The required functionality of the high-throughput electron beam wafer scanner developed at Mapper Lithography B.V. is as follows:

- The machine should be able to produce integrated circuits with a maximum writing error of 7 nm.
- A single machine should reach a throughput rate of at least 10 circular wafers with a diameter of 300 mm per hour.

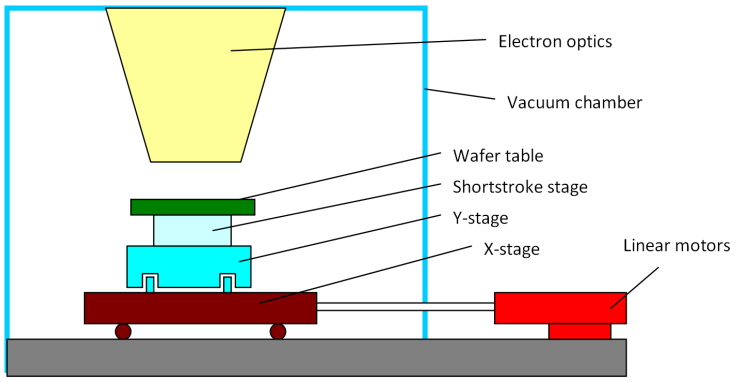

Figure 1.1: Schematic drawing of the e-beam lithography machine.

- The entire machine should fit inside a square floor area of 1×1 m .

The two main parts of the machine are the electron optics, that generate and control the electron beams, and the wafer positioning system (WPS). In Figure 1.1 a schematic drawing of the machine is shown. The WPS has the task of positioning the wafer under the stationary electron column. During the exposure, the wafer is moved with a constant velocity in the 'scanning direction' over the full length of the wafer, so that a small strip of the wafer area is exposed. This is repeated to expose the entire wafer area. The maximum 3σ-error on the wafer position during the scanning motion is 1.65 nm.

The wafer positioning system consists of four subsystems:

1. The X-stage: the linear stage that allows the wafer to move in the scanning direction.
2. The X-drives: two linear electric motors that drive the X-stage.
3. The Y-stage: the linear stage that allows the wafer to move in the lateral direction. The actuators are integrated in the stage and form no separate subsystem.
4. The shortstroke stage. This is a 6-DOF short-stroke positioning system, placed between the longstroke stage and the wafer table to compensate for disturbances in the longstroke stage position. This is necessary since the longstroke stage itself is not able to provide the required position accuracy.

Both the electron optics and the wafer positioning are placed inside a vacuum chamber with 10^{-6} mbar air pressure which is required for the electron optics module. This vacuum chamber contains a magnetic shield to reduce the magnetic fields inside the machine, that affect the position stability of the electron beams, to the order of 1 nT. The front side of the vacuum chamber (left in the picture) contains a door that can be opened to do servicing.

In the current prototype of the longstroke stage, the X-stage is driven by two linear electric motors and the Y-stage by piezoelectric ultrasonic motors. The linear electric motors are located outside the main vacuum chamber, in separate chambers with somewhat lower vacuum, and two driving rods penetrating the main vacuum chamber wall feed through the linear motion. In this way, the drives are outside the 1×1 m floor area taken by the rest of the machine so the machine doesn't fulfill the footprint requirement. Therefore, a new X-stage design is required, in which the actuators are placed either in a recess on the outside of the main vacuum chamber, or completely inside, so that the footprint of the entire machine doesn't exceed the 1×1 m floor area.

1.3 Overview of contents

The first part of this report deals with the process of choosing a basic concept for the positioning stage. In Chapter 2, the requirements for the stage, as set by the company, are given and explained from the required

functionality of the entire machine. In Chapter 3, several alternatives are presented for the most important components of the stage, leading to a number of design concepts. A choice is made for a concept in which a piezoelectric ultrasonic motor is used to drive the stage.

The second part focuses on the piezoelectric motor. In Chapter 4, the working principle and main limitations of piezoelectric motors are explained. In Chapter 5, a specific motor is chosen and a simulation model is built to further investigate the characteristics of this motor. The used method is explained and results of the simulations are given. Chapter 6 focuses on validation of the simulation model by doing measurements on an experimental setup that is designed and built for this purpose.

Finally, Chapter 7 contains some concluding remarks and recommendations.

Chapter 2

Stage requirements

In this chapter the most important requirements for the X-stage are given and explained. A full list of requirements and conditions can be found in Table 2.1.

2.1 Functionality

Stroke The X-stage is responsible for positioning the wafer under the electron beams in the scanning direction. The wafer is a circular plate with a diameter of 300 mm and the electron column is a 26x26 mm square, so in order to expose the entire wafer the stroke should be at least 326 mm. In order to allow acceleration and deceleration at the beginning and end of the run, the minimum required stroke is 340 mm.

Duty cycle The entire surface of the wafer is divided in 10 'lanes'. At each lane, the machine makes two exposure scans, first the 'main scan' to expose the wafer, and after that the 'redundancy scan' to cover possible gaps left after the first exposure. Exposure can only be done in a single movement direction. Therefore the stage should make two back-and-forth movements per lane, which means 40 full-stroke travels, about 13 m traveled distance, per wafer. On top of the scanning movements, the duty of the stage contains additional movements for instance for calibrations or wafer loading, so that the traveled distance is about 15 m per wafer. The required throughput is six wafers per hour.

Velocity and acceleration The velocity of the wafer during the exposure scan is determined mostly by the performance of the electron optics module and should be 75 mm/s. In order to reach the desired wafer throughput rate, the stage should be able to move with at least 200 mm/s during return movements and additional movements. Because of the smooth scanning motion and relatively low velocity, accelerating and decelerating the stage is only a small part of the duty and therefore the required acceleration is not very high: 0.3 m/s^2.

Position stability The position stability of the longstroke stage during constant-velocity scan should be such that the shortstroke stage is able to compensate them to acquire the final 1.65 nm 3σ positioning accuracy. With the current shortstroke stage specifications, this means the maximum 3σ-error on the X-stage position during the scan is 30 µm. Furthermore, it is required that stage should reach 10 µm static position accuracy.

Tolerances The shortstroke stage should be able to compensate for production and mounting tolerances in the longstroke stage position and orientation in the Z, RX, RY and RZ directions, which are not degrees of freedom of the longstroke stage. With the current shortstroke stage design, these tolerances are 50 µm in Z-direction and 200 µrad in all rotational directions.

Requirements	
Stroke	340 mm
Velocity	200 mm/s
Acceleration	0.3 m/s^2
Static positioning accuracy	10 µm
Maximum 3σ-error on position during scan	30 µm
3σ-value of horizontal component magnetic field due to LoS at electron column	< 2 nT, averaged over the height of the column
No magnetic materials used	-
Maximum power consumption	500 W
Lifetime	3 years; 3942 km of travel
Tolerances ΔZ, ΔRX, ΔRY, ΔRZ	50 µm; 200 µrad (3x)
Service	All service should be done from the front side of the machine
Conditions	
Duty cycle	15 m traveled distance per wafer, 6 wafers per hour
Velocity during scan	75 mm/s
Payload	75 kg
Pressure inside vacuum chamber	10^{-6} mbar
Height of the wafer table above floor level	900 mm
Footprint of the entire machine	1×1 m

Table 2.1: Complete list of X-stage requirements.

Payload With the current design of the Y-stage, shortstroke stage and wafer table, the payload for the X-stage is 75 kg.

Lifetime MAPPER requires the lifetime of the stage to be 3 years. With 15 m traveled distance per wafer, 10 wafers per hour and assuming 24/7 operation during the entire year, the X-stage should be able to make about 3942 km of travel.

2.2 Environment

Vacuum compliance The pressure inside the vacuum chamber is 10^{-6} mbar. While the machine is in operation, the vacuum environment is continually pumped to remove gases that result from 'outgassing' of materials. Therefore, a certain outgassing budget is given to the longstroke stage, including leakage of air through a feedthrough mechanism, if included in the design. The same holds for particle generation. Exact values for the maximum outgassing and particle generation rates are not known at this moment.

Magnetic fields Since the electron beams are deflected by magnetic fields, the horizontal component of the magnetic field at the electron beam column above the wafer are restricted to assure the final writing accuracy. Therefore the stage should not contain magnetic materials and should not produce magnetic stray fields more than 2 nT at the location of the electron beams in horizontal direction.

2.3 Miscellaneous

Volume In the process of designing the MAPPER machine, each of the modules 'claims' a part of the volume inside the vacuum chamber. No strict volume claim can be made for the X-stage yet, because the layout of the machine is dependent on whether for instance the actuators will be placed outside the chamber (as in the current design) or inside, and because specifications of some other parts of the machine are yet unknown. However the following things are stringent:

- The footprint of the entire machine: about 1 m^2.
- The height of the wafer table above floor level: 90 cm.

Servicing Since the MAPPER tools will be positioned close to each other in 'matrix'-formation in the cleanroom, they are accessible from only the front side. Therefore servicing for the longstroke stage, including the parts that are positioned outside the vacuum chamber, should be possible from the front side of the machine.

Chapter 3

Design concepts

In this chapter, several design concepts are defined and considered. This is based on a literature study to topics related to the design of high vacuum, high precision, non-magnetic positioning stages, of which a more extended report can be found in Appendix A.

3.1 Basic alternatives

In creating design concepts for the stage, two key characteristics are defined that largely determine the design:

1. The placement of the actuators: either inside or outside the vacuum chamber. This determines if a feedthrough mechanism is needed and what type of actuators can be used.
2. The type of actuators. The performance of the stage strongly depends on the actuator, and the choice between linear or rotary actuator determines if a transmission is needed.

3.1.1 Actuators inside the vacuum chamber

Generally speaking this is the most advantageous alternative, since it would avoid a feedthrough with its related complexity. Furthermore, in case of maintenance, the full stage can be removed and replaced, which makes servicing easier compared to a concept in which the actuators are outside the chamber and mechanically connected to the stage via a feedthrough. Several types of actuators can be considered for a stage inside the vacuum chamber.

Linear or rotary electric motors Electric motors are by far the most conventional solution [1]. However, the inevitable magnetic stray fields produced by electric motors form a big problem when they are placed inside the magnetic shielding of the vacuum chamber. No electric motors are found that comply with the strict requirements on the generation of magnetic stray fields and usage of magnetic materials.

Piezoelectric motors Piezoelectric ultrasonic motors are suitable for in vacuum environments and don't produce significant magnetic stray fields. Although not as common as electric motors, they are sometimes used in high-precision positioning stages [3]. Both linear and rotary piezoelectric motors are available on the market, but for a linear stage, the linear motors are the most suitable since a transmission mechanism would be needed when using a rotary motor.

Hydraulic or pneumatic actuators Although hydraulic actuators are known to be used for positioning applications several decades ago [1], they are generally considered as far from ideal due to for instance problems with sealing and the risk of contamination when a part of the hydraulic circuit breaks. Only one

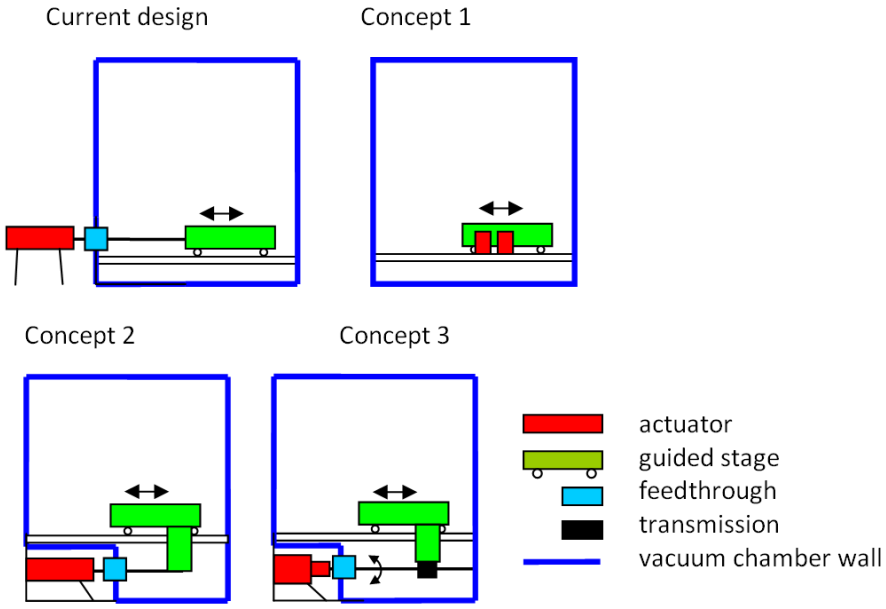

Figure 3.1: Schematic drawings of the current solution and three concepts.

more or less recent development of a precision stage with hydraulic actuators is found [4], but no indication could be found that this drive is ever used in reality.

For pneumatic actuators, the risk of leakage is less an issue since gas can be pumped away without leaving significant contamination. However, pneumatic actuators suffer from low stiffness due to the compressibility of the gas and high friction due to the sealing of the cylinder. Therefore they are not suitable for fast and precise motion control; no examples are found of pneumatic actuators used in precision stages.

3.1.2 Actuators outside the vacuum chamber

Placing the actuators outside the vacuum chamber has the disadvantage that a feedthrough mechanism is needed, and it makes servicing more complex. However, the advantage is that the use of electric motors is a realistic option, since due to the magnetic shield of the vacuum chamber only a fraction the magnetic stray fields produced by the motors are felt inside the chamber. Both linear and rotary motors could be used.

3.2 Main concepts

From the basic design alternatives, three possible concepts arise. The first is a stage that is located entirely inside the vacuum chamber, driven by linear piezoelectric motors. The second is the concept on which the current prototype of the stage is based, namely a stage driven by linear electric motors that are placed outside the main vacuum chamber. The third is a stage driven by a normal rotary electric motor placed outside the chamber. In Figure 3.1 schematic drawings are shown of each of the concepts and the current design. Dimensions and geometries are not realistic, they are just meant to give a basic impression on what the designs may look like. It is beyond the scope of this research to make a detailed design for each of the concepts, but each of them is discussed in some detail below.

3.2.1 Concept 1: stage driven by linear ultrasonic motors

Ultrasonic motors are motors that convert ultrasonic structural vibrations, generated by a piezo-transducer, to linear motion [5]. Simply speaking, the motor structure is excited in a resonance on an ultrasonic frequency

such that it makes a 'stepping motion' against a flat counter-surface, leading to relative motion between the motor and the counter-surface when integrated in a linear stage. Individual steps are small but due to the high frequency, velocities of several hundreds of mm/s can be reached.

Linear ultrasonic motors should be able to provide the required performance. As an example, the specifications of the ultrasonic motor manufactured by Nanomotion [6] are taken. The maximum velocity is 250 mm/s, and the stall force of a motor with a single stepper element is about 4N. This stall force is not enough to accelerate the stage of 75 kg with 0.3 m/s^2 (22.5 N), but motors with multiple stepper elements are available and the use of several motors in parallel configuration is supported.

The frequency of the vibrations in the Nanomotion motor is about 40 kHz. Due to this high frequency, the velocity ripple due to the vibrational actuation method is no threat. As an example, if the motors exerts harmonic forces with an amplitude of 50 N on a stage with a mass of 1 kg, the resulting harmonic position error is:

$$e = \frac{50 \text{ N}}{1 \text{ kg} \cdot (2\pi \cdot 40000 \text{ Hz})^2} \approx 0.8 \text{ nm}$$

This is far below the required value for the X-stage, so provided the stage itself doesn't contain too much unwanted resonance at the drive frequency, the motors will provide smooth motion.

With the right driver electronics, the motor has an almost linear signal-to-force characteristic, which makes it easily integrable in a servo system. Also the motors are very compact: a motor with 8 stepper elements (32 N stall force) is a box of $42 \times 47 \times 24$ mm that weighs 170 grams. The specified lifetime is 20,000 hours, enough for 3 years of operation with the required duty, although in reality cases are known in which the motors began malfunctioning long before reaching the specified lifetime.

There are two big disadvantages to this concept. In the first place, the frictional contact between the vibrating structure and the flat counter surface leads inevitably to wear and therefore particle generation. There are no specifications on particle production and knowledge about this in literature is very limited, but based on the little information that could be found, particle generation is possibly high enough to seriously contaminate the machine. The second issue is heat production: ultrasonic motors are known to have problems with losing the generated heat. Specifications of the Nanomotion motors require a certain cooling down time, limiting the duty cycle of the motors dependent on the velocity and delivered force. In Appendix B the required duty cycle for the X-stage is compared with the Nanomotion specifications of maximum duty cycle. The required duty will be close to the maximum allowed duty, which means overheating is a serious issue.

A general disadvantage of using ultrasonic motors is the fact that these type of motors is quite new and therefore not yet very often used in industrial applications, which means the available theoretical knowledge and practical experience is limited. In known cases where ultrasonic motors are used for positioning stages, often unexpected behavior is encountered.

3.2.2 Concept 2: stage driven by linear electric motor outside the vacuum chamber

This is the alternative that is currently used in a prototype of the stage. Linear electric motors are very suitable for high precision linear positioning and are the most commonly used in semiconductor industries. Linear electric motors are in general able to deliver the required performance in terms of force, stroke, velocity and accuracy.

A disadvantage of this alternative is the need for a linear feedthrough mechanism: sealing a linear shaft is more complex than a rotary shaft. In the current prototype, a non-hermetic seal is used with a differential pump to provide the pressure gap, but overcoming the full pressure difference between atmosphere and vacuum is not possible so the actuators are placed in a separate environment containing a lesser vacuum. Several alternatives exist for the pumped feedthrough [7]. One is a hermetic bellows-sealed feedthrough, but this is in general not suitable for continuous-moving applications due to the limited lifetime of the bellows, and no such feedthrough is found on the market that is able to provide the required travel length. Another alternative is a hermetic feedthrough with permanent-magnet coupling between inner and outer shaft through a thin wall, but the limited stiffness of this coupling provides problems with dynamic behavior.

However, the biggest issue in this alternative is the dimensions of the design. A linear shaft should be put through the vacuum chamber wall. One end of the shaft is connected to the linear motor outside the chamber, while the other end is connected to the moving stage inside the chamber. This leads to a design in which the stage, feedthrough mechanism and linear motor are placed in one line (see Figure 3.1). A rough estimation of the necessary space is made:

- The length of a differentially pumped feedthrough mechanism is estimated on 100 mm excl. the wall thickness (see for instance specifications of systems manufactured by VG Scienta [8]) and more for other types.
- The length of a typical linear electric motor is estimated on 100 mm on top of the the travel length.
- The required travel length is 340 mm.
- The thickness of the vacuum chamber wall is 30 mm.

Based on these numbers, the total space needed is $2 \cdot 340 + 100 + 100 + 2 \cdot 30 = 940$ mm. This is already close to the maximum of 1 m, while no attention is yet given to a secondary vacuum chamber that might be necessary (as in the current design) or other parts of the machine that might interfere. Therefore it will be quite a challenge to design a stage according to this concept that fits within the required footprint[1]. This is exactly the problem with the current prototype.

In this concept, a recess is necessary on the outside of the chamber where the motor can be placed. This makes servicing from one side of the machine complicated.

3.2.3 Concept 3: stage driven by rotary electric motor outside the vacuum chamber

The advantage of using a rotary electric motor is that it is a very conventional solution, which means there is lots of experience in its use, and lots of them are available on the market which makes it easy to select one that fits the functional requirements. The disadvantage of this concept is the need for a feedthrough and transmission mechanism, which makes the design complicated and voluminous. It is possible either to place the transmission outside the vacuum chamber and use a linear feedthrough, or to place the transmission inside the chamber and use a rotary feedthrough. In the first case, the concept is practically the same as the previous concept, only with an actuator consisting of a rotary motor and transmission instead of a 'real' linear motor. Therefore only the second is discussed.

Rotary feedthrough mechanisms are more common than linear ones and several types are available in industry [7]:

- Feedthrough mechanisms that use deformable bellows to provide hermetic sealing. They are not designed for long-term continuous operation; the service lifetime is usually in the order of 10^6 revolutions. Assuming for instance a transmission with a ratio of 10 mm per revolution, about $4 \cdot 10^8$ revolutions would be necessary for the required travel within the servicing lifetime.
- Permanent magnet-coupling between inner and outer shaft. This has the drawbacks of magnetic stray fields close to an opening in the magnetic shield of the vacuum chamber and loss of stiffness due to the non-ideal magnetic coupling.
- Feedthroughs that use a ferro-fluid seal. Again a permanent magnet is needed 'inside' the chamber wall, but since it is a stationary field, this is not necessarily a problem.
- A differentially pumped feedthrough. Several differential stages are needed to get to the final pressure of 10^{-6} mbar (commercially available systems get to 10^{-2} mbar typically [8]).

For a transmission mechanism, lots of options are available, for example lead screws, ball screws, or rack-and-pinion combinations. However, few commercially available transmission mechanisms are found that are suitable for high-vacuum environment and none of them meets the requirements for lifetime and accuracy.

[1] At the moment of writing, the required stroke is changed to 390 mm, making this even more a challenge.

	Concept 1	Concept 2	Concept 3
Compactness	+	-	+-
Complexity	+	+-	-
Accuracy	+	+	+-
Vacuum compliance	+-	+-	-
Magnetic	+	+-	+-
Lifetime	+-	+-	+-
Risk of development	-	+	+-

Table 3.1: Concept comparison table.

One of the more promising alternatives is a ball screw specifically designed for high-vacuum applications, manufactured by NSK [9], but the lifetime of this mechanism is far too short. A simple friction-wheel transmission could be a solution, but wear in the frictional contact, leading to particle generation, is a drawback of this. Also, development of stages actuated by rotary motors and friction wheels in the early semiconductor industry problems with the dynamics because of the low-stiffness connection [1].

Just as the previous concept, servicing from one side of the machine is difficult due to the complicated vacuum chamber design.

3.3 Concept choice

The above concepts are compared according to the following criteria:

Compactness: this covers the expected volume taken by the design and the likeliness of exceeding the required maximum footprint.

Serviceability: this relates to the expected difficulty of servicing the system from only the front side of the machine.

Dynamic behavior: this covers the accuracy of the actuator and the possible problems in dynamic performance due to additional components.

Vacuum compliance: this relates to possible problems with outgassing, leakage or heat transport, and problems in finding the necessary vacuum-compatible components.

Magnetic: this relates to possible problems with magnetic stray fields and magnetic materials inside the vacuum chamber.

Lifetime: this relates to the possibility that the stage doesn't reach the required lifetime.

Risk of development: the risk that is taken when an experimental concept is chosen, of which knowledge and experience is yet limited.

The results are shown in Table 3.1. Since the concepts are not worked out into detailed designs, the comparison is partly based on assumptions and 'expected behavior' rather than real specifications. Each of the concepts seems to be able to deliver the required performance, but each suffers from disadvantages that are not entirely predictable on this level. Still, the first concept, using piezoelectric motors, is chosen as the most advantageous concept. The key issue in the second concept is the compactness: the problems with fitting all components within the allowed space. The key issue in the third concept is the fact that the transmission mechanism makes the design complex and limits the dynamic performance, and the problem with finding vacuum-compatible transmission mechanisms at all that comply with the requirements. Therefore, the first concept is chosen and the rest of this report will focus on a stage driven by piezoelectric motors. The focus will be on the ultrasonic motors itself, since detailed design of the stage is considered beyond the scope of

this project and the other components, such as the linear guiding and position feedback system, are not necessarily different than in any other concept or the current prototype.

Chapter 4

Piezoelectric motors

This chapter is an introduction to piezoelectric motors. The basic working principle is explained, several different types of piezoelectric motors are compared and general specifications, advantages and disadvantages are given.

4.1 Introduction and classification

4.1.1 General introduction

Piezoelectric material is a crystalline material that deforms under influence of an electrostatic field. This deformations are very small: the maximum elongation is typically less than 0.1% of the length [10]. However, it is possible to use this small displacements for generating long-stroke travel by using the piezoelectric material to generate a stepping motion [5, 10]. A well-know example of this is the inch-worm motor (see Figure 4.1). Perpetual clamping and expanding in travel direction leads to a net displacement of the clamped object. In principle, an infinite travel can be reached using this technique. Lots of other piezo-actuated step mechanisms exist.

The disadvantage of such step mechanisms is that the achievable speed is very limited. To solve this, similar actuators are developed in which the stepping motion is created by exciting a structure in a very high, usually ultrasonic, frequency using an AC voltage. In this way, the individual 'steps' are still small but due to the high frequency the resulting linear speed can be in the order of 100 mm/s. This type of motor is called 'ultrasonic motor' (USM). Lots of types of piezoelectric USM's are available or studied, but they all have one thing in common: the piezoelectric material is used to generate an ellipsoid motion at the surface of some

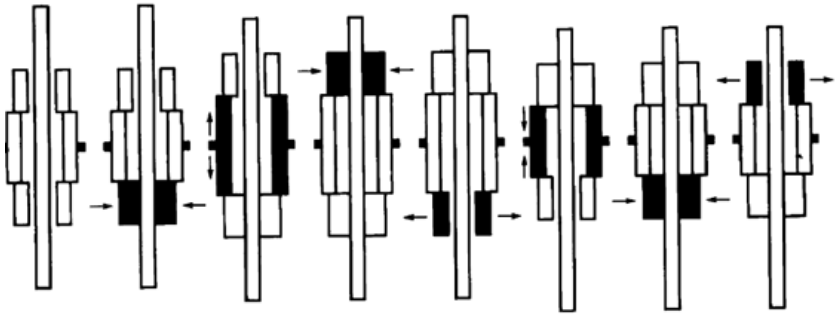

Figure 4.1: Working principle of the inchworm motor.

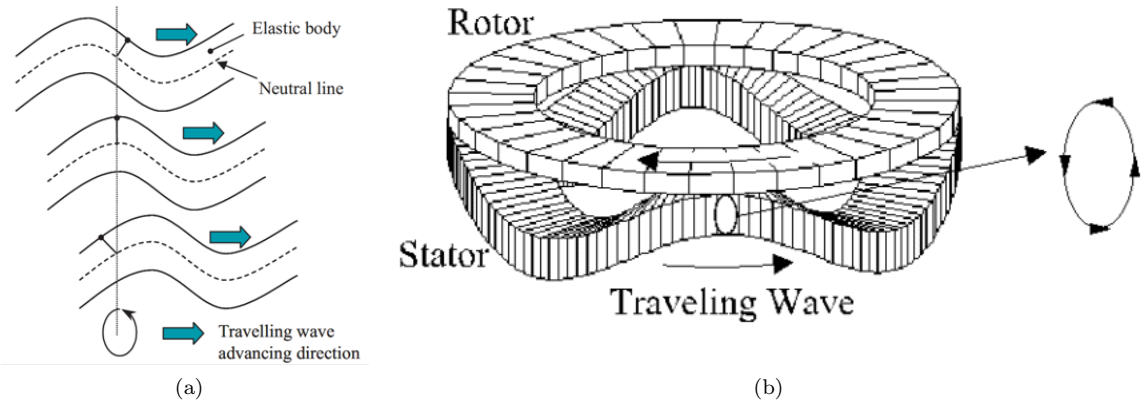

(a) (b)

Figure 4.2: Traveling wave motors: (a) working principle; (b) application in a ring-shaped medium to form a rotary motor.

structure. When this structure is pressed against a flat counter-surface, the 'drive strip', the ellipsoid motion will result in a traction force between the finger and the strip. When integrated in a positioning stage, the drive strip is mounted on the moving stage and the oscillating structure fixed to the surroundings, so that the stage is moved by the traction force in the contact.

Piezoelectric materials are divided in 'soft' and 'hard' types [11]. Soft piezo-materials have stronger piezoelectric coupling characteristics. However, hard piezo-materials have less material damping and therefore higher efficiency at high-frequency operations, so for ultrasonic motors hard piezo-material is used.

4.1.2 Drive mechanisms

The way in which the ellipsoid vibration in ultrasonic motors is generated varies strongly for different motors on the market or in research. A distinction can be made between traveling wave motors and bimodal standing wave motors.

Traveling wave mechanism In these motors, piezoelectric material is used to force a traveling wave through a flexible flat element. An individual point at the surface of the plate makes a oscillatory movement in vertical direction, but also in horizontal direction, due to the bending of the plate. These oscillations are 90 degrees out of phase, so that the resulting motion of a point at the surface is an ellipsoid. This principle is shown in Figure 4.2a. When a flat object is pushed against the resonating plate, traction forces result between the two elements due to the ellipsoid motion.

Maintaining the traveling wave is easiest in a closed-shape medium, for instance a flat circular disc (Figure 4.2b), since otherwise the vibrations need to be actively controlled at the beginning and end of the 'track'. This makes the principle useful for rotary applications: very compact and precise piezoelectric rotary motors are available on the market, of which a well-known application is automatic zoom mechanisms in photo camera's.

Research on linear traveling wave motors has lead to designs in which the ultrasonic vibrations are induced either a closed belt-shaped structure [12] or simply in a flat plate with no closed-shape geometry [13]. This research showed that due to a number of issues they are not suitable for high-speed accurate linear positioning. Typical problems are complicated mechanical design and low efficiency [13, 5]. No example is found of linear traveling wave type motors being brought to the market.

Bimodal standing wave mechanism The alternative to the traveling wave mechanism is the bimodal standing wave mechanism: ultrasonic ellipsoid motion is forced on an individual small contact element, the

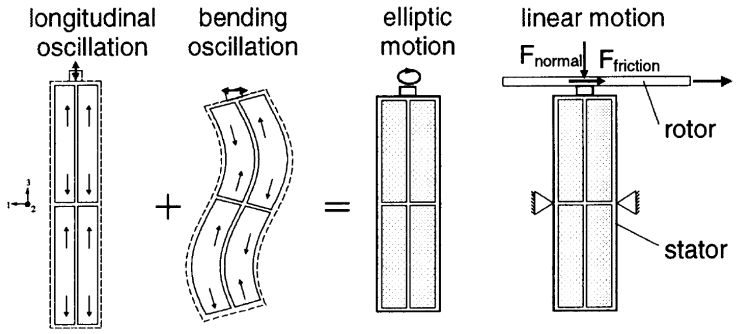

Figure 4.3: Drive mechanism of a standing wave type ultrasonic motor.

finger, by exciting two resonance modes or 'standing waves' in a piezoelectric structure. An example of such a mechanism is shown in Figure 4.3: a structure is excited in a longitudinal oscillation and a bending oscillation simultaneously, again leading to the ellipsoid motion and traction forces in the contact. By using the resonances of the structure, the amplitude of the vibrations, and with that the resulting linear velocity, is significantly bigger than in non-resonant operation. The structure is excited by an AC voltage of which the amplitude is used to control the linear velocity of the stage.

Several examples of these motors can be found on the market (for instance by Nanomotion [6] or Physik Instrumente [14]) or in research. Although the working principle is the same for each of these examples, the exact form of the structure and the mode shapes that are used to create the motion differ, leading to different characteristics.

Typical characteristics of bimodal standing wave linear USM's are velocities up to 400 mm/s, smooth and accurate positioning and passive holding force and stiffness due to the physical contact between stator and rotor. Typical issues are wear due to the frictional contact and non-linear control behavior. Some ultrasonic motors have the additional feature to do extremely precise static positioning within the range of a single step by controlling the tip deflection with a DC voltage. Another possible feature of ultrasonic motors is the integrating all movements in the horizontal plane in a single stage by letting a flat horizontal table 'float' on an array of vertically oriented ultrasonic motors instead of integrating the motor in a linear guiding. This would eliminate the need for separate x- and y-stages stacked on top of each other. However, although this type of planar piezo stages is subject of research [15, 16], they are not yet far enough developed to be applied in industrial applications.

If the traveling-wave and standing-wave principle are compared, it is easy to see that the latter induces more vibrations to the contact surface. Furthermore, in standing-wave-type motors the preload force with which the finger is pushed against the drive strip is usually such that the contact is not broken during the motion [16], which means that the contact element slides over the surface during the 'return' half of the ellipsoid motion, which causes wear at the surface. At the other hand, with the standing-wave mechanism it is possible to generate linear motion with a very simple and compact motor geometry.

4.2 Characteristics of linear ultrasonic motors

4.2.1 Manufacturer's specifications

Specifications of linear ultrasonic motors vary per specific motor, but as a reference, specifications of Nanomotion's HR8 motor are:

- Maximum velocity: 250 mm/s (up to 400 mm/s for other types).
- Force density: up to 0.36 N/cm^2 (30N stall force for a $46 \times 42 \times 24$ mm motor design).
- Resolution: < 100 nm.

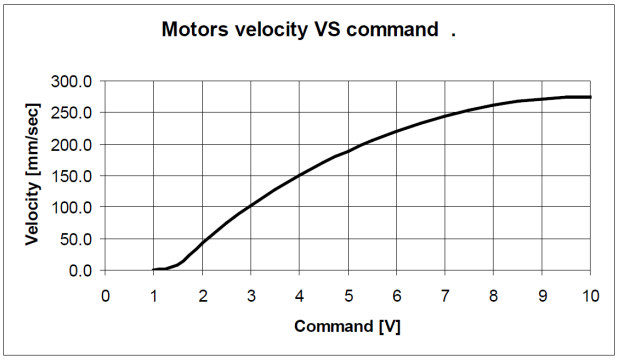

Figure 4.4: Performance characteristic of a Nanomotion HR1 ultrasonic motor

- No magnetic stray fields.

The basic behavior of ultrasonic motors is usually described by a relation between input voltage and no-load velocity, as shown in Figure 4.4. Here the 'command' is a signal sent to the driver electronics that convert it to a high-voltage ultrasonic AC voltage sent to the motor. The relation between input signal and stage velocity contains a 'dead zone' that is typical for ultrasonic motors: up to a certain input voltage, the slider will simply keep sticking to the finger. The dead zone can be eliminated if the two resonance modes are controlled independently by the driver.

4.2.2 Wear

Due to the frictional contact between the contact element of the motor and the drive strip, wear occurs. In literature, sometimes it is assumed that wear mostly occurs at the finger [17], but sometimes the wear of the finger is ignored and only that of the drive strip is observed [18]. For several reasons, wear is very unwanted:

1. Particles that are freed from the surface can contaminate the machine. More about this in the next section.
2. Lots of particles will keep sticking to the surface. This means that after a while, a layer of 'dust' is formed between the drive strip and motor that reduces the traction between these two, making the motor slip rather than grip. This can be compared to trying to walk through a 'ball pit'.

Obviously the latter affects the performance of the drive, eventually resulting in a situation where the drive isn't able to deliver the specified performance even when in strict sense nothing is wrong with the motor. In practice, malfunctioning of piezoelectric stages is almost always due to wear in the contact.

Lots of literature exists on wear mechanisms in general, but it is beyond the scope of this research to study this topic very thoroughly and try to predict the wear in ultrasonic motors. Friction and wear behavior in high-frequency sliding contact is very different from that in low-frequency or 'normal' (constant-velocity) sliding contact [19]. However, it still is assumed that for ultrasonic motors, the volume of material freed from the surface is proportional to both the running distance and the preload force, but independent of for instance the sliding velocity [20], leading to a 'specific wear rate' in units of 'volume per traveled meter per Newton preload'. The wear rate is very situation-dependent, so it is difficult to predict the wear rate of ultrasonic motors in a specific application, but typical values found in literature are in the order of $10^{-7} \sim 10^{-8}$ mm^3/Nm.

There are several ways presented in literature to reduce the wear in ultrasonic motors, for instance by exciting the motor with a rectangular block wave instead of a harmonic wave [21], or by carefully selecting the right preload force and controller settings [18, 17]. Although these methods apply only for a very specific situation, it seems that in general the controller settings and the preload force are two important parameters affecting wear in the contact.

4.2.3 Particles

Due to the wear of the ceramic strip, particles are formed. For e-beam lithography applications, there are two risk area's for particles:

1. On the wafer, where particles cause malfunction of the integrated circuit.
2. In the electron optics, where particles cause malfunction of the machine.

Nanomotion has done particle tests on its ultrasonic motors in ambient environment. Typical measured values are 5-10 particles per hour when traveling about 60 mm/minute. In [3], particle tests are done on an USM-driven XY stage in ambient environment. For 18 mm/s constant velocity a particle count rate of 0-1 particles per minute at the top of the stage but 100-300 close to the finger tips is measured.

Particles behave very differently in vacuum than in atmospheric environment. In vacuum, solid particles can keep circulating through a room for minutes or hours, 'bouncing' against the walls in random directions. After settling down, they can be freed again by vibrations in the structure they are sticking to or due to turbulent air flow when the vacuum environment is opened. The forming of particles due to wear and the behavior of particles after they are freed from a surface are extremely complex mechanisms that are highly situation-dependent. Therefore it is impossible to say if the above numbers are in any way representative for ultrasonic motors in different circumstances.

The best way to avoid particle contamination of course it trying to avoid the particles to being formed by reducing the wear as described in the previous section. However, since ultrasonic motors need the frictional contact in order to operate, it is impossible to avoid particle forming entirely. The second way to avoid particle contamination therefore is preventing the particles to travel to the risk area's.

4.2.4 Energy dissipation

In general, ultrasonic motors have problems with transporting the energy dissipated into heat to the environment. The main sources of energy dissipation are:

1. Dielectric losses in the piezo material: the capacitor formed by the electrodes with the piezo material between them is a non-ideal capacitor with a loss factor of generally about 2% for soft piezo-materials and 0.3-0.5% for hard piezo-materials [11].
2. Mechanical losses due to material damping. This is usually very low in hard piezoelectric materials, although details about material damping in piezoelectric materials are not found.
3. Friction in the contact.

Overheating is a serious issue for ultrasonic motors, especially in vacuum, due to the absence of convection. The material loses its piezoelectric behavior due to 'unpoling' when the Curie temperature is reached, usually at a few hundred degrees [11]. Therefore the allowed duty cycle is limited, dependent on the velocity and load.

Another issue is the loss of performance when the motor temperature increases: temperature-dependency of material properties such as the elasticity leads to a shift of the resonance frequency when the temperature increases. As a result, the resonance is less effectively excited by the fixed-frequency input signal, so that the motor performance is decreased [16].

Chapter 5

Simulation model

A simulation model is made of a specific ultrasonic motor to analyze its behavior in detail. This chapter contains a description of the used methods and assumptions, and several simulation results are given and discussed.

5.1 Introduction

5.1.1 Motivation

In the previous chapters it is shown that, although the ultrasonic motor is a promising solution for the required stage, it has some significant drawbacks that cause behavior of which not enough is known yet to show the feasibility of the concept. Besides, practical use of ultrasonic motors has shown that often unexpected behavior is encountered and that improving the motor performance in real life is often done by trial-and-error because real knowledge of how the motor works is very limited.

Therefore an analytical study to the behavior of the motor is wanted. The first aim of this study is to describe the behavior of the motor, including unwanted aspects as wear and heat dissipation, in more detail than possible with the current specifications and knowledge, in order to be able to show the feasibility of the concept. The second aim is to provide a tool that can be used in the stage design process to optimize design and control structures, and find solutions to possible problems, for instance problems related to overheating and particle generation.

To achieve this, a finite element model of an ultrasonic motor is built. The subject is a Nanomotion HR1 motor, since this type of motors is already used by Mapper in the Y-stage, so gaining more knowledge about this specific type of motor is the most interesting for the company. Besides, there are not many alternatives, and Nanomotion is probably the most experienced in the field.

5.1.2 Required functionality

The simulation model should at least be able to:

1. Predict the 'basic performance' of the motor, namely the relation between input signal, velocity and delivered force, within reasonable accuracy.
2. Predict the change of performance when changing important external parameters.
3. Allow evaluation of local variables such as stresses and temperature.

This can be achieved by building a finite element model that at least contains the following components:

1. A model of the structural stresses and displacements of the motor and drive strip.
2. A model of the piezoelectric effects that form the relation between the electric potential and the body displacements.

3. A model of the friction between the finger tip and drive strip.
4. A model of the energy dissipation and heat flow throughout the motor and to the environment.

It may be necessary to include the electronics providing the voltage on the electrodes, in order to describe the performance of the total system accurately.

5.1.3 Literature

Literature can be found on the modeling of ultrasonic motors, but this is almost always focused on traveling wave motors, although with proper interpretation of parameters and processes is many similarities exist with the standing wave type [22]. Often ultrasonic motors are modeled with an 'equivalent electrical circuit' built up from basic electrical element such as resistances, capacitors and diodes: in [23] ultrasonic motors are represented by an equivalent electrical circuit and in [24] a similar but more simplified way of modeling is proposed, but in both cases this is limited to rotary motors.

A model of a specific type of linear ultrasonic motor is given in [25]. This model consists of a mass-spring representation of the actuator mechanics and includes the frictional contact between finger and strip. Although the model doesn't include the piezoelectric effect that translates a voltage into a force, simulation results approximate the velocity-voltage characteristic of the motor obtained by measurements.

In [16], also a dynamic model is given. This model contains the piezoelectric and mechanical behavior of the contact material and the contact dynamics, based on a Coulomb friction model that takes into account the stick-slip contact due to the ultrasonic stepping. This model is able to predict the entire force-velocity-voltage characteristic of the observed piezo drive and corresponds quite well with experimental results.

None of the above methods, however, provides the required functionality: since all models are few-degrees-of-freedom lumped-parameter models (either mass-spring models or equivalent electrical circuits), they do not allow analysis of local variables in the body like stresses, strains, local energy dissipation and temperature. Secondly, in the above examples the model parameters are usually determined by fitting the model to experimental results, which means the model is only valid in the specific situation of the experiment. No examples are found in literature of finite element models of ultrasonic motors.

5.2 Method

5.2.1 Description of the motor

The inside of the Nanomotion motor is shown in Figure 5.1a. The most important part is the rectangular box shaped body made from piezoelectric material (1). The body is supported in four points (2) by a support structure. The support structure is placed inside the housing with rolling contacts so that it remains free to move in y-direction. The structure is pressed against the drive strip, mounted on the stage, with the preload spring (5). Four electrodes (3) are placed on the top surface and while the bottom surface contains a single electrode covering the entire surface. Fixed to the front surface is the cylindrical finger (4) with a dome-shaped tip, which is pressed against the stage surface during operation.

From now the box-shaped part is called the 'piezo-body' and the cylindrical part simply the 'finger'. In the rest of this chapter, the coordinate system will be taken such that the x-axis is in the drive direction, the y-axis is in the normal direction and the z-axis in the vertical direction, as shown in the figure. The length (y), width (x) and thickness (z) of the piezo-body are respectively 30 and 7.5 mm; more detailed dimensions can be found in Appendix C.

The electrodes are connected to the driver by only three wires: wire 0 is connected to electrode 0 (the electrode at the bottom surface), wire 1 to electrodes 1 and 4 on the top surface, and wire 2 to electrodes 2 and 3 (see Figure 5.1b for the numbering). The motor is driven in one direction by applying a 39.6 kHz AC voltage between wire 0 and wire 1, and between wire 0 and wire 2 for the other direction. This leads to the ultrasonic structural vibrations that force the stage into movement.

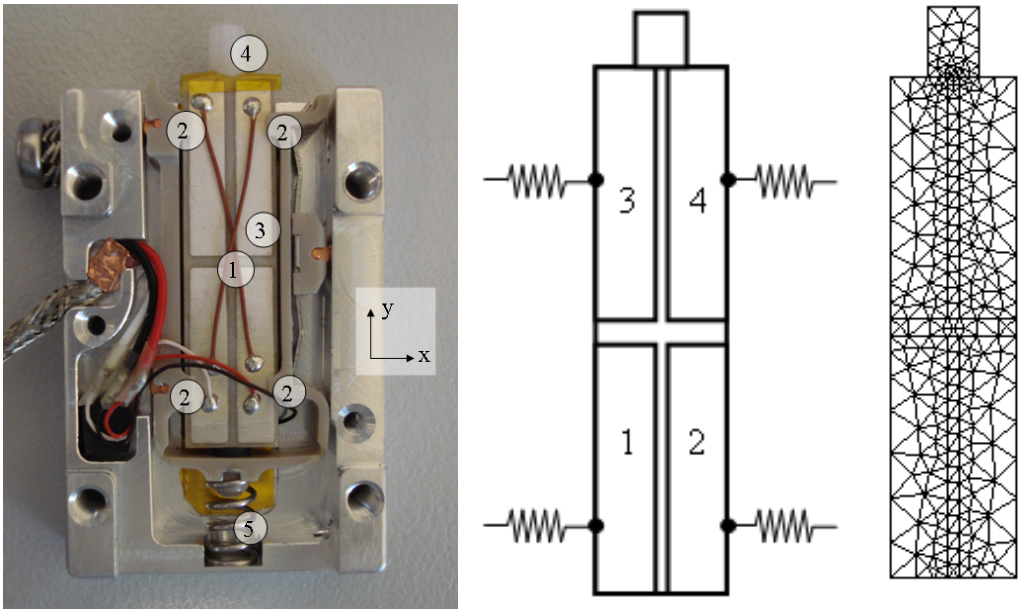

(a) (b) (c)

Figure 5.1: (a) Picture of the inside of the Nanomotion motor. The most important elements are the piezo-body (1), the four support points (2), the electrodes (3), the finger tip (4) and the preload spring (5). (b) Schematic representation of the modeled geometry. The electrodes are numbered 1 to 4; electrode 0 covers the entire bottom surface. (c) Finite element mesh.

5.2.2 Basic equations

The piezoelectric effect is described by equations that relate the mechanical stress and strain, electric field and electric displacement field inside the piezo-material. The equations are as follows [26]:

$$\mathbf{T} = [c_E]\,\mathbf{S} + [e]^T\,\mathbf{E} \tag{5.1}$$

$$\mathbf{D} = [e]\,\mathbf{S} + [\varepsilon_S]\,\mathbf{E} \tag{5.2}$$

Here $\mathbf{T}$ is the 6×1 stress vector in [N/m^2], $\mathbf{S}$ the 6×1 strain vector in [-], $\mathbf{E}$ the 3×1 electric field vector in [V/m] and $\mathbf{D}$ the 3×1 electric displacement vector in [C/m^2]. The coupling between these variables is defined by the material-specific matrices: the elasticity matrix $[c_E]$ in [N/m^2], the dielectric coefficient matrix at constant strain $[\varepsilon_S]$ in [F/m] and the piezoelectric coupling matrix $[e]$ in [C/m^2]. The first equation describes the 'forward piezoelectric coupling' (the body deformations caused by applying an electric field) and the second describes the 'backward piezoelectric coupling' (the generation of electric displacements under influence of mechanical strain)[1]. The piezoelectric material is anisotropic; the material is oriented such that the 3-direction (the polarization direction of the material) corresponds to the z-direction in the motor geometry.

The body is represented with a 2D plane stress structural model in the xy-plane instead of a full 3D model since this makes the model far less computationally expensive and displacements in the lateral direction are not of primary interest in this study (except for thermal effects) since the basic working principle of the motor is based only on the oscillations in x- and y-direction. The use of a 2D plane stress model is not completely justified since, as a rule of thumb, the thickness of the body in the third (not observed) dimension should be at least ten times smaller than the smallest characteristic dimension in the plane, which is not the case in

[1]Note that in reality, the first is called the 'inverse' effect and the second the 'direct' effect, but in this report it is done the other way around since the first plays the more important role in the ultrasonic motor.

this situation. The coupling matrix for existing piezo-materials is such that the x- and y-component of the electric field vector $\mathbf{E}$ are coupled only to out-of-plane stresses, so only E_z is taken into account.

For simplicity, it is assumed that the electric field is an input of the model. This means the backward piezoelectric coupling, represented by Equation 5.2, is neglected. Therefore the equations reduce to the following:

$$\mathbf{T}' = [c'_E]\,\mathbf{S}' + [e']^T\,E_z \tag{5.3}$$

Here $\mathbf{T}'$ and $\mathbf{S}'$ are now the 3×1 reduced stress and strain vectors containing only the in-plane terms, $[c'_E]$ the 3×3 plane stress elasticity matrix, E_z the z-direction of the electric field and $[e']$ the 3×1 reduced piezoelectric coupling matrix.

The local variable E_z is assumed to be constant over the z-axis, so that if a local variable P is defined as the potential difference between top and bottom surface, and t is the thickness of the body:

$$E_z(x, y) = \frac{P(x, y)}{t} \tag{5.4}$$

If the equations are implemented in an arbitrary finite element structure, according to general laws of finite element modeling as described in for instance [27], the following equations of motion result:

$$[M]\,\ddot{\mathbf{d}} + [Z]\,\dot{\mathbf{d}} + [K]\,\mathbf{d} = [S]\,\mathbf{P} + \mathbf{f} \tag{5.5}$$

With n the number of nodes, $\mathbf{d}$ is the $2n \times 1$ vector of nodal x- and y-displacements in [m], $\mathbf{P}$ the $n \times 1$ vector of nodal potential differences in [V], $\mathbf{f}$ the $2n \times 1$ vector of applied nodal forces in [N], $[M]$, $[Z]$ and $[K]$ respectively the $2n \times 2n$ mass, damping and stiffness matrix in [kg], [Ns/m] and [N/m], and $[S]$ the $2n \times n$ piezoelectric coupling matrix in [N/V], translating the potential distribution to 'applied forces'.

A detailed description on how the matrices $[M]$, $[Z]$, $[K]$ and $[S]$ are obtained from the basic equations of piezoelectricity is found in Appendix D.

5.2.3 Free body model

The basic equations are applied to a geometric model of the piezo-body supported in the four support points and constrained in y-direction in the contact node, but without including the slider and frictional contact, so the tip is free to move in x-direction. This will be called the 'free body' from now.

Geometric domain The finite element model consists of only the piezoelectric body including the cylindrical finger tip, as in Figure 5.1b. The support structure is not included in the domain. Detailed dimensions are given in Appendix C.

Mesh The mesh consists of 469 triangular linear elements and 262 nodes, as shown in Figure 5.1c.

Material properties Of the piezo-body material nothing is known except that it is a hard piezo-material, so properties of the material 'pic241' from the documentation of PI Ceramic [11] are used. The finger tip and drive strip are made of Al_2O_3 ceramics [17]. The approximated value for the friction coefficient μ between the finger and drive strip is 0.36. Material damping is modeled in the form of Rayleigh damping, as proposed in [28], which gives the following relation for the damping matrix:

$$[Z] = \alpha\,[M] + \beta\,[K] \tag{5.6}$$

Detailed material properties are given in Appendix C.

Support points The four support points are modeled by adding a virtual spring in y-direction to four nodes at the locations of the real support points. The stiffness of these support springs is set to 10^6 N/m, which is sufficient to prevent the body from drifting too much while it is low enough to have no significant influence the second bending mode in the body, as it is expected to be in reality.

Preload spring The preload spring is modeled as an applied force f_{pl}. Since the displacements in the body are in micrometer range while the stiffness of the preload spring is in the order of 1-10 N/mm, the applied force is assumed to be constant. Based on experiments, a value of 16.2 N is used. The force is distributed over the four support points, since in reality the spring acts on the support structure.

Contact node In reality the contact is known to take place on an area with a small diameter (400 µm) compared to the tip diameter (3 mm), so in the current mesh only the node on the middle of the tip is in contact with the drive strip. Therefore the contact conditions in the model are applied only to this node. In a Coulomb friction model, friction forces are independent of the contact area, so a point contact should still lead to realistic forces. Besides, the equations describing the contact friction become significantly more complex if multiple nodes are used.

To model the contact, this node is constrained to zero displacement in y-direction, so the assumption is made that the finger doesn't come loose from the counter-surface and the surface is infinitely stiff. For now the x-displacement of the tip is free.

Applied voltage The model has two independent voltage inputs V_A and V_B. V_A corresponds to the voltage between wire 0 and wire 1 (electrode 0 and electrodes 1+4), and V_B corresponds to the voltage between wire 0 and wire 2 (electrode 0 and electrode 2+3). In the finite element model this means the local variable P is constrained to V_A at the nodes lying on subdomain 1 and 4 and to V_B at the other two subdomains. To drive the motor, the 39.6 kHz AC signal is applied to either V_A or V_B while the other is zero.

Reduced equations of motion The degrees of freedom of the model are the x- and y-displacement of each of the nodes, except for the y-displacement of the contact node, which is constrained. This brings the number of degrees of freedom n to $2 \cdot 262 - 1 = 523$. There are three independent model inputs, namely the preload force f_{pl} and the applied voltages V_A and V_B for each of the driving directions. Therefore, the general equations of motion in 5.5 are rewritten to the following form:

$$[M_f]\,\ddot{\mathbf{d}}_f + [Z_f]\,\dot{\mathbf{d}}_f + [K_f]\,\mathbf{d}_f = [X_f]\,\mathbf{u}_f \tag{5.7}$$

Now $\mathbf{d}_f$ is the $(2n-1) \times 1$ vector of unconstrained nodal displacements and $[M_f]$, $[Z_f]$ and $[K_f]$ the $(2n-1) \times (2n-1)$ structural matrices of the free body. Furthermore, $\mathbf{u}_f$ is the 3×1 vector of independent inputs:

$$\mathbf{u}_f = \begin{bmatrix} f_{pl} & V_A & V_B \end{bmatrix}^T$$

The input coupling matrix $[X_f]$ is a $2n \times 3$ matrix of which the first column represents the distribution of the preload force f_{pl} over the four support nodes and the second and third column the translation from respectively V_A and V_B to 'applied forces' via piezoelectric coupling matrix $[S]$.

The mathematical derivation of the reduced equations of motion is given in Appendix D

5.2.4 Full model

The slider is added to the model of the piezo-body and friction is added in the contact between the finger and the slider, resulting in the 'full model'.

Slider model and contact forces The slider is represented by a rigid body with mass m_{sl} and displacement d_{sl} in x-direction. The mass of the slider in the model is 10 grams; this is very small for a real slider, but this speeds up the simulations. Friction in the guiding of this slider is represented by a constant force f_{sf} opposite to the direction of motion. Between the contact node of the finger and the slider, contact forces f_D and f_N are defined: f_D is the tractional force in x-direction, positive if the force on the slider is in positive x-direction (and thus a reaction force on the tip in negative x-direction) and f_N the normal contact force, such that a compressing force is positive. The equation of motion for the slider is:

$$m_{sl}\ddot{d}_{sl} = f_D + f_{sf} \tag{5.8}$$

Equations of motion For the coupling between the x-displacement of the finger tip node and the slider two 'phases' are possible: stick or slip.

In case of stick, the velocity (or acceleration) of the finger tip equals that of the slider. This is added as a condition to the equations of motion:

$$\ddot{d}_{sl} = \ddot{d}_{tip} \tag{5.9}$$

This, together with Equations 5.7 and 5.8 leads to a new set of linear equations [2]:

$$\begin{bmatrix} [M_f] & m_{sl}\mathbf{n}_{tip} \\ \mathbf{n}_{tip}^T & -1 \end{bmatrix} \begin{bmatrix} \ddot{\mathbf{d}}_f \\ \ddot{d}_{sl} \end{bmatrix} + \begin{bmatrix} [Z_f] & [0] \\ [0] & 0 \end{bmatrix} \begin{bmatrix} \dot{\mathbf{d}}_f \\ \dot{d}_{sl} \end{bmatrix} + \begin{bmatrix} [K_f] & [0] \\ [0] & 0 \end{bmatrix} \begin{bmatrix} \mathbf{d}_f \\ d_{sl} \end{bmatrix} = \begin{bmatrix} [X_f] & \mathbf{n}_{tip} \\ [0] & 0 \end{bmatrix} \begin{bmatrix} \mathbf{u}_f \\ f_{sf} \end{bmatrix} \tag{5.10}$$

Here $\mathbf{n}_{tip}$ is a $(2n-1)\times 1$ vector containing a 1 at the index corresponding to d_{tip} in $\mathbf{d}_f$, and zeros elsewhere. The equations can be written as:

$$\left[M^{stick}\right]\ddot{\mathbf{d}}_{full} + \left[Z^{stick}\right]\dot{\mathbf{d}}_{full} + \left[K^{stick}\right]\mathbf{d}_{full} = \left[X^{stick}\right]\mathbf{u}_{full} \tag{5.11}$$

Now $\mathbf{d}_{full}$ is the $2n\times 1$ vector containing the unconstrained nodal displacements $\mathbf{d}_f$ and the slider displacement d_{sl}, and $\mathbf{u}_{full}$ the 4×1 vector containing the same independent inputs as before, plus the slider friction.

In case of slip, the tip and slider displacement are uncoupled and a traction force acts between the finger and the strip. This is done using the Coulomb friction model, which means the normal force f_N and f_D are explicitly coupled by the constant friction coefficient μ:

$$f_D = \mu f_N \tag{5.12}$$

This is again an additional condition that leads to set of equations of motion for the slip state, with the same form as Equations 5.11. The equations are dependent on the slipping direction, so in the end three sets of equations of motion remain:

$$\begin{cases} \left[M^{stick}\right]\ddot{\mathbf{d}}_{full} + \left[Z^{stick}\right]\dot{\mathbf{d}}_{full} + \left[K^{stick}\right]\mathbf{d}_{full} = \left[X^{stick}\right]\mathbf{u}_{full} & \text{stick phase} \\ \left[M^{slip+}\right]\ddot{\mathbf{d}}_{full} + \left[Z^{slip+}\right]\dot{\mathbf{d}}_{full} + \left[K^{slip+}\right]\mathbf{d}_{full} = \left[X^{slip+}\right]\mathbf{u}_{full} & \text{positive slip phase} \\ \left[M^{slip-}\right]\ddot{\mathbf{d}}_{full} + \left[Z^{slip-}\right]\dot{\mathbf{d}}_{full} + \left[K^{slip-}\right]\mathbf{d}_{full} = \left[X^{slip-}\right]\mathbf{u}_{full} & \text{negative slip phase} \end{cases} \tag{5.13}$$

Time integration Time integration is done on the above equations of motion according to the following procedure:

1. Perform numerical integration on the system of equations for one phase until 'transition' to the other phase is detected.
2. Find the exact transition moment and stop the integration.
3. Begin a new integration run with the equations for the next phase, using the end solution of the previous run as initial solution.

Since the displacements and velocities in the model are all maintained at the transition moments, there is no virtual energy added to or subtracted from the system with this method.

Transition from stick to slip phase is triggered if the traction force in the contact exceeds its maximum:

$$|f_D| > \mu f_N \tag{5.14}$$

Transition from slip to stick state is triggered if the relative velocity between the finger and the slider approaches zero:

$$\dot{d}_{sl} - \dot{d}_{tip} = 0 \tag{5.15}$$

[2] Note that it is possible to write this system without the slider displacement as a separate degree of freedom since it sticks to the tip, but this would lead to a difference in the vector of degrees of freedom between the stick and slip phase, making switching between the phases in time integration less straightforward.

Since no existing finite element package is found that is able to do dynamic (time-dependent) analysis on a model that includes a non-continuous Coulomb friction force between two bodies, the model is built in MatLab, version 2010b. The finite element package COMSOL is used to draw the body and create the mesh. In MatLab, this mesh is imported, the equations of motion are derived and the model is solved by numerical integration. The MatLab-function 'ode45' is used to perform the numerical integration and detect the transition moments.

In order to increase the simulation speed, an attempt is done to reduce the number of degrees of freedom. This is done using the method of modal superposition as described in for instance [27]. However, since the model contains three separate systems of linear equations, each with its own set of resonance modes, a small discontinuity is inevitably introduced at the transition points when not all modes are used. This leads to results that are unstable or too far off from the full model. Therefore in the end only the full model is used; reducing the model is left as a recommendation for future work.

5.2.5 Thermal model

In order to describe the heating of the motor due to energy dissipation in the piezo-body and the frictional contact, a separate 3D model should be built, since heat flow and temperature gradients in z-direction cannot be described in a 2D model. This model should be able to simulate conductive heat transport (via the support points and the finger tip), convection and radiation, because all of them play a role in the cooling of the motor element. From the results of the dynamic model, an estimation can be made of the amount of energy dissipated, and the distribution of energy dissipation over the xy-plane, as an input for the thermal model.

An attempt is done to build such a model in COMSOL, but due to the complexity of the problem and the insufficient knowledge of the thermal material properties, no useful results are acquired. This is left as a recommendation for future work.

5.3 Results

5.3.1 Free body behavior

The basic behavior of the piezo-body is shown by doing static, eigenvalue and frequency response analysis. This is done on the free body, the model of the piezo-body without slider, supported in the four support points and constrained in y-direction in the contact node.

Basic behavior If a static voltage $V_A = 250$ V is applied to the system, the deflection of the free body is as depicted in Figure 5.2a. An eigenvalue analysis shows a first bending vibration mode at 22.2 kHz, a second bending mode at 49.6 kHz and a longitudinal mode at 68.1 kHz. The second bending mode is shown in Figure 5.2b. In Figure 5.2c and 5.2d a frequency response is shown of the transfer from V_A to the tip displacement in x-direction and the normal contact force. All three of the aforementioned resonance modes are visible in the frequency response plots.

If a point mass of 10 g is added to the finger tip, to represent the behavior of the model when a slider is fixed to the finger, the second bending resonance is visible at about 61 kHz, and the mode shape is different: the displacement of the finger tip is very small because of the large mass applied to it.

Influence of several parameters and assumptions In Table 5.1a the second bending resonance frequency and static tip displacement at $V_A = 250$ V are given for different meshes in 2D and 3D. The 2D analyses are done as before in MatLab, the 3D analyses are done in COMSOL, using a geometry, constraints and boundary conditions equivalent to the 2D model.

In the 3D model, there is 2-way piezoelectric coupling, while in the 2D model the backward coupling is neglected as described before. Therefore, for the eigenvalue analysis in the 3D model in Table 5.1a the top and bottom surface are grounded: constraining the potential is approximately equivalent to neglecting the

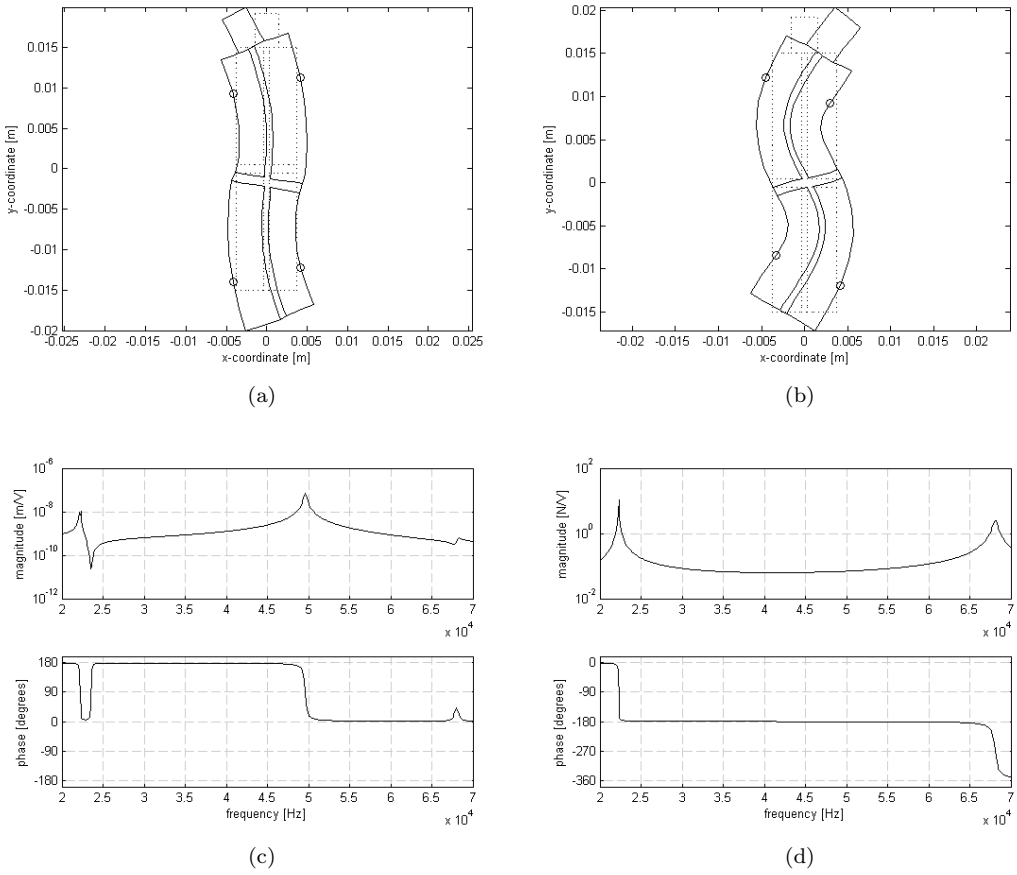

Figure 5.2: Various simulation results for free body: (a) static deflection with $V_A = 250$ V; (b) second bending resonance mode; (c) frequency response of the transfer from input voltage V_A tip displacement d_{tip}; (d) frequency response of the transfer from input voltage V_A to normal contact force f_N.

backward piezoelectric coupling. In Table 5.1b the 3D model with grounded surfaces is compared to the situation in which the electric potential on the surface is unconstrained.

Table 5.1c shows the influence of the stiffness of the support springs on the second bending resonance frequency, using a mesh with 1531 elements.

5.3.2 Full simulations

Time-dependent simulations are done on the full model. This is done by performing numerical integration, starting at a static equilibrium position, and continuing until the slider velocity reaches a more or less steady-state value. The model inputs are: $f_{ps} = 16.2$ N, $V_A = \bar{V}_A \sin(2\pi F_d t)$ V, $V_B = 0$ and $f_{frict} = 0$, with $\bar{V}_A$ and F_d respectively the amplitude and frequency of the AC input voltage V_A, which are different for the various simulations.

Frequency response Since the drive frequency that will bring the simulation model in its useful resonance is not necessarily the same as the frequency used in reality or the frequency of the second bending mode of the free body, the optimum drive frequency F_d is determined by performing a set of simulations for different drive frequencies and $\bar{V}_A = 150$V. In Figure 5.3a, the slider velocity is plotted against the input frequency.

Mesh	2nd bending frequency (kHz)	static tip displacement (µm)
2D - 469 linear elements (MatLab)	49.6	0.189
2D - 1531 linear elements (MatLab)	48.2	0.194
2D - 2664 linear elements (MatLab)	48.1	0.196
3D - 2483 quadratic elements (COMSOL)	48.0	0.184
3D - 9640 quadratic elements (COMSOL)	48.0	0.182

(a)

Boundary condition type	2nd bending frequency (kHz)
Constrained (default)	48.0
Free	49.4

(b)

Support stiffness (N/m)	2nd bending frequency (kHz)
0	48.2
1e6 (default)	48.2
1e8	50.8
∞ (fixed constraints)	58.2

(c)

Table 5.1: Influence of several assumptions and parameters on basic behavior: (a) free body behavior for several 2D and 3D meshes in MatLab and COMSOL; (b) influence of electric boundary conditions on 2nd bending resonance frequency in the 3D 2483-element mesh in COMSOL; (c) influence of the support stiffness on the 2nd bending resonance frequency in the 2D 1531-element mesh in MatLab.

The optimum frequency is 51.5 kHz, close to the frequency of the second bending mode in the free body, but not exactly the same.

In order to bring the optimum frequency to 39.6 kHz as used in reality, a correction factor of $(51.5/39.6)^2$ is applied to the density of the materials. The new results are shown in Figure 5.3b.

Single simulation In Figure 5.4 some detailed results are shown of a single simulation run on the corrected model using $\bar{V}_A = 150$ V, $F_d = 39.6$ kHz. Figures 5.4a and 5.4b show respectively the tip displacement and slider velocity against time. Figure 5.4c shows the traction force f_D (continuous line) and the normal force f_N multiplied by $\pm\mu$ (dotted line) for a few oscillation periods. The area's where $f_D = \pm\mu f_N$ represent slip, while the area's where $-\mu f_N < f_D < \mu f_N$ represent stick (see Equation 5.12). Figure 5.4d shows the deformed shape at the end of the simulation. The colors represent the Von Mises stress in the body.

Voltage-velocity and voltage-force characteristic Simulations are done with $F_D = 39.6$ kHz to show the relation between the input amplitude $\bar{V}_A$ and the slider velocity $\dot{d}_{sl}$. The results are shown in Figure 5.5a. Furthermore, simulations are done to find the stall force of the motor against a stationary stage. In this simulations the slider displacement is constrained to zero, and simulation is done from static equilibrium to the moment that the vibrations reach a more or less steady-state value. Figure 5.5b shows the average stationary stall force against the input voltage amplitude.

Parameter sensitivity Simulations are done to show the influence of the model parameters μ (the friction coefficient in the contact) and β (the Rayleigh material damping coefficient) on the results. The reference situation is $\mu = 0.36$, $\beta = 2 \cdot 10^{-8}$ s. In Figure 5.6a the steady-state velocity is shown for several values of β, each with the same input amplitude. To observe the influence of the friction coefficient in more detail, a new set of simulations is done with friction coefficient $\mu = 0.2$. The optimum frequency is found to be 50.4 kHz, and again a correction factor is given to the mass to bring this frequency to 39.6 kHz. Figure 5.6b shows the voltage-velocity plot of this simulations after correction.

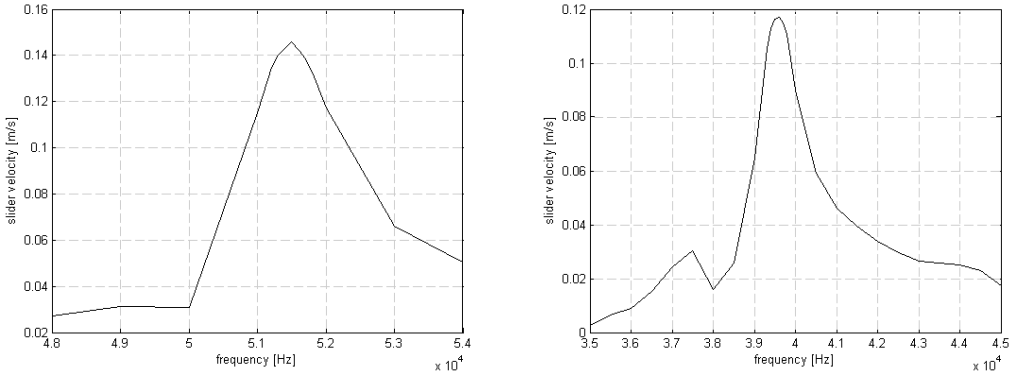

(a) (b)

Figure 5.3: Slider velocity $\dot{d}_{sl}$ against input frequency F_d for (a) uncorrected and (b) corrected model.

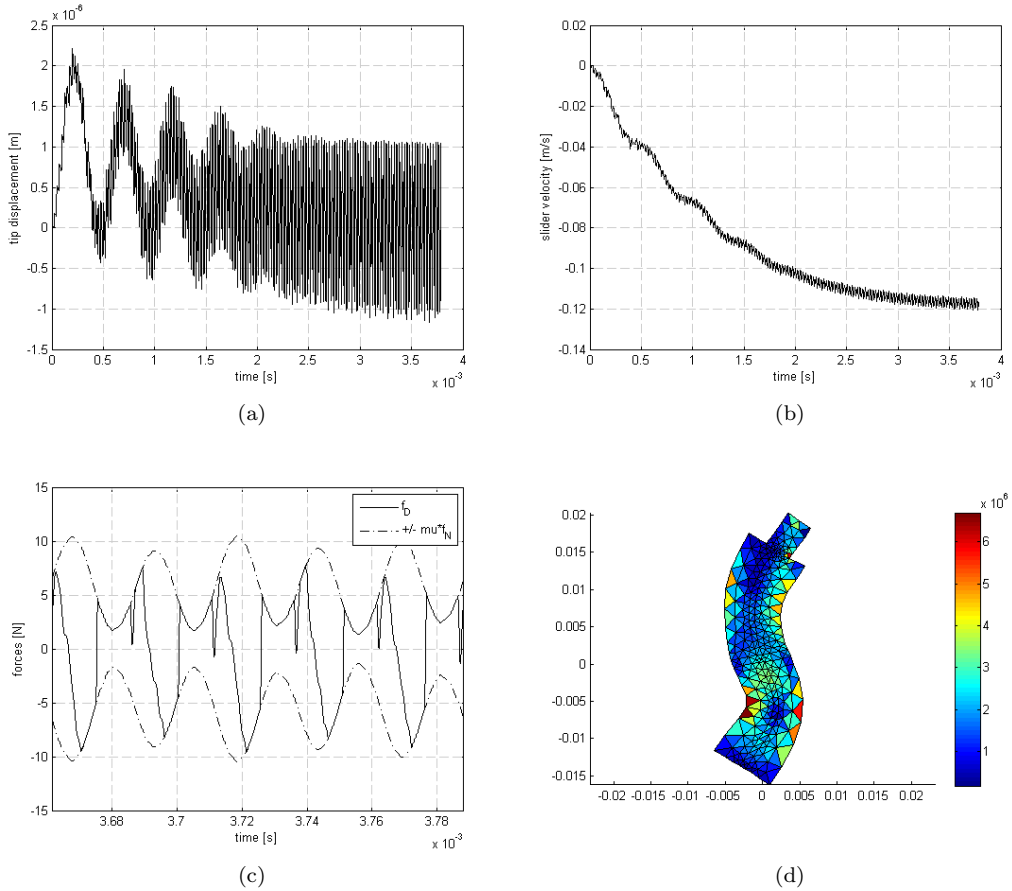

(a) (b)

(c) (d)

Figure 5.4: Detailed results of a single simulation with $\bar{V}_A = 150$ V, $F_d = 39.6$ kHz: (a) tip displacement d_{tip} against time; (b) slider velocity $\dot{d}_{sl}$ against time; (c) traction force f_D and $\pm\mu$ times normal force f_N in the contact node against time for a few oscillation periods; (d) deformed body at the end of the simulation with colors representing the Von Mises stress in the individual elements.

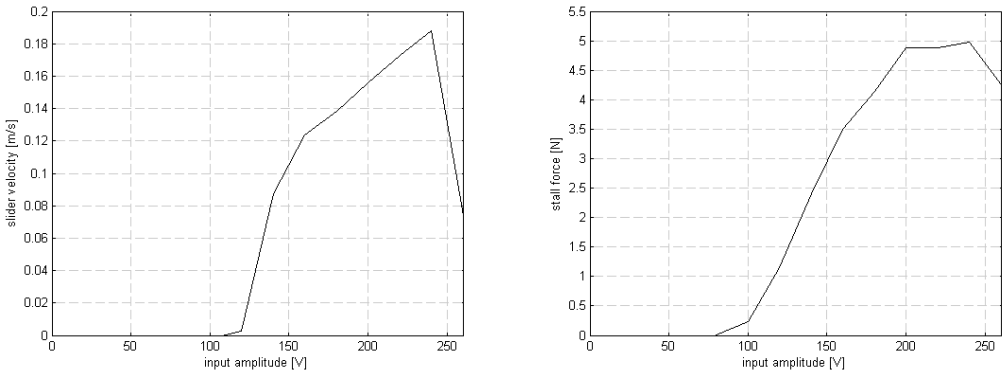

(a) (b)

Figure 5.5: Steady-state characteristics: (a) slider velocity $\dot{d}_{sl}$ against input amplitude $\bar{V}_A$; (b) static stall force against input amplitude $\bar{V}_A$.

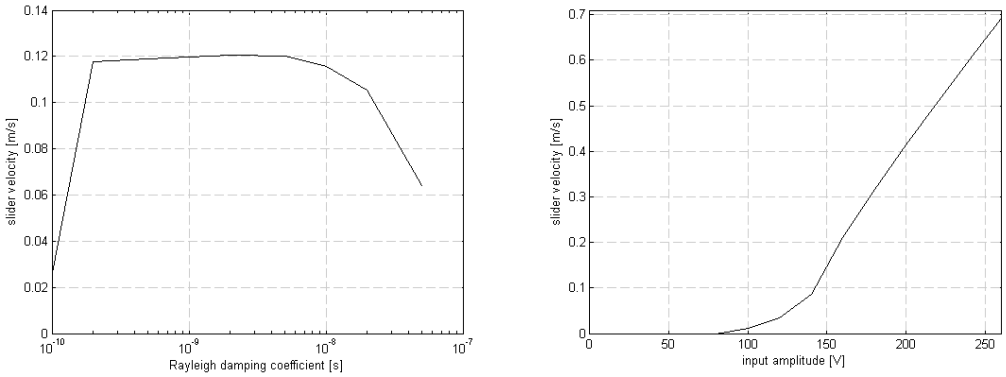

(a) (b)

Figure 5.6: Influence of several parameters (a) slider velocity $\dot{d}_{sl}$ against Rayleigh damping value β; (b) slider velocity $\dot{d}_{sl}$ against input amplitude $\bar{V}_A$ for friction coefficient $\mu = 0.2$ instead of 0.36.

5.4 Discussion

5.4.1 Interpretation of results

Resonance The working of the motor strongly depends on a mechanical resonance of the body. In reality, the motor is able to reach a velocity of 250 mm/s at a driving signal of about 250 V, 39.6 kHz. Assuming a harmonic tip oscillation, and knowing that the amplitude of the tip velocity should at least be equal to the slider amplitude, it follows that the tip vibration in x-direction should theoretically be at least $0.25/(39600 \cdot 2\pi)$ ≈ 1 µm. The static displacement of the tip in x-direction in Figure 5.2a is 0.19 µm for 250 V DC input, and from the frequency response in Figure 5.2c it is seen that the amplitude of this displacement for 250V AC input in kHz range is also about 0.1 µm in the non-resonant area's. This is far less than the necessary value, so clearly the motor strongly depends on a resonance.

In the frequency response plots for the free body in Figure 5.2c and 5.2d it is seen that this necessary resonance is found around 50 kHz. At that point, the following is observed:

1. The second bending resonance of the body is strongly excited by the input voltage, so the amplitude of the tip displacement is in the order of 10 µm, roughly 2 orders of magnitude higher than the non-resonant value.
2. The amplitude of the normal force is not influenced by the resonance. Ideally, the amplitude of the normal force is such that it just doesn't break loose from the counter surface. Here the amplitude of the normal force is about 17 N for 250 V input so with 16.2 N preload force this is close to the optimum.
3. The phase difference between the normal force and the tangential displacement is exactly 90 degrees. This means the normal force is 'high' if the tip moves in one direction and 'low' if it moves in the opposite direction, so that more energy is delivered in the first than in the second direction. This is exactly the principle on which the working of the motor is based.

With the full model, the optimum frequency and mode shape are influenced by the presence of the frictional contact and dependent on the friction coefficient, but from Figure 5.4d it is seen that the body deformation during the simulation strongly resembles the second bending mode of the free body so it is clear that this mode is excited. For the observed cases, $\mu = 0.2$ and $\mu = 0.36$, the optimum frequency is respectively 50.4 and 51.5 kHz. This increase can be explained by the fact that the higher the friction coefficient, the more the finger will stick to the stage, so the resonance frequency increases towards the value of 61 kHz that is found for the model where the slider is completely fixed to the finger.

Displacements of finger and slider In Figure 5.4a it is seen that the tip oscillates in x-direction not only at the frequency of the input signal, but also an oscillation at about 2 kHz is seen. This is likely due to a rigid-body vibration of piezo-body in its compliant support points: eigenvalue analysis of the free body shows two rigid-body modes around 3.5 kHz while a rigid-body mode is seen at 1.4 kHz if the slider mass is added to the tip. Due to the stick-slip behavior it is understandable that a rigid-body mode exists somewhere between this values. The 2 kHz oscillation dies out in a few milliseconds, so it doesn't influence steady-state behavior of the model.

The amplitude of the high-frequency oscillation in the x-displacement of the tip d_{tip} 'slowly' increases, as is expected in resonance-based oscillations. At a close-up the tip displacement resembles a sawtooth-like function, which indicates that the finger sticks to the stage to one side and then rapidly slips to the other side. The slider velocity (Figure 5.4b) 'slowly' increases to an end value of about 150 mm/s, in this case in negative direction. The ripple on the velocity is due to the finger oscillation; due to the small slider mass, this ripple is exaggerated.

Stick-slip behavior Stick-slip behavior is obviously a key aspect in the simulation model. Both the stick- and slip phase are present in the simulation results. The ratio in which they are present depends on the applied input: for high voltage, the finger slips in both directions and only sticks for a short time in between. With somewhat lower voltage, the finger slips only to one side and sticks to the stage in the other direction.

If the voltage becomes too low, the finger isn't able anymore to 'escape' the stick state, which means the slider won't move with respect to the finger. This last phenomenon causes the well-known dead zone in the voltage-velocity characteristic of the motor, clearly visible in Figure 5.5a and 5.6b.

Inherent to the working principle of the motor is that the effective force exerted by the motor to the stage decreases when the slider velocity increases, until at a certain velocity, the effective force is zero. Therefore, the stage always reaches a steady-state velocity instead of keeping accelerating, even when there is no friction in the guiding.

The friction coefficient is an important parameter in the model. It determines the ratio between sticking and slipping: as expected, when the friction coefficient is lower, the finger doesn't stick as much as with a higher friction coefficient. This means with a lower friction coefficient, the finger can move more freely, so the amplitude of the oscillation of the finger tip in x-direction is higher, leading to a higher slider velocity as seen in the figures.

Breaking of the contact In the simulation results the normal forces in the contact between the finger and drive strip become negative when the input voltage exceeds a certain value. In reality, the contact would be broken but this is not possible in the simulation model. This leads in some cases to unstable behavior, as seen in Figure 5.5a, where the velocity collapses after a certain point. Since negative contact forces have no physical meaning, the results are not valid anymore beyond this point.

Influence of material damping The results in Figure 5.6a, show that the slider velocity is slightly increased when β is decreased, but the change is only about 10%. Increasing the damping leads to lower velocity, which is obvious since more energy is dissipated and therefore less energy is effectively put into the stage. It should be noted that the results for $\beta = 10^{-10}$ are not valid since the normal contact force is sometimes negative in this solution.

Mechanical efficiency and energy dissipation From the results it is possible to evaluate energy dissipation in the system due to dielectric loss, material damping and friction in the contact. In the simulations without slider friction, the losses are: 7.5 mW (1.7%) dielectric loss, 92 mW (20.4%) due to material damping and 354 mW (78.0%) due to friction in the contact, at steady state velocity and 150 V input amplitude.

In the contact area, part of the power delivered by the motor is effectively transferred to the stage for accelerating the stage and overcoming the guiding friction, while part of the power is dissipated by the contact friction. The ratio between the effective power and the total is called the contact efficiency. Obviously, in the simulations without slider friction this efficiency is zero at steady-state velocity because no energy is added to the stage. In simulation results with 1.1 N slider friction, the efficiency is between 10 and 30 %, depending on the velocity: the efficiency decreases for increasing velocity.

5.4.2 Resonance frequency error

One of the most important observations is the difference in the optimum drive frequency in the simulations and the known drive frequency in reality. An overview of the most important frequencies:

- Drive frequency in reality: 39.6 kHz.
- Resonance frequency of the free body: 49.6 kHz.
- Optimum frequency in full model with $\mu = 0.2$: 50.4 kHz.
- Optimum frequency in full model with $\mu = 0.36$: 51.5 kHz.

There are two known sources of error in the resonance frequency in the body: the plane stress assumption and the coarseness of the mesh. The difference in the second bending frequency of the free body between the finest 2D mesh and the 3D mesh in Table 5.1a is only 0.1 kHz, about 0.2%, so the plane stress assumption causes only a very small error. The mesh size is a more significant factor: from Table 5.1a it is seen that with the default mesh the resonance frequency is about 1.5 kHz higher than the 'reference', a very fine mesh,

so this effect results in an overestimation of about 3.1% of the resonance. This is due to the well-known phenomenon in finite element modeling that structural stiffness is overestimated if the mesh is too course.

The above two error sources are not big enough to fully explain the difference between the real drive frequency and the resonance in the model. Two possible additional explanations can be found:

1. In reality the drive frequency is *not* the frequency at which the second bending resonance is excited.
2. The model gives an inaccurate prediction of the system behavior due to certain simplifications or errors in the parameters.

The first is highly unlikely, firstly because literature suggest that the Nanomotion motor uses this resonance [5, 17], and secondly because the simulation results clearly show that the motor is not able to even get close to the specified performance when not in this resonance. Therefore it should be because of inaccuracy of the model.

It is expected that the main reason for the difference in frequency between the simulation model and reality is the simplified way in which the support structure is modeled. Since the support points are not entirely in the nodes of the vibration shape (see Figure 5.2b), it is imaginable that the dynamics of the support structure influence the dynamics of the piezo-body. Although in general the stiffness of the support springs causes an increase in the resonance frequency, as seen in Table 5.1c, it is possible that effective resonances exist below the 49.6 kHz of the free body for different ways of modeling the support structure. Proof of this is given in Appendix E, where it is shown that, for certain support conditions, the transfer from input voltage to tip vibration is effectively influenced by resonance around 40 kHz. To investigate if this is indeed the cause for for the difference between simulation model and reality, the geometry of the real support system should be included in the finite element model.

Apart from this, several assumptions and inaccuracies may cause an error in the frequency, as listed below.

Geometric properties Inaccuracy of the dimensions of the model have some influence (for instance, with l and w the length and width of the piezo body, the second bending resonance frequency is approximately proportional to $l^{1.5}$ and $w^{0.5}$), but since all geometric dimensions are determined with about 0.1 mm accuracy, this leads to an uncertainty of not more than a few hundred Hz in the resonance frequency.

Material properties The resonance frequency scales with the square root of both the mass and stiffness of the material, but although the properties of the material used in the real motor are unknown, properties of hard piezoelectric crystals found in literature differ only slightly, not enough to explain an error in the resonance frequency of more than 2 kHz.

Material not taken into account There are a few additional elements in the real system connected to the piezo-body that vibrate along: the electrodes, the solder joints that connect the wires to the electrodes and part of the wires itself. This provides some extra inertia, but the estimated mass of these elements is very small compared to the mass of the piezo-body itself, so this doesn't lead to a significant error.

Electrodynamics Just as the support structure dynamics, the dynamics of the electronic system (the driver) providing the voltage on the electrodes could influence the resonance. In the model, the potential on the electrodes is purely a prescribed input variable, which corresponds with zero output impedance of the driver. In Table 5.1b it is shown that when the potential on the electrodes is free (corresponding to infinite driver output impedance), the resonance frequency is increased with 1.4 kHz (about 2.9%). It is however imaginable that when the driver output impedance is a complex combination of inductance, resistance and capacitance (the electrical equivalent for mass, damping and stiffness) a reduction of resonance frequency is possible. This hypothesis is not yet investigated. To implement this in the current 2D model the backward piezoelectric coupling should be taken into account.

Chapter 6

Measurements

The results of the simulation model need to be validated. Validation by comparing simulation results with manufacturer's specifications is possible, but the specifications are very limited so that not every aspect of the model can be validated in this way. Therefore validation via experiments is necessary. In this chapter a description is given of the experimental setup that is used for the purpose and the measurements done on this setup. The results are presented and compared to the results of the simulations.

6.1 Experimental setup description

To carry out the measurements, a test setup is built. Most of the intended functionality of the test setup is to send different kinds of signals to an USM-driven stage and measure the precise reaction of the stage, namely the displacement in time. Therefore the setup should at least contain a linear stage, an ultrasonic motor, a precise and long-stroke position measurement system and means to control the motor and readout the position sensor.

6.1.1 General description

A picture of the setup is shown in Figure 6.1. The setup consists of a slider (1) guided along a linear rail (2). The slider consists of two carriages (not visible in the picture) connected by an aluminum component. The slider is driven by an ultrasonic motor (3) that acts against a ceramic drive strip (4) mounted against the side surface of the slider. At the other side is a linear position encoder consisting of an encoder head (5) and a glass scale (6). The motor, rail and encoder head are mounted on an aluminum base plate. Two relay switches are connected to the stage to detect when the slider reaches its extreme positions.

The total moving mass of the slider is approximately 300 g.

6.1.2 Detailed component specifications

Motor A Nanomotion HR1 motor, containing a single piezo-element, is selected for the test setup. Motor designs with multiple parallel elements are available but using this would make comparison between simulation and experimental results less straightforward and would increase the requirements for the rest of the setup in terms of loads. A vacuum version of this motor is used: for the current purpose it makes no real difference, but in the future it could be interesting to do tests in a vacuum environment since in the end the real stage needs to operate in vacuum too. The drive strip is the standard Nanomotion ceramic drive strip with a length of 150 mm. The motor is mounted on the frame according to Nanomotion standard procedure: the motor is pushed against the strip with a spacer in between that ensures 1.8 mm distance between the strip and the motor front surface.

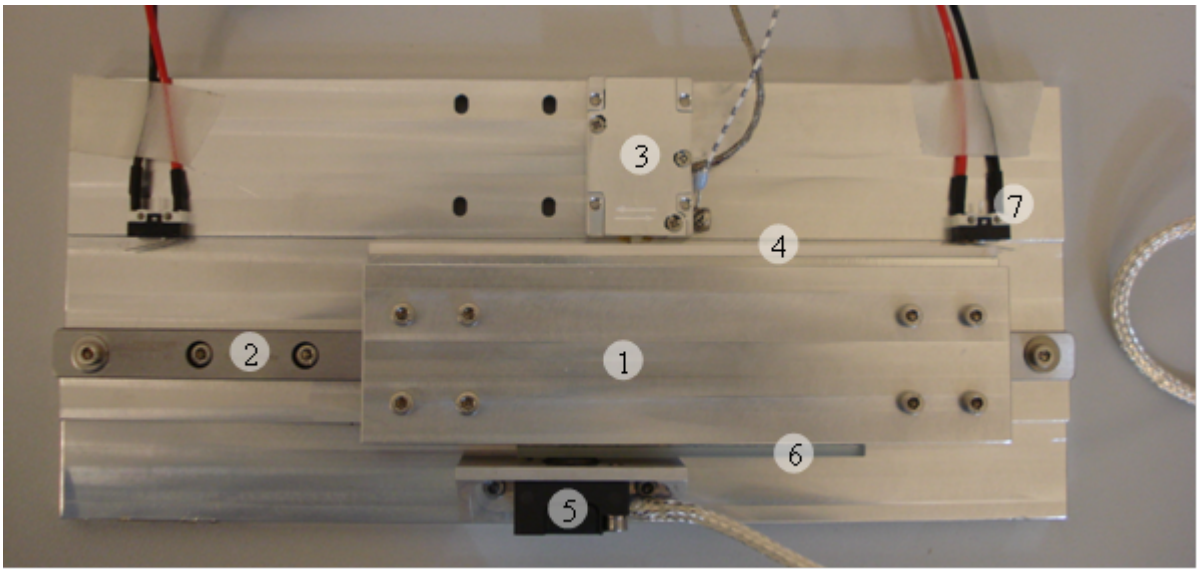

Figure 6.1: Experimental setup consisting of a slider (1) guided along a linear rail (2), a Nanomotion HR1 motor (3) and drive strip (4), a linear encoder consisting of an optical scanning head (5) and glass scale (6), and limit switches (7).

Linear guiding A Schneeberger Minirail system is chosen as linear guide way: a MN12 rail with a length of 245 mm with two MNN12 carriages. The two carriages are connected by a beam-like component to provide a slider with 150 mm length, needed to support the Nanomotion drive strip. The minirail carriages contain recirculating ball bearings to slide over the rail, which gives smooth and accurate linear motion and provides the runway accuracy in the side direction that is needed for the correct working of the Nanomotion motor. Besides, the minirail system supports the slider against the lateral preload force of the Nanomotion motor and the load of the slider.

Position encoder For the linear position measurement a Heidenhain LIF481V linear incremental optical motion encoder is chosen, mainly because it was easiest available at the moment. The measurement system consists of a linear scale with a length of 70 mm. An optical scanning head scans the surface of the scale and returns two harmonic signals that are interpolated to a TTL signal with 0.4 µm signal period. The maximum global error is ±3 µm over 1m scale length and the maximum local error ±0.08 µm within one signal period.

Driver With the motor comes a AB1A driver that converts a ±10 V DC analog input signal V_{in} to the high-voltage 39.6 kHz AC signals to the motor. This driver is the standard to use with these motors. The driver needs a 64 V DC power source with about 0.5 A max. This is delivered by a Delta power source.

Signal input/output Two input/output cards are used to realize control of the setup from a PC:

- National Instruments PCI-6052E for analog and digital input/output. This is used a.o. to send the +/- 10 V DC signal V_{in} to the driver.
- National Instruments PCI-6602 counter card. This is used to count the TTL signal from the encoder and translate it to a position value.

For the PCI-6052E, a BNC-2110 breakout box is used, and for the PCI-6602 a BNC-2121 breakout box. These boxes form the interface to which the various cables coming from the test setup can be connected.

V_{in} (V)	0	1	2	3	4	5	10
V_0 (V_{pp})	0	184	258	312	350	380	390
V_1 (V_{pp})	0	182	258	310	348	368	380
V_2 (V_{pp})	0	62	88	108	126	130	130

Table 6.1: Measured voltages on the motor electrodes for different DC driver input signals V_{in}. V_0 is the voltage applied to electrode 0, V_1 to electrodes 1 and 4 and V_2 to electrodes 2 and 3. All three are peak-to-peak values.

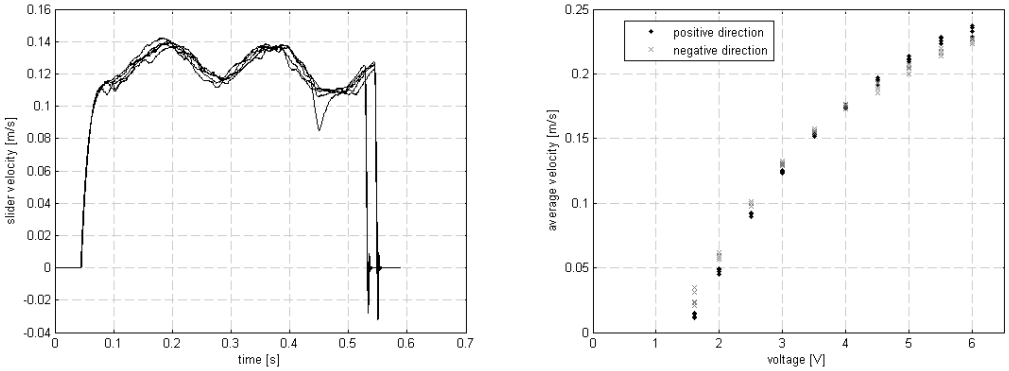

(a) (b)

Figure 6.2: (a) Velocity profiles (slider velocity $\dot{d}_{sl}$ against time) for several identical measurement runs with constant driver input $V_{in} = 3.0$ V; (b) average slider velocity $\dot{d}_{sl}$ against driver input V_{in}.

Load cell For several measurements, a load cell is used. This is a single-point load cell with a maximum load of 30N and an accuracy better than ±0.1 N.

6.2 Measurement description and results

Driver-to-motor signal To find the relation between the driver input signal V_{in} and the amplitude of the 39.6 kHz AC signals from driver to motor $\bar{V}_A$ and $\bar{V}_B$, the latter are put on a Tektronix TDS 1001B oscilloscope using a probe that reduces the voltage with a factor 10. As explained in the previous chapter, three wires lead from the driver to the motor: one to the electrode that covers the bottom surface of the motor (V_0), one to electrodes 1 and 4 on the top surface (V_1) and one to electrodes 2 and 3 on the top surface (V_2); by definition $V_A = V_1 - V_0$ and $V_B = V_2 - V_0$. Table 6.1 shows the measured signals against the input signal to the driver (V_{in}). The measured signals are harmonic signals and the values in the table are peak-to-peak values. The phase difference is 180° between V_0 and V_1 and 0° between V_0 and V_2. The measured values are stable and repeatable within ±2 V.

At the above measurements, the motor is actually connected to the driver, and the stage is kept at a stationary position. When the same measurements are done with the stage allowed to move freely, the measured voltages are up to 10% lower than with stationary stage.

Steady-state velocity measurements The most important characteristic of the motor is the relation between input voltage and no-load slider velocity. This is measured by sending a constant DC signal to the motor driver so that the slider moves from begin to end position. An example of the resulting slider velocity profile, for several identical runs with 3 V to the driver, is found in Figure 6.2a. In order to describe some relation between input signal and steady-state velocity, the average velocity between acceleration and

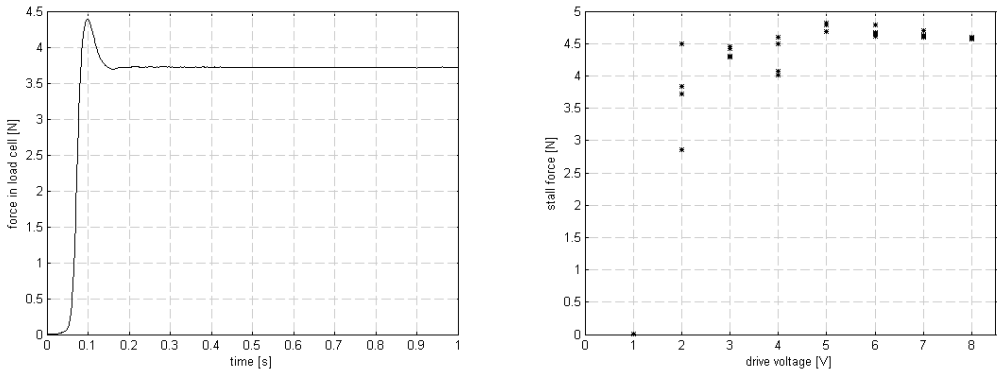

(a) (b)

Figure 6.3: Zero-velocity stall force measurements: (a) measured force against time for single measurement run; (b) stall force against drive voltage V_{in}.

deceleration is taken for each measurement run. The measurement is done for input voltages between 1.6 and 6 V, and each measurement is done 5 times in one direction and 5 times in the other direction. The results are shown in Figure 6.2b.

Static stall force measurements In addition to the steady-state velocity characteristic, also the stall force of the motor at zero velocity is measured. This is done in the following way: at $t = 0$, a signal is sent to the driver so that the motor pushes the slider against one end of the load cell, that is fixed to the environment at the other end. Figure 6.3a shows the force on the load cell against time for a single measurement run. The force measured by the load cell, after entrance effects are damped out, is interpreted as the static stall force of the motor. In Figure 6.3b the stall force is plotted against the drive signal, each dot corresponding to a single measurement.

Frequency response measurements Besides steady-state response, also the frequency response of the system is measured. To do that, a harmonic chirp signal is sent to the driver of which the frequency increases linearly from 10 to 200 Hz with 10 Hz/s increase rate. The amplitude of the chirp signal is 0.5 V on top of a 2 V 'offset' voltage. By using an offset voltage, it is made sure the velocity of the stage doesn't reach zero (the stage keeps moving), so that the dead zone in the motor behavior and the hysteretic stage friction don't influence the results. The transfer from drive voltage to slider velocity is determined by dividing the Fourier transform of the velocity by that of the input signal. The result is shown in Figure 6.4a.

Friction and preload characteristics To determine the preload force, the characteristics of the preload spring are determined by connecting the load cell at one end to the stage and push the stage such that the other end of the load cell is pushed against the finger of the ultrasonic motor in normal direction. See Figure 6.5a. The displacement of the stage is measured with the encoder. As a result, the measured force is plotted against the protrusion distance of the finger. The results are compensated for the deflection of the load cell itself. The results for several back-and-forth movements of the stage are shown in Figure 6.4b.

To measure the friction of the stage, again the load cell is connected to the slider and now it is pushed back and forth by hand, as shown in Figure 6.5b. This is done both with and without the motor mounted to the stage. The results are shown in Figure 6.4c and 6.4d. The results are compensated for acceleration forces using the measured position profile.

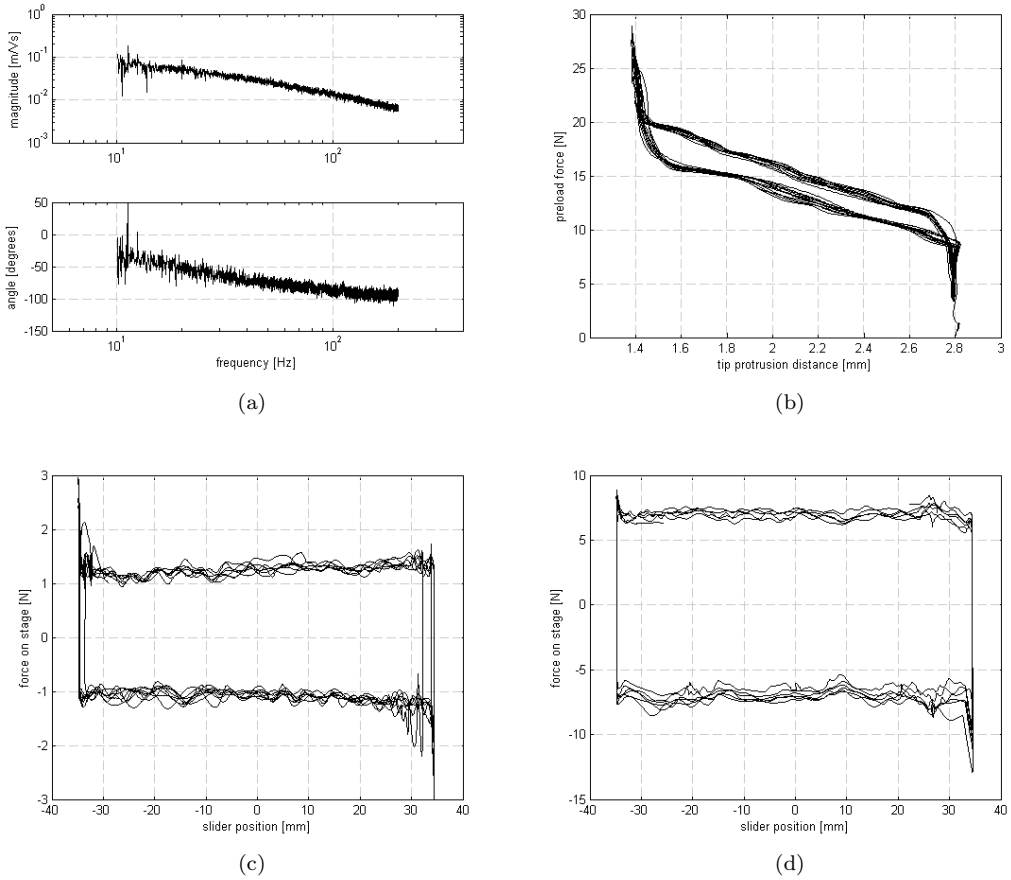

(a) (b)

(c) (d)

Figure 6.4: Various measurement results: (a) frequency response of the transfer from driver signal V_{in} to stage velocity $\dot{d}_{sl}$; (b) characteristics of the preload spring; (c) measured friction force f_{sf} in the guiding against slider position d_{sl}; (d) measured friction on the stage against slider position d_{sl}, with motor applied to the stage.

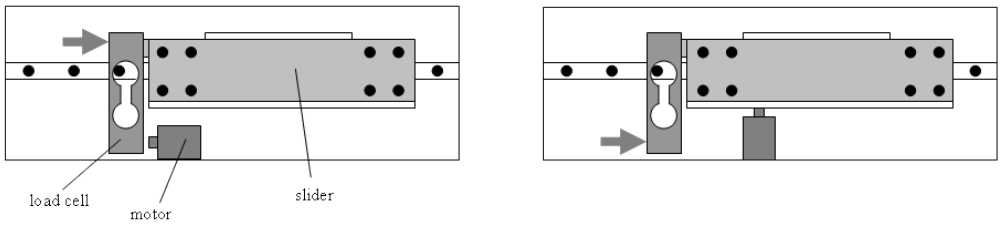

(a) (b)

Figure 6.5: Sketch of the experimental setup for (a) preload characteristics measurements and (b) stage friction measurements.

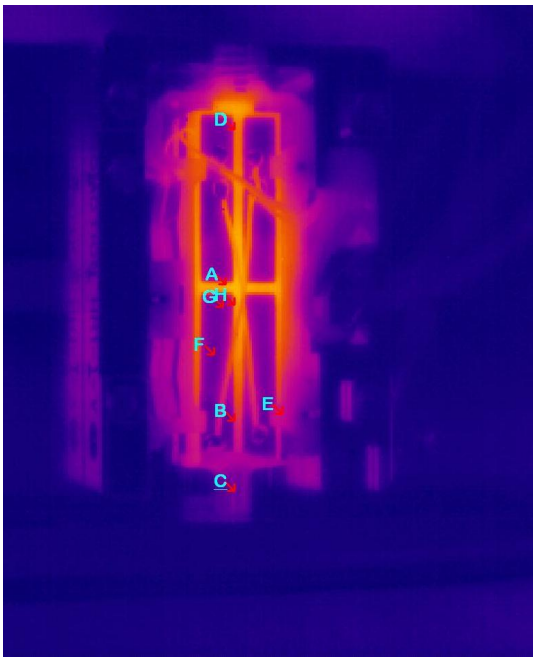

Figure 6.6: Infrared picture of the motor after a few minutes of continuous operation.

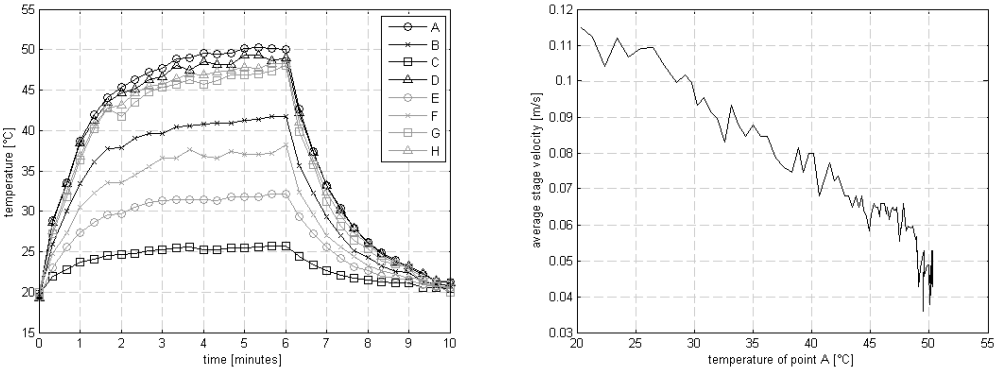

(a) (b)

Figure 6.7: (a) Temperature of several points on the motor surface against time for 6 minutes of continuous operation and 4 minutes of cooling down afterward. (b) Average slider velocity $\dot{d}_{sl}$ against the temperature of point A.

Temperature measurements Since transport of dissipated heat to the surroundings is one of the main challenges of the ultrasonic motor, the motor cover is removed and the inside of the motor is filmed by an infrared camera. In order to translate the measured infrared radiation to temperature, the surface emissivity of the various materials needs to be known. Emissivity values of some materials can be found on the Internet, but they are always a rough estimation and values for more exotic materials such as piezoelectric crystals are not found. Therefore emissivity values are determined experimentally, by observing several pictures taken by the camera at certain temperature difference between the object and the surrounding.

A test is done in which the stage is driven back and forth continuously for 6 minutes with an input signal of 3.0 V to the driver and a duty cycle of 70%. An example of a picture taken after a few minutes is found in Figure 6.6. The temperature at several locations on the surface of the motor parts is logged from the moment the stage started till 4 minutes after it stops; results are shown in Figure 6.7a. The point locations and numbering is as depicted in Figure 6.6.

During the test, the average velocity of the slider over a single full-stroke run is logged together with the temperatures. Figure 6.7b shows the average stage velocity against the temperature of point A: it is seen that the velocity decreases significantly for increasing temperature.

6.3 Interpretation

Determining model parameters The friction and preload characteristics measurements are used to determine three important parameters for the simulation model: the preload force f_{pl}, the guiding friction f_{sf} and the friction coefficient μ between the motor finger and drive strip.

Figure 6.4b can be used to estimate the preload force f_{pl} when the motor is mounted with a known distance to the strip. Obviously there is quite some hysteresis due to the friction in the linearly guided support of the piezo-body. It is assumed that the influence of this hysteretic friction is eliminated by the ultrasonic vibrations when the motor goes into operation, although no way is found to verify this experimentally. This means the preload can be estimated by taking the middle between the two 'lines' in the figure. An estimate value of 16.2 N is found in this way when the motor is mounted according to Nanomotion procedure, with 1.8 mm distance from the strip.

From Figure 6.4c it is seen that there is some variation in the guiding friction that seems partly reproducible and partly random. Both type of errors can be caused by for instance imperfections in the guiding. In the end, the average friction value, 1.1 N, is used in the simulations; even if the variations in friction force have significant influence on the stage velocity, this is canceled out by the fact that the stage velocity is also averaged.

Based on the results in Figure 6.4d, an average friction of 6.4 N acts on the stage when the motor finger is pressed to the stage. It can be assumed that the preload force of the motor doesn't influence the friction of the guiding, since the guiding is designed for much higher loads. Therefore the friction force caused by the finger is 5.3 N, which leads together with the 16.2 N preload force to an estimate of 0.33 for the friction coefficient μ according to Equation 5.12.

Steady-state characteristics In Figure 6.2a, the slider velocity at constant 3 V input varies roughly between 100 and 140 mm/s. This could be due to the variation in stage friction and effective friction between motor finger and drive strip, but since the velocity profiles show stronger repeatability than friction forces, there is likely another source.

The voltage-velocity characteristic shown in Figure 6.2b corresponds quite well to the manufacturer's specifications, shown in Figure 4.4. The measured velocities are even somewhat higher than expected, although the specifications are for a no-load situation while in the experiment some friction is present in the guiding. It is seen that the velocity is dependent on the direction of motion: at input signals below 4 V, the slider moves faster in negative than in positive direction; at input signals above 4 V it is the other way around. This behavior is seen even when the motor is removed and remounted on the stage several times, so this cannot be explained by mounting tolerances but it may be due to small production errors in the motor itself.

The results of the stall force measurements in Figure 6.3 could be strongly affected by the friction in the stage: the stall force exerted by the motor on the stage is not only compensated by the load cell, but also by static friction in the guiding. Furthermore, the measurements are done such that at $t = 0$ the slider is at a small distance from the load cell, so the slider hits the load cell with a certain velocity. The resulting inertia forces, together with the hysteretic friction, may be the reason for the large spreading in the results and lead to the conclusion that the measured values are no realistic representation for the actual stall force.

Frequency response In the frequency response of the transfer of input signal V_{in} to stage velocity $\dot{d}_{sl}$ (Figure 6.4a) it is seen that for frequency converging to zero, the amplitude converges to a finite value and the phase to zero, which refers to the fact that for a static input, the velocity always reaches a finite value due to the contact friction. In Figure 6.2b the steady-state (0 Hz) transfer magnitude, seen as the slope of the signal-velocity graph at 2 V, is about 0.08 ms^{-1}/V; the amplitude in the frequency response plot indeed seems to converge to approximately this value.

For higher frequencies, the amplitude changes to approximately a -1 slope and the phase to -90°, which corresponds to the force-to-velocity transfer for a simple mass system, in this case the slider mass.

Since the relation between input voltage and slider velocity in steady-state is not linear, the amplitude of the transfer is valid only for this specific input voltage, not for any harmonic input signal.

Thermal behavior For the thermal measurements, the the method with which the emissivity values of the observed surfaces are determined is not very accurate: the uncertainty in the resulting values can account for an inaccuracy of approximately ±25 % in the final values of measured relative temperature (relative to the ambient temperature), although the accuracy of the values relative to each other is better. Designing a test to determine the emissivity values more accurately is beyond available time and resources.

Figure 6.7a provides some insight on how the temperature is distributed over the piezo-body and other motor parts. The temperature of the piezo-body close to the finger (point B) is significantly lower than in the middle (point A) and the back (point D), which indicates that the conductive heat transport through the finger tip plays an important role in the motor cooling. Although from the simulation results it was seen that most of the energy is dissipated in the contact area, no local temperature increase is seen around the tip, but this is possibly due to the moving slider providing conductive cooling.

Despite inaccuracies in both the temperature and average stage velocity values, it is clear that the motor performance decreases significantly when the temperature increases. This is likely due to the temperature-dependency of the resonance frequency, as described in Section 4.2, although further investigation and more accurate measurement results are necessary to validate if this is really the (only) explanation of the observed behavior.

Since a thermal simulation model of the motor is not yet built, these results do not play a role in the model validation, but they provide some insight on the motor behavior that is in any case valuable when applying the motor in a stage design. Performing more accurate and extensive experiments is recommended.

6.4 Model validation

6.4.1 Electric behavior

By definition of the used method, the experimentally determined signals V_0, V_1 and V_2 are translated to the input voltages V_A and V_B of the simulation model according to:

$$V_A = V_1 - V_0$$

$$V_B = V_2 - V_0$$

If this is applied to the measured values in Table 6.1, taking account the phase shift between the signals, the relation between input signal on the driver and motor signal amplitudes $\bar{V}_A$ and $\bar{V}_B$ is as shown in Figure **??**.

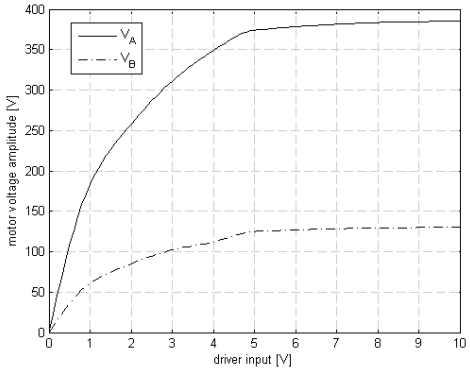

Figure 6.8: Relation between driver input V_{in} and motor voltages V_A and V_B.

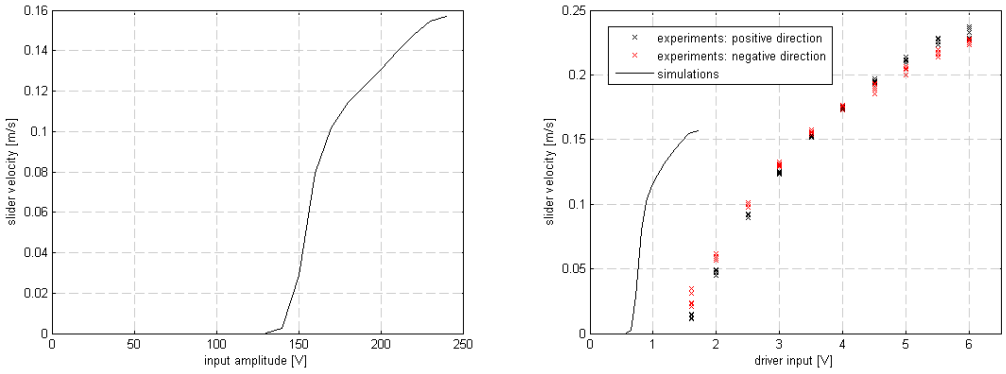

(a) (b)

Figure 6.9: (a) Voltage-velocity characteristic ($\dot{d}_{sl}$ against $\bar{V}_A$) of the final set of simulation results. (b) Comparison of input-velocity characteristics ($\dot{d}_{sl}$ against V_{in}) from simulations and experiments.

In the simulation model it is assumed that when driving the motor using V_A, V_B is always zero, in other words: two of the top electrodes are shorted to the bottom electrode. This is clearly not a valid assumption: in the measurements the V_B is always 32.9% ± 0.9 of V_A, with 0° phase difference. It is not known if this is actively done by the driver (for instance to optimize the motor performance) or caused by the backward piezoelectric coupling in the motor.

The assumption that the voltage is purely a system input prescribed by the driver is also not a valid assumption since the voltage over the electrodes is shown to be dependent on the slider velocity. A difference of 10% in motor voltage is shown between the two 'extremes' (namely stationary slider and free moving slider). This is due to the backward piezoelectric coupling: this makes the voltage on the electrodes dependent on the motor velocity and applied load, much like the two-way coupling of the motor constant of an ordinary electric motor, creating a back EMF.

6.4.2 Steady-state system behavior

To compare steady-state system behavior of the simulation model with the experimental results, simulations are run with the set of parameters obtained from experiment: 1.1 N friction force on the stage, 16.2 N preload force and a friction coefficient 0.33 in the contact zone. Furthermore, the applied voltage is now such that $V_B = 0.33V_A$; even if this is in reality not actively done by the driver, it is a better assumption than the

$V_B = 0$ assumption. The only parameter that doesn't correspond with the experimental setup is the slider mass: the slider mass in the simulations is 10 g, 30 times lower than in the experimental setup, in order to speed up the simulations. This shouldn't influence the steady-state characteristics. Again simulations are done for a range of input amplitudes.

In Figure 6.9a the results of these simulations are shown and in Figure 6.9b they are compared to that of the measurements, expressed in a graph with on the x-axis the signal to the driver V_{in} and on the y-axis the resulting slider velocity $\dot{d}_{sl}$. For the simulation results, the applied motor voltage amplitude $\bar{V}_A$ is translated to a driver input V_{in} using the relation shown in Figure 6.8. Clearly, the simulation results are very different from the experimental results. The main differences can be described as follows:

1. The dead zone is underestimated in the simulations by about a factor 2.
2. The maximum velocity is significantly lower than the maximum velocity in the measurements.
3. The maximum voltage for which the simulation model works 'correctly' is a factor 3 lower than the maximum voltage used in the measurements.

In comparing the results, several limitations of the simulation model should be taken into account. Firstly, an important reason for the differences is the fact that the simulation model doesn't take into account the backward piezoelectric coupling, neglecting the influence of the slider velocity on the voltage on the motor. The relation between the driver input V_{in} and the motor voltage V_A is measured with a stationary stage, while for moving stage the measured motor voltages are lower. Taking this into account in the translation from $\bar{V}_A$ in the simulations to V_{in}, this would lead to a scaling of the simulation results along the x-axis with a positive factor. This would explain differences '1' and '3' to a certain extent: in the experiments, $\bar{V}_A$ is up to 10% lower for moving slider than for stationary slider, and scaling all simulation results with 10% over the x-axis would clearly explain only part of the difference. Unfortunately the relation between V_{in} and $\bar{V}_A$ is not measured in detail for free-moving stage, because the limited stroke of the stage is a practical problem for this measurements.

In the second place, the simulation model can only be used up until the point where the contact between the finger and strip is broken; at that point the simulation model produces a negative normal force in the contact, which has no physical meaning. In reality however, it could be that the finger indeed disconnects from the surface without the motor losing performance. This could be the reason for difference '2' and '3'. Unfortunately, with the current experimental setup it is not possible to check if this is the case.

Further differences can be explained by the various assumptions and simplifications done in the model. The most important are listed here.

Plane stress assumption In the previous chapter it is shown that the plane stress assumption, when compared to a full 3D model, has only little influence on the second bending resonance frequency and the static body deformations. This doesn't necessarily mean that this is also a valid assumption in the full simulations. Probably the real motor behavior is influenced by higher resonance modes or out-of-plane resonance modes that cannot be (accurately) described by the plane stress model. It is however assumed that, since the second bending resonance dominates the motor behavior, these influences are small and therefore using a plane stress model is justified. The only way to validate this is to perform simulations with a 3D model.

Simplified contact model Assuming Coulomb friction, a single contact node and an infinitely stiff counter-surface is inevitably a simplified representation of reality. For now it is not possible to say how this affects the simulation model behavior. The friction coefficient μ is already shown to have influence on the resonance, the maximum slider velocity and the dead zone, so all these things will also be influenced if a completely different contact model is used.

Optimum frequency assumption Figure 5.3b shows that the optimum drive frequency in the simulations, after correction, is 39.6 kHz. However, as shown before the optimum frequency is influenced by the stick-slip friction in the contact and dependent on the friction coefficient. Since the amplitude of the input signal

influences the ratio in which the stick- and slip phases are present in the solution, it is likely that the optimum frequency is not the same for each input amplitude. This hypothesis is not yet validated by simulations, nor is it known if this can be observed in the real motor.

In determining the optimum frequency, simulations are done with $\bar{V}_A = 150$ V (corresponding to 0.73V driver input in the figure), so in a way the model is optimized on this voltage. It is possible that 'optimizing on a different voltage' leads to better results.

Material properties Overestimation of the material damping could be an explanation for the fact that the maximum velocity is lower than expected. However, for a specific situation it is shown that if the damping factor is reduced, the resulting velocity increases only with about 10%. Therefore this is not likely to be a significant error source.

Underestimation of the strength of the piezoelectric coupling could also be a possible error source. Due to the linearity of the equations, scaling the piezoelectric coupling matrix leads to the same results as scaling the applied voltage. Therefore, the result of a deviation in the piezoelectric coupling characteristics of the material is simply shown by scaling the x-axis of the voltage-velocity graph. However, for several different piezoelectric materials found in literature, the difference in effective piezoelectric coupling is at most $\pm 5\%$ compared to the currently used, so again this is not likely to be a significant error source.

The dead zone is the result of the fact that for low voltage, the traction force in the contact is not high enough to overcome sticking. Therefore, underestimating the dead zone could be due to underestimation of the friction coefficient in the contact or the guiding friction. However, in the previous chapter it is shown that a higher friction coefficient lead to a lower maximum velocity at least in simulations with a frictionless stage, so this conflicts with difference '2'.

Slider friction and preload force The slider friction obviously influences the velocity of the stage. However, the fact that the maximum velocity in the simulations is too low points to overestimation of the friction, while the fact that the dead zone is too small points to exactly the opposite.

The preload force is another parameter that could have some influence. However, experiments show that the influence of the preload force on the motor performance is very small. Inaccuracies in the determined values for the slider friction and preload force therefore are not likely to be a significant source of error.

6.4.3 Dynamic system behavior

The simulation results in (Figure 5.4b) show that the velocity 'slowly' increases from zero to a steady-state value with a step on the input of the motor. A time constant τ can be defined as the time where the velocity reaches 63% of its end value; about 1 ms in this specific situation. As a rule of thumb, the 'bandwidth' of such a system, the frequency at which the transfer is decreased by 3 dB, can be obtained by:

$$\omega_{bw} = 2\pi F_{bw} = \frac{1}{\tau}$$

This would lead to a bandwidth of approximately 150 Hz, while from the measurements in Figure 6.4a the bandwidth seems to be roughly 20 Hz. This difference is explained by the fact that the slider mass used in the simulations is 30 times lower than that in the experimental setup, which clearly increases the time constant. It is not exactly known how much influence an increase in the mass will have on the time constant in the simulations, since the (mechanical) inertia of the system is only partly from the mass of the slider, and partly from the inertia of the piezo-body itself. The last is seen in the fact that the amplitude of the finger tip vibrations in the simulations also increases 'slowly'.

The fact that possible dynamic aspects of the driver electronics are not taken into account may also cause a difference between the experimental and simulation results. More experiments and simulations are needed to validate the dynamic behavior of the simulation model.

Chapter 7

Conclusion and recommendations

7.1 Conclusion

For a necessary redesign of the X-stage in the e-beam lithography machine developed at Mapper Lithography B.V., a comparison is made between several design alternatives. A concept in which piezoelectric motors are used as actuators is chosen as the most advantageous alternative. A literature survey on the topic of piezo-motors showed that not enough is known yet about the behavior of these motors to prove the feasibility of the concept.

Therefore a finite element model is built of a specific motor, that simulates the deformations in the core part of the motor and the resulting displacement of the slider. The model is based on linear structural and piezoelectric equations and a point contact between the motor and slider coupled by Coulomb friction. Dynamic analyses are done to simulate several aspects of the complex motor behavior. The results prove that the model is capable of simulating the base mechanisms on which the working of ultrasonic motors is based, namely the generation of ultrasonic vibrations in a piezoelectric structure by applying an AC voltage, and the translation of these vibrations into linear velocity of a guided slider through frictional stick-slip contact. The resulting linear slider velocity is in the expected order of magnitude.

The simulation model is validated by doing experiments on a test setup specifically designed for this purpose. It is shown that the simulation model is able to predict behavior of the motor up to certain extent, but in a quantitative manner the simulation results do not yet correspond to the experimental results: when the 'voltage to no-load velocity' characteristics of the simulation model are compared to the experimental results, the maximum velocity is too low, the dead zone is underestimated and the velocity 'collapses' already at relatively low input voltage. Furthermore, the input frequency in the simulation model at which the necessary resonance is excited, is significantly higher than in reality. The main reasons for these differences are presumably:

1. Neglecting the dynamics of the structure that supports the piezo-element in the motor housing.
2. Neglecting the backward piezoelectric effect and the electro-dynamic behavior of the driver.
3. The inability of the simulation model to simulate breaking of the contact.

Further work on the simulation model is recommended before it can be used in design and optimization processes.

7.2 Recommendations

7.2.1 Further work

The first focus should be on further developing the simulation model so that it will give results that are closer to the values found by experiment. Therefore the following is proposed:

1. Since it is shown that the frequency and shape of the resonances in the motor are strongly dependent on the way the support structure is modeled, the dynamics of the support structure should be analyzed and included in the simulation model. Analyzing the dynamics can be done by including the geometry of the support structure in the finite element model, but eventually it is preferable to model them in the form of a simplified mass-spring structure that doesn't add too much degrees of freedom to the model.
2. The backward piezoelectric coupling should be included in the model since this is seen to affect the voltage on the motor electrodes significantly in reality. If this is done under the assumption that the complete potential distribution over the surface of the piezo-body can described by only the motor voltages V_A and V_B, it adds only 2 degrees of freedom to the model so it doesn't make the simulation model significantly more complex. The driver should then be included in the model, because the influence of the backward piezoelectric coupling on the motor voltage cannot be described without knowing the electrical properties of the driver. The DC driver input V_{in} will then be the input of the model.
3. It should be verified how much the simulation results are influenced by the choice for a contact and friction model. If this influence is significant, more investigation to ultrasonic contact mechanics in ceramic materials is needed, using literature or experiments, and a contact model should be used in the simulations that approaches the real contact phenomena more closely than the current assumptions of point contact and Coulomb friction.
4. An experiment should be designed to investigate whether or not the contact between the motor finger and drive strip is broken in reality. If so, the simulation model should be adjusted such that it can handle this situation.

The second focus should be on building a thermal model, overheating is one of the main threats in the use of the ultrasonic motor. The existing model can be used to evaluate several forms of energy dissipation, but a 3D finite element model of the motor should be built, including conductive, convective and radiative heat transfer, to investigate temperature and heat transfer.

Finally, more effort could be put in model reduction. In the current stadium, several time-consuming simulations are needed to show the basic motor behavior even in a single situation, and this should be repeated each time a certain parameter is changed. This makes the simulation model quite impractical for extensive research. An attempt to reduce the model by modal superposition didn't lead to a working model yet, but further attempt in this direction or another may lead to a significantly faster model.

7.2.2 Practical use of the simulation model

Since the results of the simulation model are clearly not in accordance with reality, it is not yet possible to use the model for accurate prediction of different aspects of the motor performance in a design process. However, results so far show several possibilities:

1. With the current model, energy dissipation due to structural damping, contact friction and dielectric loss can be easily observed by postprocessing using the simulation results. This can be used to predict temperature rise and heat flows, giving a clearer view on the danger of overheating and possible solutions to this. Evaluation of the energy dissipation in the simulations for instance showed that most of the energy is dissipated in the frictional contact.
2. The simulation model outputs the exact forces in the contact between the motor finger and drive strip. This can be used to predict vibrations on the stage and maybe to predict wear in the contact area.
3. With the current model it is easy to observe stress distributions throughout the motor, so that possible failure mechanisms can be predicted.

Since parameters in the simulation model can be easily changed, the above things can not only be observed for a specific situation, but also the influence of changes in the design or operation of the motor on these things can be investigated. In the process of designing a stage with ultrasonic motors, optimizing the design of the motor itself will probably be beyond the possibilities, but for instance optimization of the controller

settings, selecting a material with different friction properties for the drive strip, optimizing the preload force with which the motor is mounted to the stage or reducing overheating problems by adding a coating to the motor parts are good examples of possibilities in a design project. These are all things of which the influence on the motor behavior could be shown with the simulation model (some already with the current model, some after expanding the model), which makes the model in the future a powerful tool in optimization processes of this kind.

7.2.3 Design recommendations

The required stage moves with a constant velocity most of the time. With basic calculations it can be shown that, in theory, for accelerating and decelerating the stage according requirements about 10 Nanomotion HR1 ultrasonic motors would be needed, while 2 motors would be enough for the steady-state part to overcome the stage friction. This means that 8 of the 10 motors are not necessary for most of the time and traveled distance. If the motors could be actively decoupled from the stage during operation, it would be possible to control the stage such that during the acceleration all 10 of the motors are used, while during the constant-velocity scanning, only 2 at a time are used. This would provide some big advantages:

1. Since, based on knowledge from literature, the wear in the USM contact area is expected not to be dependent on the delivered force, wear and particle generation decrease directly with the number of motors used, even though the delivered force per motor increases.
2. If the motors are alternately responsible for the constant speed part, the duty per motor is quite low. In this way, the motors don't age very fast; the total lifetime of the module is much higher than the lifetime of each of the motors. This also prevents problems with overheating since each of the motors stands still for most of the time. This is not entirely compensated by the fact that the force per motor is increased.
3. If one of the motors breaks down, the duty could automatically be adjusted so that the broken motor becomes idle. In this way, the remaining motors continue to do the work so that machine can maintain operation, though with somewhat less performance, until maintenance is done. It is also possible to build in spare motors.

If a stage is designed with ultrasonic motors, it is therefore recommended to further investigate this concept. Further investigation should focus on the following things:

1. Verifying if there is enough motor stiffness during the constant-velocity scanning motion if only a few motors are used (in the above calculation, only the required force is taken into account, not the required stiffness).
2. Investigating the influence of the coupling/decoupling action on the motor performance. Typical issues could be: sudden unwanted accelerations on the stage, local wear increase and degradation of the drive strip or high contact forces affecting the lifetime of the motors.

Appendix A

Literature study to topics related to compact stage design

This appendix contains the result of an earlier literature study to topics possibly related to the design of the required stage. The information that was found on these topics was used to define and consider the different design concepts in Chapter 3 of the report, although some of the topics were eventually not quite relevant in the design considerations.

A.1 Contents

There are two main solutions to the problem of building a precision stage in a vacuum tank: either drives have to be found that are able to operate in the vacuum environment, or drives are to be placed under the vacuum chamber and motion should be transferred to the inside via a feedthrough mechanism. This requires a state-of-the-art research for the following topics:

- High-precision actuators in vacuum
- Feedthrough mechanisms
- Transmission mechanisms
- High-precision stages in vacuum
- Errors and vibrations in high-precision (vacuum) positioning systems

Furthermore, the challenge of avoiding the magnetic field production in the vacuum chamber requires a study to the following topics:

- Magnetic field production of typical electric drives
- Principles of magnetic shielding

A.2 Important issues and limitations in high vacuum environment

Common modern applications for which high precision motion in a high vacuum environment is needed are [7]:

- thin films coating equipment
- electron an ion lithography
- molecular epitaxy

- surface research
- ...

Lots of literature can be found on mechanical systems in a high vacuum environment. Important issues in high vacuum environment are:

- Friction: friction in vacuum environment is significantly different, usually higher, than in atmospheric environment. Besides, due to wear material particles are being freed, contaminating the vacuum environment.
- Outgassing: outgassing of materials contaminates the vacuum environment. This introduces limitations on the types of materials that can be used and on temperatures.
- Leakage of air from the outside through feedthrough holes.
- Heat production: since there is no air to remove the heat produced by for example a motor, overheating is a problem.

Outgassing Outgassing is the process where gases trapped in a solid are freed in a vacuum environment, or where particles at the surface of a solid react with the still present gas particles to form a new gas. Outgassing is a challenge in high-vacuum applications because the quality of the vacuum is affected by these gases. In applications where a vacuum environment is demanded, usually requirements on the outgassing rate are set. These are usually specified in mbar L/s. In some applications, several requirements for the outgassing of different materials are set, because certain materials contaminate the application more than others.

A well-known remedy against unwanted outgassing in high-vacuum applications is 'baking': before the system is running, the components are heated to usually a few hundred degrees, to speed up the outgassing and thus remove most of the gases and particles from the material before the machine gets in operation.

A.3 Actuators in high vacuum environment

Possible actuators to use in high vacuum environment are:

- linear or rotary electric motors
- piezoelectric drives
- a hydraulic piston.

A.3.1 Electric motors

Not many examples are found of electric motors that are suitable for high-vacuum environment. An example is a linear electric motor manufactured by Anorad [29], which is suitable for environments up to 10^{-7} mbar. Although linear electric motors are very suitable for precise positioning applications, the inevitable production of magnetic stray fields is a problem in e-beam applications. Anorad offers solutions specifically for scanning e-beam lithography applications, but these are based on external linear drives with through-chamber rods. No examples are found of electric motors used directly in a vacuum environment in e-beam applications.

A.3.2 Piezoelectric drives

(The topic of piezoelectric drives is covered in Chapter 4 of the main report.)

A.3.3 Hydraulic actuators

Hydraulic systems are not often used for high-precision applications. This may be because the speed and accuracy of such systems normally is limited by for instance the high viscous friction forces or the slowness and inaccuracy of mechanical valves.

However, in [7] Deulin proposes a hydraulic valve controlled by magneto- or electrorheology. This principle is based on increasing the viscosity of a suspension by applying a magnetic or electric field. The suspension consists of a carrier liquid (for example vacuum oil) containing particles that are attracted by the magnetic or electric field, creating a local accumulation of particles that works as a kind of valve. The time constant for this principle is in the order of 1 ms for MR and 0.1 ms for ER. With this principle, flows can be controlled for the control of high-precision hydraulic actuators.

A schematic view of a long travel magnetic rheology drive is seen in figure A.1. An object (1) is moved along a guide (2), actuated by two hydro-cylinders (3). The suspension is pumped from a spillage tank to the distributor (4) by a pump (5). The distributor contains four magnetorheology 'valves' (K1 to K4) that control the motion of the stage: opening of K1 and K3 causes the stage to move right and opening of K2 and K4 causes the stage to move left. Closing all valves fixes the stage at a certain position; the pumped liquid is then directly fed back to the spillage tank through safety valve (6). Since the rheology valves are not limited to two states ('opened' and 'closed'), but are able to vary the local viscosity in a continuous range, the force on the stage can also be varied continuously.

The advantage of rheology drives over piezoelectric drives is the smoothness of action: long-stroke piezoelectric drives are always based on stepwise motion. Also, when ER is used, no magnetically charged particles or electrical current is present inside the vacuum chamber, so no magnetic fields will be produced at all. The advantage of rheology drives over conventional hydraulic drives is the smaller time constant and higher precision, due to the use of rheology valves instead of mechanical valves.

The drive in figure A.1 was invented in 1993 Deulin et. al. [4]. It is based on magnetic rheology, has a stroke of 200 mm and according to [30], the accuracy is 0.2 μm and the time constant about 1 ms. The cylinder is sealed with deformable bellows providing a hermetic seal, which makes the drive able to operate in high vacuum surroundings. In [31] further information on testing this device is published. The maximum transporting velocity is in the order of 100 mm/s [7]. Apart from this example, no literature is found on magnetic or electric rheology precision drives and no manufacturers of such drives exist to the knowledge of the author.

When electric rheology is used instead of magnetic, the viscosity of the fluid is somewhat lower, making it even more fast and accurate but lowering the maximum exerted force on the stage.

A.4 Feedthrough mechanisms

In order to transfer mechanical motion from outside the vacuum chamber to the inside, a so-called 'feedthrough mechanism' is used. The two functions of these mechanisms are the transfer of motion and the sealing of the chamber. Lots of different mechanisms exist. Some are based on just feeding a shaft through the wall and sealing the gap; in this case the sealing usually is not hermetic. Others are based on more complicated transfer mechanisms between an incoming and outgoing shaft, allowing perfect (hermetic) sealing with flexible elements.

In [7], a number of different feedthrough mechanisms is observed. They can be divided in two types: hermetic and non-hermetic feedthroughs. Some transfer linear motion, others rotary motion. Usually linear feedthroughs are not as perfect as rotary feedthroughs, because it is difficult to provide high vacuum sealing for long-stroke linear motion. Table A.1 gives a list of feedthrough mechanisms with their most important characteristics.

A.4.1 Hermetic feedthrough holes

Simple bellows-sealed rotary motion feedthrough A schematic view of this feedthrough mechanism is shown in figure A.2. This mechanism provides feedthrough for rotary motion. From both sides, the rotating

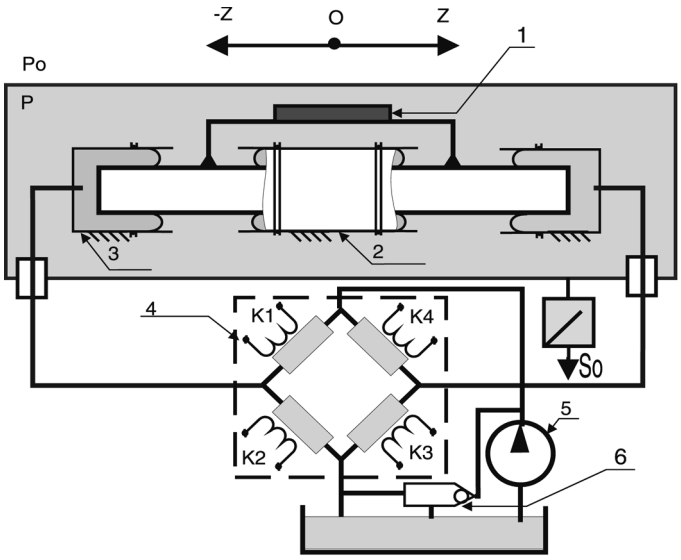

Figure A.1: Long travel 1-DOF magnetic rheology drive

type	DOF	trans-mission	seal	details
simple bellows-sealed rotary motion feedthrough	1: rotary	1:1	hermetic	trade-off between longevity of bellows and bearings
harmonic gear rotary motion feedthrough	1: rotary	gear	hermetic	no trade-off; in-built gearing
simple bellows-sealed linear motion feedthrough	1: linear	direct	hermetic	stroke limited by extension of bellow
magnetic linear-rotary motion feedthrough	2: linear + rotary	1:1	hermetic	linear stroke depending on length of tube; allowable force limited by magnet
non-coaxial nut-screw linear motion feedthrough	1: linear	gear	hermetic	low wear, high precision, high rigidity
differentially pumped feedthrough	2: linear + rotary	direct	pumped	non-perfect sealing, high power consumption due to pumping
magnetic fluid feedthrough	1: rotary	direct	fluid	excellent sealing, high rotational speeds allowed

Table A.1: List of hermetic feedthrough holes and their most important characteristics

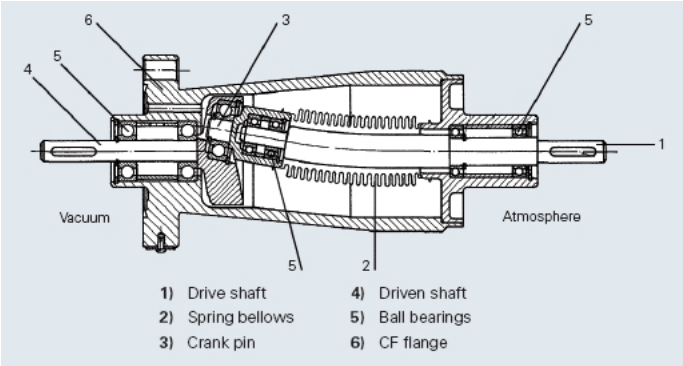

Figure A.2: Bellows-sealed rotary motion feedthrough (source: [32])

shaft (1,4) is connected to an eccentric bus and pin (3) that doesn't rotate itself. A bellow (2) is hermetically connected to the bus and the surrounding chamber wall (6), providing a perfect vacuum sealing.

In this types of feedthroughs, the eccentricity is a critical factor in the design. In order to keep the forces in the bearings small, the eccentricity should be as high as possible, but this negatively influences the longevity of the bellows. A trade-off should be made, depending on the requirements of the application.

Lots of companies produce bellows-sealed rotary motion feedthrough mechanisms. VG Scienta, a producer of vacuum equipment, produces several feedthroughs of this type, all having either a stepper motor or knob for manual operation included [8]. The specifications of the motor-driven types are the following:

- maximum speed: 165 to 500 rpm
- allowable torque at maximum speed: 0.12 to 0.8 N, the highest corresponding to the one with the lowest maximum speed and vice versa
- resolution: 0.1 to 0.9 rad
- outer diameter: 34-70 mm

Some of these feedthroughs allow limited motion in axial direction, up to 24 mm.

Also, this company provides a low-speed high-precision motorized feedthrough:

- maximum speed: 2.0 rpm
- max axial load: 130 kg
- max radial load: 10 Nm
- resolution: 0.0075 degrees
- outer diameter: 114 mm

Magnetic feedthrough A magnetic feedthrough is shown in figure A.3. This mechanism is based on magnetic coupling between the elements inside and outside the vacuum tank. Sealing is provided by a tube of rigid non-magnetic material (1). A shaft inside the tube (3) and a ring outside the tube (2) are coupled via permanent magnets, so that motion transfer from outside to the inside is possible. Magnetic feedthroughs can allow movements in 2 degrees of freedom: rotary motion and linear motion along the axis of rotation. However, magnetic feedthroughs that allow only rotations also exist.

Magnetic rotary motion feedthroughs usually can handle bigger torques than bellow-sealed mechanisms. Also, when the maximum torque is exceeded, the magnets just will 'cog' to the next position, so no physical damage will occur. VG Scienta provides magnetic feedthroughs for only rotary motion with the following characteristics [8]:

- maximum speed: 500 rpm

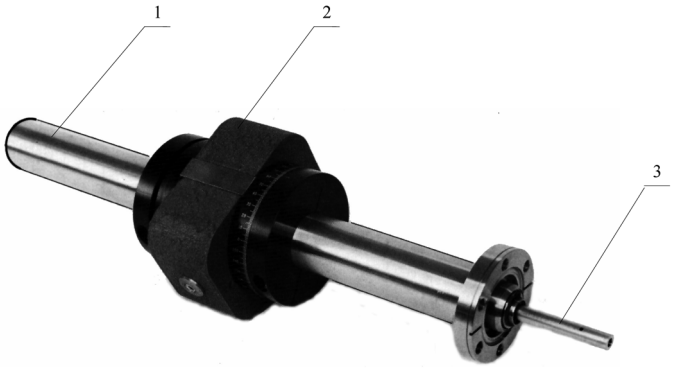

Figure A.3: Magnetic feedthrough mechanism (source: [7])

- maximum torque: up to 5.0 Nm
- outer diameter: 70 mm
- minimum pressure: 10^{-10} mbar

Also, magnetic feedthroughs that allow both rotary motion and linear motion, with the following characteristics:

- maximum torque: 1.0 Nm
- maximum load: 2.1 kg (shaft assumed horizontal and fully extended)
- linear stroke: 1450 mm
- outer diameter: 70 mm
- total length: 1845 mm
- minimum pressure: 10^{-11} mbar

No literature is found on this type of feedthroughs.

Harmonic gear rotary motion feedthrough The harmonic gear rotary motion feedthrough is introduced by Y. Hayashi and T. Yamada in [33]. It is based on a harmonic gear, of which the working is shown in figure A.4b. The input shaft is connected to a ellipsoid 'wave generator'. A flexible element, the 'flexspline', is connected to the wave generator via a roller bearing so that it follows the ellipsoid form. The outside of the flexspline contains teeth connected to teeth in the inside of the surrounding 'circular spline' that is fixed to the environment. The number of teeth of the flexspline is less than that of the circular spline, so that the flexspline moves a little in the opposite direction of the shaft for each shaft revolution.

In the harmonic gear rotary motion feedthrough (figure A.4a), the wave generator consists of two eccentric ball bearings (2, 2a) on the input shaft (1), and instead of the flexspline, the circular spine (4) is rotating and connected to the output shaft (5), while the flexspline (3), that also has the function of vacuum sealing element, is fixed to rotation.

The harmonic gear provides a big reduction of rotational speed, which can be beneficial in some applications. The position accuracy is excellent. A critical factor is fatigue in the flexspline, limiting the lifetime. In [33] a lifetime of over 2 x 10^5 revolutions was found when an input speed of 1000 rpm, a reduction factor of 1:101 and a load of about 20 Nm was used. This type of feedthroughs is able to seal vacuum environments in the order of 10^{-8} ~ 10^{-10} mbar [33], dependent on the input rotational speed..

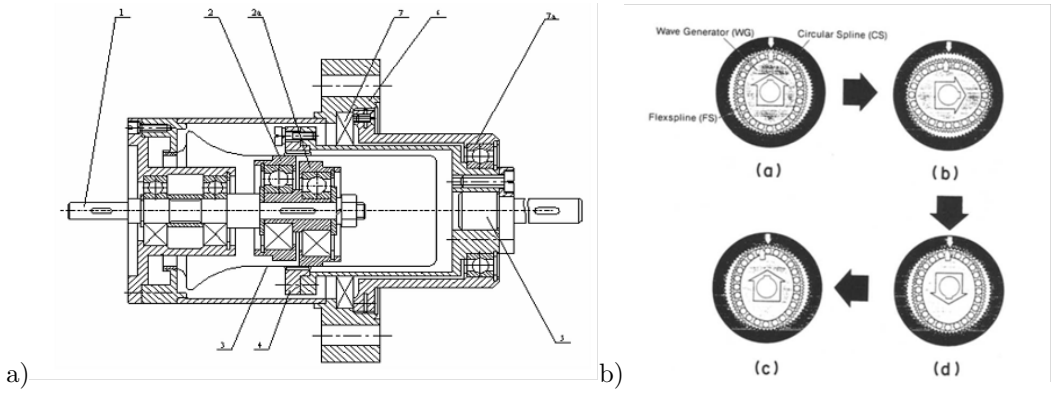

a) b)

Figure A.4: Harmonic gear rotary motion feedthrough: a) schematic view (source: [7]); b) wave motion generated by harmonic gear (source: [33])

Simple bellows-sealed linear motion feedthrough This feedthrough mechanism consists simply of a shaft that is able to make a linear motion through the vacuum wall, and a bellow connected between the shaft and the wall, sealing the opening hermetically. Obviously, the stroke is limited by the bellow. According to [7], arc-welded bellows can extend to 200% of their initial length.

Performance specifications like maximum load or accuracy purely depend on the shaft itself and its bearings and not on the sealing mechanism.

Non-coaxial nut-screw couple feedthrough With this feedthrough mechanism, a rotation is transferred into a translation. The rotation of a bush with an eccentric hole sets a nut in motion in a circular path, without rotation. The inside of the nut contains zero-pitch thread that acts on a non-rotating screw, setting the screw in linear motion. The sealing is done by connecting bellows between the wall and a non-rotating ring between the bush and the nut.

A.4.2 Non-hermetic feedthrough holes

In the hermetic feedthrough holes, the motion was always transferred indirectly, either via extra moving parts (in case of most bellow-sealed feedthroughs, because of the need for a non rotating part to connect the bellows to) or with no physical connection at all (in case of magnetic feedthroughs). The only exception is the bellows-sealed linear motion feedthrough, in which the bellows actually is connected directly to the shaft, but this prevents rotational motion and allows translation only with limited stroke.

In non-hermetic feedthrough holes, the shaft is directly fed through the vacuum chamber wall, which has several benefits: the allowable torque is higher (just dependent on the shaft itself, not on the sealing mechanism) and there is no position error in the transferred motion. Sealing in general is less perfect than for the hermetic seals. Two kinds of feedthroughs are discussed here: differentially pumped feedthroughs and feedthroughs with magnetic fluid seals.

Magnetic fluid feedthrough Magnetic sealing is introduced in [34]: the basic principle of magnetic sealing is explained and several different designs with minor differences are shown. A schematic view of the magnetic fluid feedthrough is found in figure A.5. The principle is based on sealing with thin 'rings' of fluid in which ferromagnetic material particles are suspended. An shaft (2) is mounted in the housing (1) with normal bearings (3). Permanent magnets (4) are mounted in the housing, creating a magnetic circuit (9) via the shaft, that holds the fluid rings (8) in its place.

Magnetic fluid seals are able to provide perfect (zero leakage) sealing for rotational motion feedthroughs. No literature is found yet on magnetic fluid seals for linear feedthrough, obviously this would give complications for holding the fluid in its place. Since seal doesn't have a solid connection between the shaft and

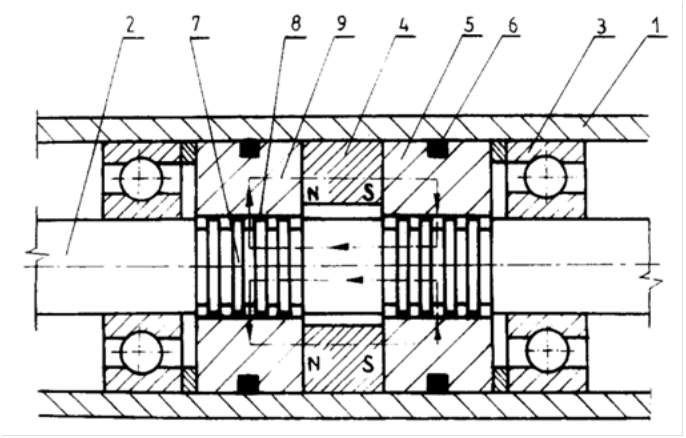

Figure A.5: Schematic view of magnetic fluid feedthrough (source: [34])

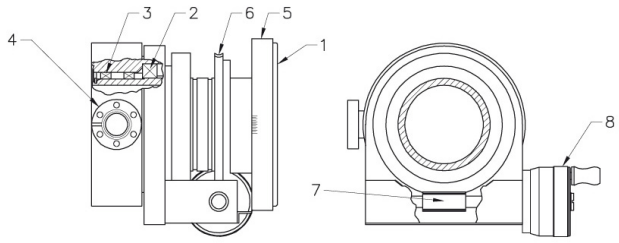

Figure A.6: Schematic view of differentially pumped feedthrough (source: [8])

the housing, there is almost no wear, granting a long lifetime and low power consumption and allowing high rotational speeds. Usually the seal consists of multiple rings, each of which handles a part of the pressure difference. According to [34], magnetic fluid seals are able to seal vacuums in the order of 10^{-8} mbar at rotational speeds of more than 30 000 rpm.

More considerations on the design of magnetic fluid sealed feedthroughs is found in [35]. A company providing magnetic fluid feedthroughs with lots of different characteristics is Telemark [36]. This company also speaks of vacuum sealing up to about 10^{-9} mbar.

Differentially pumped feedthrough A schematic view of this kind of feedthrough is seen in figure A.6. The shaft is supported in the housing with normal bearings (2) and the opening is sealed with at least two standard seals, for example 'U-seals' (3). The air leaking through the seals is pumped away at (4). VG Scienta has feedthroughs that can be pumped to 10^{-2} mbar in the space between the two seals. The total sealing capacity is of course determined by both the pumping action and the quality of the U-seals. Sealing capacity can be increased by adding more 'stages' of rings and pumps.

The power consumption of this type of feedthrough is quite high, due to the friction in the seals and the continuous pumping. Important parameters as lifetime and friction are mostly determined by the U-seals.

A.5 Transmission elements

If a rotating electric motor will be used for actuation, a rotary to linear transmission is needed to translate the motion of the motor to a linear displacement of the stage. In [37] a comparison is made between rotary motor driven stages and linear motor driven stages, for high-precision linear positioning.

A.5.1 Lead screws

A lead screw consists of a rotating threaded shaft with a non rotating nut that makes linear movement when the screw is rotated. In the most simple case, the nut just slides over the screw. In general, lead screws have the following drawbacks [37]:

- transmission errors due to pitch tolerances of the lead screw ('recoil')
- dead zone and friction induced backlash
- limited stiffness
- additional large inertia
- position, velocity and acceleration limitations due to the mechanical characteristics of the lead screw (stiffness, critical velocity)
- wear

Several variants of lead screws exist:

- Ball screws: the surface of the screw and nut are not directly sliding against each other but rolling via balls, similar to a normal ball bearing.
- Hydrostatic or aerostatic lead screws: in this cases a liquid or air film prevents contact between the screw and nut, so that friction is almost entirely eliminated, almost no backlash and recoil exists and the motion is very smooth and vibrationless.

A.5.2 Ball screws

With ball screws, the surface of the screw and nut are not directly sliding against each other but rolling via balls, similar to a normal ball bearing. Ball screws suffer from the drawbacks listed above. In general a trade-off should be made between recoil and friction: eliminating recoil means pushing the nut tightly against the screw so that friction is increased.

NSK [9] is one of the biggest companies that produce ball screws. An indication of the performance of ball screws is found by studying the ball screw catalog of NSK.

Accuracy Accuracy is specified according to standards, in terms of:

- e_p, the maximum difference between the specified travel and actual travel after one full-stroke travel
- v_u, two times the maximum deviation from the 'mean travel path'

For the highest quality standard and a length between 300 and 400 mm, $e_p = 5$ μm and $v_u = 3.5$ μm. This is within the accuracy requirement (10 μm) for the longstroke stage, but it leaves not much budget for other elements in the kinematic chain.

Vibrations A problem with ball screws is noise and vibrations. No estimation of vibrations in ball screws are found but NSK gives data about noise production measured with a microphone at a certain distance from the ball screw. Versteyhe ([38], pp. 5) states that ball screws in general are not able for precision applications because of the vibrations. No quantitative indication of vibrations in ball screws is found.

Maximum speed Rotational speed is limited by the mechanical resonance frequency. For our case this is no problem: with an unsupported length of 400 mm, even the smallest diameter screw can rotate with up to 4000 rpm with simple support on both sides and even more with more extensive support.

Lifetime

The lifetime of ball screws is strongly dependent on the load. Since the load in our case (15 N for 0.3 m/s^2 acceleration of 15 kg) is far less than what ball screws are designed to handle, in theory the lifetime is extremely high.

A.5.3 Rack and pinion

Rack and pinions provide lower transmission ratio than screws, so either a low-speed high-torque motor is needed or extra gearing has to be built in.

The pitch error for racks is specified according to the same standards as screws: the highest accuracy standard has a maximum pitch error of 5 μm for 300 mm length. Typical system accuracy for the rack and pinion combination is about 15 μm. Extreme accurate rack-and-pinion systems are made by Wittenstein [39] with an overall accuracy in the order of 5 μm.

Resolution of course depends on the used encoder and actuator; a complete rack and stepper motor assembly is provided that reaches 300 mm/s linear velocity and a resolution of 3.3 μm is reached when 'microstepping' is enabled.

Source: [40].

A.5.4 Belt and pulley

No examples are found of belt-and-pulley systems used for high-precision applications.

A.5.5 Friction wheels

Friction wheels generate very smooth motion and are very accurate. However the stiffness and force characteristics are very limited ([38], pp. 5). Besides, friction causes wear and particle generation contaminating the vacuum equipment.

A.5.6 Transmissions in vacuum

In general, since each of the transmission mechanisms is based on surfaces sliding or rolling over each other, wear on the contact surfaces makes it unsuitable for vacuum environment. No examples are found in literature and manufacturer's websites of simple lead screws and rack-and-pinions used in vacuum environments.

NSK provides ball screws with a special silver coating that works as a solid lubricant, making them suitable to use in high vacuum (especially semiconductor) applications. The lifetime of these screws however is limited by the silver coating peeling off the surface. Testing is done with these ball screws in vacuum under the following circumstances:

- Pressure: 1.3 - 0.13 x10^{-5} Pa (˜ x10^{-7} mbar)
- Rotational speed: 300 rpm

The screw has the following properties:

- Diameter: 12 mm
- Lead: 4 mm
- Nut preload: 29.4 N

As a result, the lifetime of the bearings was found: about 1x10^7 revolutions. Assuming our stage moves 6 meters for one wafer, with a lead of 4 mm it needs 1500 revolutions per wafer. This means the lifetime of the ball screw spans 6,700 wafers or 670 hours of operation. This is by far less than the requirement. Besides, the linear velocity in this test case was 20 mm/s, a factor 10 too low.

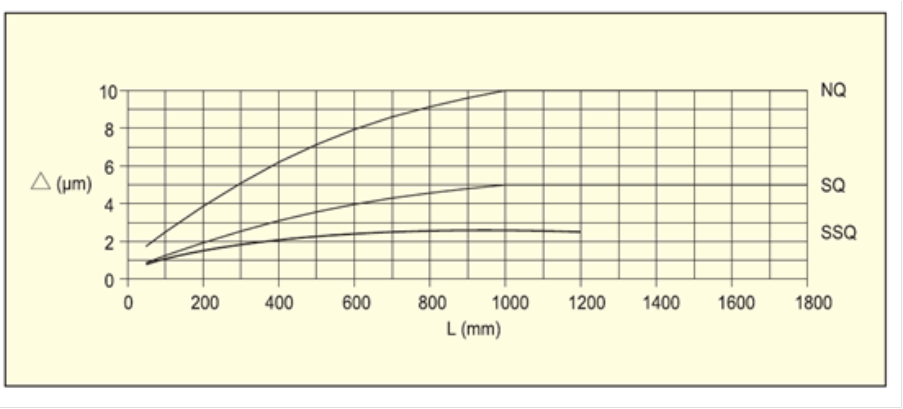

Figure A.7: Relative tolerance for parallelism as function of stage length for three quality classes of Schneeberger linear bearings (source: [41])

To avoid this problem of limited lifetime, a high pitch screw could be used. However, the high pitch either requires extra down gearing or makes the requirement for rotational resolution and accuracy of the motor very strict.

Hydrostatic or aerostatic lead screws don't suffer from wear and friction, but are not suitable for in vacuum because of leakage of the fluid.

A.6 Linear guidings in vacuum environment

A big company providing high-precision linear bearings and guiding stages is Schneeberger [41]. For vacuum applications, special coated roller bearings are provided that have a lifetime of 50 million revolutions.

The Schneeberger stages are available in different accuracy classes. Tolerances on the distance between the stationary and moving element in the directions perpendicular to the direction of motion are about 5μm for the highest class. The maximum difference between two carriage on one rail is 3 μm and on two different rails 5 μm if matched.

For linear bearings, the relative tolerance value (Δ) for the parallelism of the running surfaces is shown in figure A.7 for three quality classes. As seen, for a stage length of about 400 mm even the normal quality (NQ) stages are within 10 μm.

A.7 Errors and vibrations in high precision positioning systems in vacuum

Errors in the position of a high-precision positioning system could be divided in two categories:

- Static errors and vibrations in the non-actuation directions (directions that are not a degree of freedom of the system)
- Position errors in the actuation directions

In the case of a 2-DOF X-Y stage, the non-actuation directions are Z, RX, RY and RZ.

A.7.1 Errors in non-actuation direction

Position errors in the non-actuation directions consist of:

- Static:

  - Tolerances in dimensions of guiding and stage and in the placement of the stage to the environment

- Dynamic:

  - Vibrations of the environment transferred to the stage
  - Vibrations due to non-smoothness of guiding elements
  - Elastic deformation due to inertia forces or external forces on stage.

Usually, the first are not a problem because the stage will be mounted using adjustable elements so that static errors can be eliminated within certain boundary.

Dynamic errors are to be reduced as much as possible by isolating vibrations from the surroundings as much as possible, using high-precision stages and design the mechanism as stiff as possible.

When a short-stroke stage is located on top of the long-stroke positioning stage, the errors can be compensated if these errors are included in the measurement system, dependent on the stroke and control bandwidth of the short-stroke stage.

A.7.2 Errors in actuation direction

According to [7], all positioning errors are as listed in table A.2.

Positioning errors in a closed-loop controlled system can be divided in the following components:

- δ_B: the master control action error. This error has nothing to do with the mechanical system.
- δ_H: the error of initial action or dither signal. This is a dynamic error, caused by a sudden change in the input position or velocity signal or the external force. This error therefore is not present during stationary or constant-speed positioning. When taking a step to a certain position, the system needs some time ('settling time') before these errors are eliminated.
- δ_{CT}: the static control error, consisting of:

  - δ_C: hysteresis error due to static friction forces. When in a stationary position, the actuation force F_a has to overcome the static friction force F_f before the stage comes in motion. Therefore the error $\delta_c = \frac{F_f}{K}$, where K is the static gain of the controller and actuator. This error only occurs only at stationary positioning.
  - δ_L: error caused by backlash. This is caused by a gap in the kinematic chain, a 'dead stroke' in which the movement of the actuator doesn't cause a movement observable by the sensor, or vice versa. This is only a problem when the force in this kinematic chain switches direction, for example when the system starts accelerating/decelerating or when the external forces on the stage change.
  - δ_I: error caused by errors in measurement system and electronics. Errors in the measurement system cause the measured position to be different from the actual distance. The electronics can provide an error if there is an offset between the input (measurement value) and output that goes to the controller.

In a loop-controlled system working at stable outward parameters, δ_C and δ_I are the only error sources for stationary positioning and δ_I the only one for constant-speed positioning.

It is however possible that part of the kinematic chain is not included in the control loop. This is for instance the case when the internal encoder of the actuator is used for position measurement. There may be a kinematic chain between the motor and stage, consisting of for example gears, spindles, guidings, vacuum sealing elements, each of which may cause errors between the actual position of the stage and the position predicted by the measured value. The following errors will show up:

- A static error due to mechanical intolerances in the kinematic chain. This can be eliminated by calibration.

The summarized error components			
Control system type	Title		Error component name
	Total	correct	
Open control system	κ	1	Kinematic error as result of drive manufacturing
		2	Kinematic error as result of drive wear
	L	3	Dead centre of kinematic elements
		4	Dead centre as result of wear
	c	5	Elastic error as result of a load
		6	Elastic error as result of friction force and atmosphere pressure
		7	Elastic error as result of friction force at movement
		8	Elastic error as result of friction force variation
		9	Elastic error as result of non linear elastic forces
		10	Error of occasion kinematic component
	L	11	Error of occasion dead stroke
	c	12	Error of occasion rigidity
		13	Error of occasion friction force.
		14	Error of variated friction forces
Loop controlled system	B		Error of calculated action
	H		Error of initial action
	C		Error of static resistant force
	L 3		Error of dead stroke
	I		Instrumental error

Table A.2: List of errors in high-precision positioning systems (source: [7])

- A static error in calculation of the stage position as function of the measured position. This can also be eliminated by calibration.
- An error due to a backlash in the kinematic chain.
- An error due to elastic deformation caused by external load, friction forces or inertia forces.

A.8 Magnetic fields

In electron lithography, absolutely no magnetic fields can exist at the electron optics module: in the Mapper Lithography machine the allowed magnetic field is in the order of nano-Tesla's. Therefore, for the Wafer Positioning system it is best to use drives that generate magnetic fields as less as possible. Still, shielding may be needed if the wafer positioning system generates fields that are too high to be allowable. Magnetic field shielding can be done in 2 ways:

- Passively, by applying a shield consisting of a layer of μ-metal or other high-magnetic-permeability material.
- Actively, by generating counteracting magnetic fields using coils.

In this chapter first the magnetic field production of several elements is studied and after that the two types of magnetic shielding.

A.8.1 Magnetic field production of typical elements

Wires For a single wire carrying a current, the flux density at distance r from the wire is given by:

$$B = \frac{\mu_0 i}{2\pi r} \tag{A.1}$$

Here μ_0 is the magnetic permeability of the surrounding environment (vacuum or air assumed) and i is the current in the wires.

When two parallel wires with equal but opposite current run close to each other, as usually is the case for a wire that is used for providing electrical power to a device, the magnetic fields of the two wires interact such that the net resulting field is reduced. In [42], for two parallel wires containing an equal but opposite current, the magnitude of the flux density at a distance r from the axis halfway in between the wires are calculated:

$$B_r = \frac{\mu_0 i a}{\pi\left(r^2 + a^2\right)} \tag{A.2}$$

$$B_\theta = \frac{\mu_0 i a}{\pi\left(r^2 - a^2\right)} \tag{A.3}$$

Here a is half of the distance between the two wires.

Here the θ-direction is perpendicular to the direction of the currents and in line with the two wires, and the r -direction perpendicular to both the current direction and the θ-direction. For $r>>a$, this results in:

$$B = \frac{\mu_0 i a}{\pi r^2} \tag{A.4}$$

In figure A.8, the field density is plotted as function of the distance from the wires, for a parallel pair of wires containing a 1mA current and with a distance of 1, 2 and 3 mm from each other.

To further reduce the magnetic fields, wires are usually twisted. When the length of one 'twist' is big enough, it will be approximately the same as for parallel wires but when the twist length is smaller, much better results can be seen. According to [42], the flux density from a twisted pair can be 50 dB below that from a parallel pair of lines, for a certain distance from the wires and a and i the same for both cases.

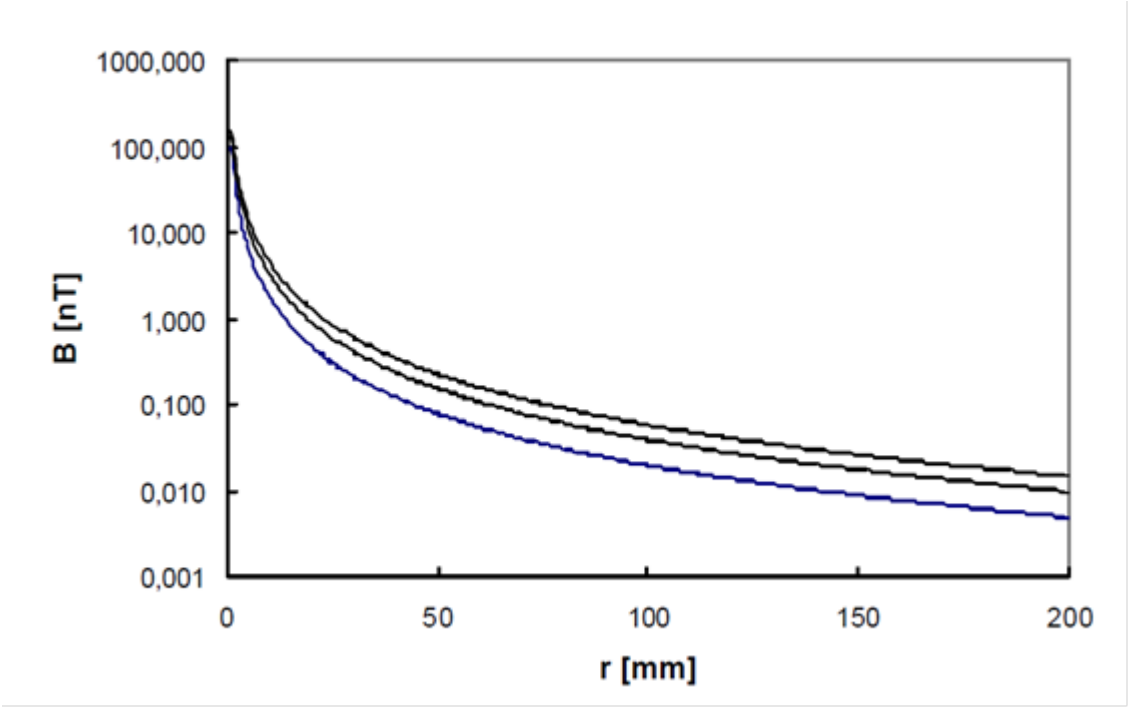

Figure A.8: Magnetic field density as function of distance to wires for parallel pair of wires resp. (from top to bottom) 3, 2 and 1 mm from each other, carrying a current of 1mA DC

When a double pair of wires is used to feed a current to a certain electrical device, the current at a certain location in the two wires is only equal and opposite if:

$$d << \lambda$$

where d is two times the distance along the wires from the observed point to the device (or: the length of the 'path' of the current between the two times it crosses the observed point) and λ the wavelength of the AC current in the wires. When this is not the case, there is too much phase difference between the two wires and therefore the currents would not be exactly equal in magnitude. Since electrons flow through a copper wire at nearly the speed of light this is only a problem at very high-frequency currents or very long wires; for instance the wavelength of a 1MHz AC current is still in the order of a few hundred meters.

Electric motors Electric motors always contain permanent magnets and electromagnets (coils) to generate motion. The permanent magnets used in electric motors usually have field density in the order of 1 Tesla. Usually the magnets are connected such that there is a closed magnetic circuit inside the motor, but still there are some stray fields outside the motor housing. The amount of stray flux outside the motor strongly depends on the design of the motor, but no literature has been found that provides indications on what magnetic field strength to expect for different electric motors.

Piezoelectric drives No literature is found specifically on magnetic fields around piezo elements or drives. In applications where magnetic fields are undesirable, piezoelectric drives are usually used. For example in [43] piezoelectric drives are used for a memory disk test system because they don't generate magnetic fields. Nanomotion [6] produces piezoelectric drives that are claimed to produce no magnetic fields and contain no magnetic materials.

However the electric current through the piezo actuators inevitably produces magnetic fields. As an example, the Nanomotion HR8 is observed. The maximum current for this motor is 600 mA. This is AC

current at about 40 kHz so equation A.4 is valid. For a distance of 1 mm between the wires, the field strength is approximately 1 nT at a distance of 350mm for parallel wires and possibly lower for twisted wires.

At the piezo actuator itself however, the magnetic fields are probably bigger. If a single piezo element is assumed to act as a single piece of wire carrying a current, the magnetic fields can be estimated by equation A.1. When several piezo elements are used, they can be oriented such that the magnetic field cancels out as much as possible.

A.8.2 Passive magnetic shielding

Magnetic shielding is based on re-directing magnetic flux lines by creating a low-resistance path around the volume that should be isolated from the magnetic field. To do that, the volume is surrounded by a closed wall of high-permeability material, for example μ-metal. This is a iron-nickel-molybdenum alloy with extremely high magnetic permeability: up to $\mu = 200,000$ for AC and DC magnetic fields. The magnetic permeability of this material is not constant but dependent on:

- The strength of the magnetic field.
- The thickness of the material.
- The AC frequency of the magnetic field.

Rough estimations of the performance of μ-metal magnetic shields can be found by using simple formulae, but for more accurate estimations finite element analysis has to be done.

Basic formula for perfect single- or double-layered μ-metal shields Several basic formulas exist for the shielding factor S of a single- or double layered μ-metal shield for different basic 2D and 3D shapes [44, 45]. The shielding factor S is defined as H_{out}/H_{in}, the ratio between the magnetic field strength outside the shielding and inside the shielding. For a cubic volume shielded by a single layer of μ-metal at all sides under influence of a DC magnetic field, the shielding factor is given by:

$$S = \frac{4\mu d}{5r} \tag{A.5}$$

With:

- μ the relative magnetic permeability of the μ-metal;
- d the thickness of the material;
- r the side length of the cube.

A double shielded cubic form provides excellent performance:

$$S = S_1 S_2 \left(1 - \frac{r_1^2}{r_2^2}\right) + S_1 + S_2 + 1 \tag{A.6}$$

With:

- S the total shielding performance of the double shield;
- S_1, S_2 the shielding performance of the individual shields, respectively the inner and outer shield;
- r_1, r_2 diameters of the two shields.

When the magnetic field source is inside the shield, the formulae are the same, but S is defined the other way around then.

In thin-walled shields in strong magnetic fields, the saturation limit of the material should be taken into account. In a 2-D closed structure, assuming the permeability to be infinite so all magnetic flux goes through the walls, the 'caught' flux is divided over two paths:

$$B_{walls} = \frac{\Phi_{in}}{2d} \tag{A.7}$$

For a cylindrical structure, the caught flow is typically 2 times the outside area of the cylinder seen from the direction of the magnetic field, so in that case:

$$B_{walls} = \frac{r}{d} B_{in} \tag{A.8}$$

For alternating magnetic fields, the eddy current effect positively influences the shield factor. More complicated formulae for the shielding factor at alternating fields are given in [45]. The critical factor is the ratio between the wall thickness d and penetration depth δ defined as:

$$\delta = \sqrt{\frac{10^7 \rho}{4\pi^2 \mu f}} \tag{A.9}$$

with ρ the specific resistance of the material and f the frequency of the alternating magnetic field. A low frequency obviously leads to a deep penetration. When the penetration is large compared to the wall thickness, this situation corresponds with a DC magnetic field. At higher frequencies, saturation effects will occur due to the small penetration depth, leading to a decreased shield factor. Hence the shield factor as function of frequency has an optimum somewhere.

Influence of holes in the shielding Studies on the effect of openings in a shielding wall are mainly concentrating on open-ended cylindrical shields. According to [45], the strength of a DC field entering the open end of a cylinder decays exponentially with the depth inside the cylinder:

$$H_{op} = H_{out} e^{-kx/R_i} \tag{A.10}$$

where H_{out} is the field strength outside the shielding, x is the distance from the opening along the cylinder axis, R_i is the inner radius of the cylinder and k a factor depending on the direction of the external field: $k = 3.832$ for transverse fields and $k = 2.405$ for longitudinal fields. Now the shield factor due to the opening is defined as:

$$S_{op} = \frac{H_{out}}{H_{op}} = e^{kx/R_i} \tag{A.11}$$

The total field strength at a certain location are found now by adding the fields caused by one or more openings to the 'normal' value as calculated in the previous paragraph:

$$H_{in} = \left(\frac{1}{S} + \frac{1}{S_{op}} \right) H_{out} = \frac{H_{out}}{S_{eff}} \tag{A.12}$$

For AC fields, Mager states in [45] that the phase difference of the fields entering via the two different ways (the 'normal' way and the opening) should be taken into account. At a location where the fields are in phase, the effective shielding factor is just as before:

$$\frac{1}{S_{eff}} = \frac{1}{S} + \frac{1}{S_{op}} \tag{A.13}$$

However, if the fields are 180 degrees out of phase, the effective shielding factor is given by:

$$\frac{1}{S_{eff}} = \frac{1}{S} - \frac{1}{S_{op}} \tag{A.14}$$

Designers could use this to increase the effective shielding factor at a certain spot if confronted with a stationary AC magnetic field with constant frequency.

More information on the effect of open endings of cylindrical shields is found in [45, 46, 47].

At Mapper, the influence of small holes in large volume shields is investigated by doing finite element simulations with a DC magnetic field. A large rectangular box-shaped double-layered μ-metal shield with dimensions of about 1 x 1 x 1.5 m is observed with 4 circular holes of 200 mm diameter with tubes connected to the holes at the outside. The effective shielding factor is decreased in respect to the shield without the holes. Regarding the tubes, the following observations were done:

- The tubes provide magnetic shielding for the opening, increasing the performance with respect to openings without tubes. However, the length of the tubes has limited influence, because the increased shielding provided by long tubes to the opening is counteracted by the fact that the tube also works as an 'antenna' that attracts magnetic fields. At the optimum length, the effective shielding factor of the total system, taken at the center of the box-shape, was decreased to about 16% of the value for the box without holes.
- Making the tubes double-walled has negligible influence, because the magnetic field just 'neglects' the outer shield.
- Connecting the tubes only to the outer shielding layer instead of both the outer and inner layer leads to an increase of the effective shielding factor, because then the flux attracted by the tubes will mainly stay in the outer wall. Now the optimum shielding factor was about 27% of the original value.

The influence of using a metal grid (a 'french fries cutter') instead of a tube is observed. For same length-diameter ratio the performance of these two is approximately the same. However, using a grid it is possible to provide a double-layered shielding for the opening, which was impossible with tubes. When a grid is used to magnetically seal the opening both for the inner as for the outer shielding layer, the total effective shielding factor is brought back to 35% of the initial value. Of course a grid in the opening is only possible when no solid elements have to go through the opening; in the observed case the openings were used for pumping of a vacuum tank.

These observations are merely based on finite element simulations of one particular situation, so no general laws can be extracted from this.

A.8.3 Active magnetic shielding

Instead of shielding a magnetic field passively, it can be compensated by generating an electromagnetic field opposite to the original field using a set of coils, usually in the 'Helmholtz configuration'. The advantage of this is the possibility of active compensation: for magnetic fields of which the behavior is known (magnetic fields generated by permanent magnets or electronics with predictable behavior) it is easy to provide compensation, and for fields caused by an unpredictable source, a probe could be used to measure the field close to the coil and control the coil actively.

In practice, compensating magnetic fields has many complications and limitations:

- Only DC or low-frequency AC fields can be handled, because the high inductance of the coils.
- A complicated control system is needed, especially when multiple volumes next to each other have to be shielded separately.
- The coils need more space than passive shielding layers.

Literature can be found on actively shielding volumes against magnetic fields. In [48], a large volume is shielded against a 60 Hz AC magnetic field with multiple coils around the volume. When the field inside the volume is observed for different points, the average remaining magnetic field was still 5 - 25 % of the outside field strength. However, the following things should be observed:

- The aim was to provide shielding for the entire volume. When focusing on one spot, the current in the coils can be controlled such that the shielding factor is optimal for that spot.
- No active feedback was applied.

No literature has been found on using coils to shield the 'outside' of a volume against magnetic fields produced at the 'inside'.

Appendix B

Duty cycle calculation regarding overheating

Nanomotion specifies an EOP (Envelope of Performance) for their HRx motors: the duty cycle and max continuous operating time for different environments and working conditions. See figure B.1. To investigate whether the expected duty cycle of the WPS is allowed by this restrictions, a calculation example is done, in complete analogy to a calculation example found in a Nanomotion technical document.

For a single wafer, the X-stage makes 20 exposure runs of 300 mm at 75 mm/s (required), 20 return runs at 200 mm/s. Accelerating and decelerating is done at 0.3 m/s^2, which means 22.5 N acceleration/deceleration force. Friction force in the stage is assumed to be 4N constant (based on specifications of common linear guidings).

A single Nanomotion HR8 motor can deliver 30 N static stall force and 10 N at 200 mm/s, so a single HR8 would in theory already be enough. The different cycles are now as follows:

- Constant speed exposure runs: v = 75 mm/s, F = 4 N, duration = 20 times 4 s = 80 s. This is curve 'b'.
- Acceleration exposure runs: v = 0-30 mm/s, F = 26.5 N, duration = 20 times 0.25 s = 5 s. This is curve 'f'.
- Deceleration exposure runs: no effort due to inherent passive break.
- Constant speed extra runs: v = 200 mm/s, F = 4 N, duration = 20 times 1.5 s = 30 s. This is curve 'e'.
- Acceleration extra runs: v = 0-200 mm/s, F = 26.5 N, duration = 20 times 0.67 s = 13.3 s. Obviously the acceleration cannot be constant, but this heavy duty is considered as curve 'g'.
- Deceleration extra runs: no effort due to inherent passive break.

The motor is working for 128.3 seconds in total now. The effective maximum duty cycle is the average of the individual stages, weighed according to the duration:

$$DC_{eff} = \frac{80DC_b + 5DC_f + 30DC_e + 13.3DC_g}{128.3} = \frac{80 \cdot 44\% + 5 \cdot 9\% + 30 \cdot 13\% + 13.3 \cdot 8\%}{128.3} = 32\%$$

This means the total time needed for a wafer to prevent the X-drives from overheating is $\frac{128.3}{0.32} = 405$ seconds. This is 6 minutes and 45 seconds while the available time is 6 minutes to reach the 10 WPH throughput. This means the estimated duty cycle is not within the Nanomotion specifications. However, the following things should be regarded:

- The assumed duty cycle is only an estimation. On one hand, extra runs are necessary for for instance calibration and wafer loading while on the other hand not all exposure and return runs will require a full-stroke travel because of the circular shape of the wafer.

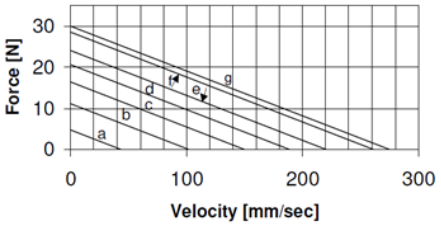

Curve	25° C		50° C		Vacuum 25° C	
	Duty Cycle	max.continuous operation time	Duty Cycle	max.continuous operation time	Duty Cycle	max.continuous operation time
a	100%	-	100%	-	100%	-
b	100%	-	100%	-	44%	184
c	100%	-	92%	137	26%	107
d	100%	-	62%	93	17%	72
e	78%	87 seconds	47%	70	13%	55
f	56%	62 seconds	33%	50	9%	39
g	50%	56 seconds	30%	45	8%	35

Figure B.1: Envelope of Performance for the Nanomotion HR8 motor

- Probably more than one motor will be used to increase actuation stiffness, so that the delivered force per motor is lower than in the calculation example.
- The Nanomotion EOP is only a rough guideline.

Still, the calculation example shows that the required duty will at least be not very far from the maximum allowed duty, so overheating is a problem that should be seriously taken into account.

Appendix C

Dimensions and material properties for the simulation model

C.1 Dimensions

The symbols used for the dimensions of the modeled body are shown in Figure C.1. The values are as follows:

- Dimensions of the piezoelectric body ($l \times w \times t$): $30 \times 7.5 \times 3$ mm.
- Dimensions of the finger ($l_f \times w_f$): 4.2×3.0 mm.
- Dimensions of the electrodes ($l_e \times w_e$): 14.0×3.0 mm.
- Distance of support points to front and back surfaces: $dy_{p1} = 4.8$ mm; $dy_{p2} = 4.3$ mm.
- Distance of the electrodes from the side surfaces: $dx_e = 0.4$ mm; $dy_{e1} = 0.5$ mm; $dy_{e2} = 0.5$ mm.

All these dimensions were measured on a single real motor using a caliper with an approximate accuracy of ± 0.1 mm. In the simulation model, the electrodes are drawn up until the side surfaces of the body (dx_e, dy_{e1} and dy_{e2} all zero) and since a 2D plane stress model with a constant thickness is used, the finger is box-shaped instead of cylindrical.

C.2 Material properties

C.2.1 Piezo-body material

Properties used in the simulation model for the material of which the piezo-body consists:

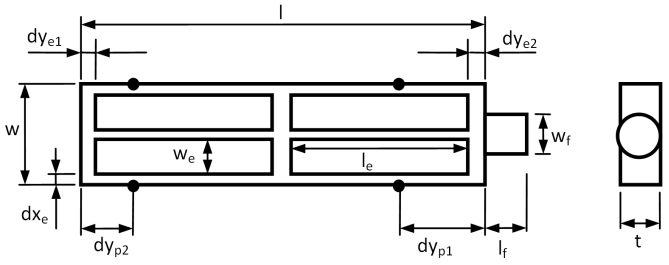

Figure C.1: Dimensions of the modeled geometry.

$$[c_E] = \begin{bmatrix} 1.29 & 0.702 & 0.679 & 0 & 0 & 0 \\ 0.702 & 1.29 & 0.679 & 0 & 0 & 0 \\ 0.679 & 0.679 & 1.16 & 0 & 0 & 0 \\ 0 & 0 & 0 & 0.256 & 0 & 0 \\ 0 & 0 & 0 & 0 & 0.256 & 0 \\ 0 & 0 & 0 & 0 & 0 & 0.306 \end{bmatrix} \cdot 10^{11} \text{ Pa}$$

$$[e] = \begin{bmatrix} 0 & 0 & 0 & 0 & 6.79 & 0 \\ 0 & 0 & 0 & 6.79 & 0 & 0 \\ -6.27 & -6.27 & 16.0 & 0 & 0 & 0 \end{bmatrix} \text{ C/m}^2$$

$$[\varepsilon_S] = \begin{bmatrix} 1.35 & 0 & 0 \\ 0 & 1.35 & 0 \\ 0 & 0 & 0.941 \end{bmatrix} \cdot 10^3 \varepsilon_0$$

$$\rho = 7800 \text{ kg/m}^3$$

$$\alpha = 0$$

$$\beta = 2.0 \cdot 10^{-8} \text{ s}$$

$$\tan\delta = 5 \cdot 10^{-3}$$

Here $[c_E]$ is the elasticity matrix at constant electric field, $[e]$ the piezoelectric coupling matrix, $[\varepsilon_S]$ the permittivity matrix at constant strain, ρ the density and α and β the Rayleigh-constants for material damping.

The properties of the real material used in the Nanomotion motor are not known, so the values are assumptions based on properties of the material 'pic241' in the documentation of PI ceramics [11], the material 'pzt4' in the COMSOL material library and a paper on material damping in piezoelectric materials [28].

C.2.2 Finger material

Properties used in the simulation model for the isotropic material Al_2O_3 of which the finger consists:

$$E = 300 \text{ GPa}$$

$$\nu = 0.21$$

$$\rho = 3690 \text{ kg/m}^3$$

$$\mu = 0.36$$

Here E is the Young's modulus, ν is the Poisson's ratio, ρ is the density and μ the friction coefficient between the finger and drive strip.

Appendix D

Detailed model description

D.1 Notation

Throughout this appendix, matrices are denoted as $[X]$, and $n \times 1$ vectors as $\mathbf{x}$. A $[0]$ means a matrix of zeros and a $\mathbf{0}$ a vector of zeros. Matrices and vectors can contain subscripts. If p and q are both an integer or array of integers:

- $[X_{pq}]$ stands for the matrix containing the elements X_{PQ} for all P in the array of indices p and all Q in the array of indices q, so if $p = \{1, 2\}$ and $q = \{3, 4\}$, $[X_{pq}] = \begin{bmatrix} X_{13} & X_{14} \\ X_{23} & X_{24} \end{bmatrix}$.
- $[X_p]$ contains the rows of X corresponding to the indices in p.
- $\mathbf{x}_p$ denotes the vector containing the elements x_P for all P in the array of indices p.

D.2 Unconstrained equations of motion

D.2.1 Fundamental structural and piezoelectric equations

The general equations for piezoelectric material are given by:

$$\mathbf{T} = [c_E]\,\mathbf{S} + [e]^T\,\mathbf{E} \tag{D.1}$$

$$\mathbf{D} = [e]\,\mathbf{S} + [\varepsilon_S]\,\mathbf{E} \tag{D.2}$$

The second describes the direct piezoelectric effect (generating an electrostatic field by deforming the crystal) whereas the first describes the converse piezoelectric effect (deforming the crystal by applying an electrostatic field). Here $\mathbf{T}$ is the 6×1 tensor of stresses, $\mathbf{S}$ the 6×1 tensor of strains, $\mathbf{E}$ the 3×1 vector of electrical fields, $\mathbf{D}$ the 3×1 vector of electric charge displacements and $[e]$, $[c_E]$ and $[\varepsilon_S]$ the matrices of material properties.

Equations D.1 are written as:

$$\begin{bmatrix} \sigma_x \\ \sigma_y \\ \sigma_z \\ \tau_{zy} \\ \tau_{zx} \\ \tau_{xy} \end{bmatrix} = \begin{bmatrix} c_{11}^E & c_{12}^E & c_{13}^E & 0 & 0 & 0 \\ c_{21}^E & c_{22}^E & c_{23}^E & 0 & 0 & 0 \\ c_{31}^E & c_{32}^E & c_{33}^E & 0 & 0 & 0 \\ 0 & 0 & 0 & c_{44}^E & 0 & 0 \\ 0 & 0 & 0 & 0 & c_{55}^E & 0 \\ 0 & 0 & 0 & 0 & 0 & c_{66}^E \end{bmatrix} \begin{bmatrix} e_x \\ e_y \\ e_z \\ \gamma_{zy} \\ \gamma_{zx} \\ \gamma_{xy} \end{bmatrix} + \begin{bmatrix} 0 & 0 & e_{31} \\ 0 & 0 & e_{32} \\ 0 & 0 & e_{33} \\ 0 & e_{24} & 0 \\ e_{15} & 0 & 0 \\ 0 & 0 & 0 \end{bmatrix} \begin{bmatrix} E_x \\ E_y \\ E_z \end{bmatrix} \tag{D.3}$$

In the 2D plane stress model, the out-of-plane stresses σ_z, τ_{zy} and τ_{zx} are zero, and the out-of-plane bending γ_{zy} and γ_{zx} are not included so that E_x and E_y also don't play a role. Rewriting leads to:

$$\begin{bmatrix} \sigma_x \\ \sigma_y \\ \tau_{xy} \end{bmatrix} = \begin{bmatrix} c_{11}^E - \frac{c_{13}^E c_{31}^E}{c_{33}^E} & c_{12}^E - \frac{c_{13}^E c_{32}^E}{c_{33}^E} & 0 \\ c_{21}^E - \frac{c_{23}^E c_{31}^E}{c_{33}^E} & c_{22}^E - \frac{c_{23}^E c_{32}^E}{c_{33}^E} & 0 \\ 0 & 0 & c_{66}^E \end{bmatrix} \begin{bmatrix} e_x \\ e_y \\ \gamma_{xy} \end{bmatrix} + \begin{bmatrix} e_{31} - \frac{c_{13}^E e_{33}}{c_{33}^E} \\ e_{32} - \frac{c_{23}^E e_{33}}{c_{33}^E} \\ 0 \end{bmatrix} E_z \tag{D.4}$$

From now on $\{T\}$ and $\{S\}$ will be used to denote the above 3×1 vectors of in-plane stresses and strains and the above reduced elasticity and piezoelectric coupling matrix will be called respectively $[c']$ and $[e']$:

$$\mathbf{T} = [c']\,\mathbf{S} + [e']\,E_z \tag{D.5}$$

For the ceramic finger material the reduced elasticity matrix is written as [27]:

$$[c'] = \frac{E}{1-\nu^2} \begin{bmatrix} 1 & \nu & 0 \\ \nu & 1 & 0 \\ 0 & 0 & \frac{1-\nu}{2} \end{bmatrix} \tag{D.6}$$

where E is the Young's modulus and ν the Poisson's ratio.

D.2.2 Finite element discretization and equations of motion

Because the model was not built in an existing FEM package, but written in MatLab, this section describes how the equations of motion are obtained, beginning at the basic rules of finite element modeling as described in [27].

For a triangular element in a FEM model, the value of a property ϕ on a location (x, y) somewhere within this element can be expressed in terms of the property values at the three nodes, resp. ϕ_1, ϕ_2 and ϕ_3:

$$\phi(x,y) = N_1(x,y)\phi_1 + N_2(x,y)\phi_2 + N_3(x,y)\phi_3 = [N]\,\{\phi\} \tag{D.7}$$

For linear triangular elements the derivatives of the shape functions are constant throughout the element:

$$\begin{aligned} \left\{\frac{\partial N_1}{\partial x}, \frac{\partial N_2}{\partial x}, \frac{\partial N_3}{\partial x}\right\} &= \frac{1}{2A}\{(y_2 - y_3), (y_3 - y_1), (y_1 - y_2)\} \\ \left\{\frac{\partial N_1}{\partial y}, \frac{\partial N_2}{\partial y}, \frac{\partial N_3}{\partial y}\right\} &= \frac{1}{2A}\{(x_3 - x_2), (x_1 - x_3), (x_2 - x_1)\} \end{aligned} \tag{D.8}$$

Here A is the surface area of the element, given by:

$$A = \frac{1}{2}\begin{vmatrix} 1 & x_1 & y_1 \\ 1 & x_2 & y_2 \\ 1 & x_3 & y_3 \end{vmatrix} \tag{D.9}$$

If Equation D.7 is applied to the property 'displacement', the strain tensor $\mathbf{S}$ at location (x, y) can be found as function of the nodal displacements:

$$\mathbf{S}(x,y) = \begin{bmatrix} e_x \\ e_y \\ \gamma_{xy} \end{bmatrix} = \begin{bmatrix} \frac{\partial u}{\partial x} \\ \frac{\partial v}{\partial y} \\ \frac{\partial u}{\partial y} + \frac{\partial v}{\partial x} \end{bmatrix} = \begin{bmatrix} \frac{\partial N_1}{\partial x} & \frac{\partial N_2}{\partial x} & \frac{\partial N_3}{\partial x} & 0 & 0 & 0 \\ 0 & 0 & 0 & \frac{\partial N_1}{\partial y} & \frac{\partial N_2}{\partial y} & \frac{\partial N_3}{\partial y} \\ \frac{\partial N_1}{\partial y} & \frac{\partial N_2}{\partial y} & \frac{\partial N_3}{\partial y} & \frac{\partial N_1}{\partial x} & \frac{\partial N_2}{\partial x} & \frac{\partial N_3}{\partial x} \end{bmatrix} \begin{bmatrix} u_1 \\ u_2 \\ u_3 \\ v_1 \\ v_2 \\ v_3 \end{bmatrix} \tag{D.10}$$

This is constant throughout the element (independent of x and y), so this can be written as:

$$\mathbf{S}_{(e)} = [B]_{(e)}\,\mathbf{d}_{(e)} \tag{D.11}$$

Here $\mathbf{s}^{(e)}$ is the 3×1 vector of strains in the element (e) and $\mathbf{d}^{(e)}$ the 6×1 vector containing the displacements u and v (resp x- and y-displacement) of the three nodes of the element and $[B]_{(e)}$ the so-called 'strain-displacement' matrix for the element.

The electric field E_z is related to the potential difference P over the geometry in z-direction:

$$E_z(x,y) = \frac{P(x,y)}{t} \tag{D.12}$$

where t is the thickness of the body.

$$E_z(x,y) = \frac{1}{t} \begin{bmatrix} N_1(x,y) & N_2(x,y) & N_3(x,y) \end{bmatrix} \begin{bmatrix} P_1 \\ P_2 \\ P_3 \end{bmatrix} \tag{D.13}$$

$$E_z(x,y) = \frac{1}{t} [N](x,y)\mathbf{P}_{(e)} \tag{D.14}$$

Here $\mathbf{P}_{(e)}$ is contains the values of P on the three nodes of the element (e).

The potential energy $U_{(e)}$ in the element is given by integrating $\mathbf{S}_{(e)}^T \mathbf{T}_{(e)}$ over the volume of the element. Since we use a 2D model, the volume integral is replaced by a surface integral multiplied by the thickness t of the element.

$$U_{(e)} = t \cdot \iint_{S_{(e)}} \mathbf{S}_{(e)}^T \mathbf{T}_{(e)} dS = t \cdot \iint_{S_{(e)}} \mathbf{S}_{(e)}^T \left([c'] \mathbf{S}_{(e)} + [e'] E_z(x,y) \right) dS =$$

$$t \cdot \iint_{S_{(e)}} \left(\mathbf{d}_{(e)}^T [B]_{(e)}^T [c'] [B]_{(e)} \mathbf{d}_{(e)} + \frac{1}{t} \mathbf{d}_{(e)}^T [B]_{(e)}^T [e'] [N]_{(e)} \mathbf{P}_{(e)} \right) dS \tag{D.15}$$

All matrices except $[N]$ are constant over the surface of the element. It can be shown that integration of $[N]$ over the surface leads to the matrix $A \cdot \begin{bmatrix} \frac{1}{3} & \frac{1}{3} & \frac{1}{3} \end{bmatrix}$. Therefore:

$$U_{(e)} = At \left(\mathbf{d}_{(e)}^T [B]_{(e)}^T [c'] [B]_{(e)} \mathbf{d}_{(e)} + \mathbf{d}_{(e)}^T [B]_{(e)}^T [e'] [C] \mathbf{P}_{(e)} \right) \tag{D.16}$$

where $[C] = \frac{1}{t} \begin{bmatrix} \frac{1}{3} & \frac{1}{3} & \frac{1}{3} \end{bmatrix}$.

This is written as:

$$U_{(e)} = \mathbf{d}_{(e)}^T [K]_{(e)} \mathbf{d}_{(e)} + \mathbf{d}_{(e)}^T [S]_{(e)} \mathbf{P}_{(e)} \tag{D.17}$$

The individual expressions for each element is added up, to get the potential energy equation for the total system:

$$U = \mathbf{d}^T [K] \mathbf{d} + \mathbf{d}^T [S] \mathbf{P} \tag{D.18}$$

Deriving the energy to the displacements gives the equations for the static forces:

$$[K] \mathbf{d} + [S] \mathbf{P} = \mathbf{f}_A \tag{D.19}$$

For a system with n nodes, $\{\delta\}$ is now a vector of length $2n$ containing all nodal displacements u and v, $\mathbf{P}$ a vector with length n containing the potential difference at all nodes, $\mathbf{f}_A$ a $2n$ vector containing the applied nodal forces in x and y, $[K]$ by definition the $2n \times 2n$ stiffness matrix and $[S]$ the $2n \times n$ piezoelectric coupling matrix.

By definition, the mass matrix of one element is given by:

$$[M]_{(e)} = t \iint_{S^{(e)}} \begin{bmatrix} [N]^T [N] & [0] \\ [0] & [N]^T [N] \end{bmatrix} \rho dS \tag{D.20}$$

For the integration of the shape functions over the surface of a triangular element it can be shown that:

$$\iint_{S^{(e)}} N_1^a N_2^b N_3^c dS = 2A^{(e)} \frac{a!b!c!}{(a+b+c+2)!} \tag{D.21}$$

Using this rule, the mass matrix for a single element becomes as follows:

$$[M]_{(e)} = \rho A \begin{bmatrix} \frac{1}{6} & \frac{1}{12} & \frac{1}{12} & & & \\ \frac{1}{12} & \frac{1}{6} & \frac{1}{12} & & [0] & \\ \frac{1}{12} & \frac{1}{12} & \frac{1}{6} & & & \\ & & & \frac{1}{6} & \frac{1}{12} & \frac{1}{12} \\ & [0] & & \frac{1}{12} & \frac{1}{6} & \frac{1}{12} \\ & & & \frac{1}{12} & \frac{1}{12} & \frac{1}{6} \end{bmatrix} \tag{D.22}$$

This can be summed up to obtain the total $2n \times 2n$ mass matrix $[M]$.

The damping matrix $[Z]$ is obtained according to the Rayleigh damping model;

$$[Z] = \alpha [M] + \beta [K] \tag{D.23}$$

Finally, the full equations of motion are given by:

$$[M] \ddot{\mathbf{d}} + [Z] \dot{\mathbf{d}} + [K] \mathbf{d} = - [S] \mathbf{P} + \mathbf{f}_A \tag{D.24}$$

D.2.3 Model inputs

In finite element modeling, the potential distribution is solved in the same way as the fundamental stress-strain equations: instead of integrating $\mathbf{S}^T\mathbf{T}$, now $\mathbf{E}^T\mathbf{D}$ is integrated over an element, expressed in terms of the nodal potentials $\mathbf{P}$ so that the derivative of this property to $\mathbf{P}$ should be zero. If this is done using Equation D.2, neglecting the piezoelectric coupling, the following results:

$$\begin{bmatrix} D_x \\ D_y \end{bmatrix} = \begin{bmatrix} \varepsilon_{11} & 0 \\ 0 & \varepsilon_{22} \end{bmatrix} \begin{bmatrix} E_x \\ E_y \end{bmatrix} \tag{D.25}$$

$$\mathbf{D} = [\varepsilon'] \mathbf{E} \tag{D.26}$$

The electric field vector can be expressed in terms of the nodal potentials and the element shape functions:

$$\begin{bmatrix} E_x \\ E_y \end{bmatrix} = \begin{bmatrix} \frac{\partial P}{\partial x} \\ \frac{\partial P}{\partial y} \end{bmatrix} = \begin{bmatrix} \frac{\partial N_1}{\partial x} & \frac{\partial N_2}{\partial x} & \frac{\partial N_3}{\partial x} \\ \frac{\partial N_1}{\partial y} & \frac{\partial N_2}{\partial y} & \frac{\partial N_3}{\partial y} \end{bmatrix} \begin{bmatrix} P_1 \\ P_2 \\ P_3 \end{bmatrix} \tag{D.27}$$

$$\mathbf{E}_{(e)} = [B']_{(e)} \mathbf{P}_{(e)} \tag{D.28}$$

In analogy to before, the property $\mathbf{E}_{(e)}^T \mathbf{D}_{(e)}$ is expressed in the known matrices and integrated over the volume:

$$t \iint_{S_{(e)}} \mathbf{E}_{(e)}^T \mathbf{D}_{(e)} dS = t \iint_{S_{(e)}} \mathbf{P}_{(e)}^T [B']_{(e)}^T [\varepsilon] [B']_{(e)} \mathbf{P}_{(e)} dS =$$

$$At \mathbf{P}_{(e)}^T [B']_{(e)}^T [\varepsilon] [B']_{(e)} \mathbf{P}_{(e)} = At \mathbf{P}_{(e)}^T [T]_{(e)} \mathbf{P}_{(e)} \tag{D.29}$$

Again the individual $[T]_{(e)}$'s can be added to obtain the the full $[T]$ matrix. Then the solution can then be found by making the partial derivatives of the above expression to the potentials zero:

$$[T] \mathbf{P} = \mathbf{0} \tag{D.30}$$

Now if the potential on nodes j is prescribed while the potential on nodes i is free, the full potential distribution vector can be obtained by:

$$[T_{ii}]\,\mathbf{P}_i = -\,[T_{ij}]\,\mathbf{P}_j \tag{D.31}$$

In the simulation model there are only two independent voltage inputs: V_A on electrodes 1 and 4 and V_b on electrodes 2 and 3. Since all relations are linear, the potential distribution therefore can be written as:

$$\mathbf{P} = \mathbf{P}_A V_A + \mathbf{P}_B V_B \tag{D.32}$$

where $\mathbf{P}_A$ is the potential vector if the potential difference is prescribed to 1 V at the nodes on electrodes 1 and 4 and to 0 V at the nodes on electrodes 2 and 3, and $\mathbf{P}_A$ the other way around.

The only applied force is the preload force f_{ps} distributed over the four support nodes. Therefore:

$$\mathbf{f}_A = \mathbf{q} f_{ps} \tag{D.33}$$

where $\mathbf{q}$ is the $2n \times 1$ vector representing the distribution of the preload force over the contact nodes, containing the value $1/4$ on the rows corresponding to the vertical displacements of the support nodes, and zeros elsewhere. The equations of motion are rewritten to:

$$[M]\,\ddot{\mathbf{d}} + [Z]\,\dot{\mathbf{d}} + [K]\,\mathbf{d} = [X]\,\mathbf{u} \tag{D.34}$$

Here $\mathbf{u} = \begin{bmatrix} f_{pl} & V_A & V_B \end{bmatrix}$ is the vector of model inputs and $[X]$ the input coupling matrix:

$$[X] = \begin{bmatrix} \mathbf{q} & -[S]\,\mathbf{P}_A & -[S]\,\mathbf{P}_B \end{bmatrix} \tag{D.35}$$

D.3 Constraints and contact model

To handle with the constraints and contact node, the degrees of freedom (the nodal displacements) are subdivided in four categories:

- j: the degrees of freedom that are constrained by the support structure
- k: the unconstrained degrees of freedom (everything that is not in one of the other categories)
- l: the displacement of the contact node in drive direction
- m: the displacement of the contact node in normal direction

In addition to this, the moving slider has to be added to the model. The slider is represented by a rigid body with mass m_{sl} that is constrained in the normal direction by a linear guiding and therefore has only one degree of freedom: its displacement in the drive direction δ_{sl}.

D.3.1 General equations of motion

In the equations of motion given in Equation D.34, the constrained displacements j and the forces corresponding to this DOFs are eliminated, so that only the degrees of freedom k, l and m remain. The displacements $\mathbf{d}_m$ are also eliminated because they are constrained. There can be applied forces on the unconstrained degrees of freedom k, and in the contact node there is the normal forces f_N and traction force f_D. What remains of the equations then is the following:

$$\begin{bmatrix} [M_{kk}] & [M_{kl}] \\ [M_{lk}] & [M_{ll}] \\ [M_{mk}] & [M_{ml}] \end{bmatrix} \begin{bmatrix} \ddot{\mathbf{d}}_k \\ \ddot{d}_l \end{bmatrix} + \begin{bmatrix} [Z_{kk}] & [Z_{kl}] \\ [Z_{lk}] & [Z_{ll}] \\ [Z_{mk}] & [Z_{ml}] \end{bmatrix} \begin{bmatrix} \dot{\mathbf{d}}_k \\ \dot{d}_l \end{bmatrix} + \begin{bmatrix} [K_{kk}] & [K_{kl}] \\ [K_{lk}] & [K_{ll}] \\ [K_{mk}] & [K_{ml}] \end{bmatrix} \begin{bmatrix} \mathbf{d}_k \\ d_l \end{bmatrix} = \ldots$$

$$\ldots \begin{bmatrix} 0 \\ -f_D \\ -f_N \end{bmatrix} + \begin{bmatrix} [X_k] \\ [X_l] \\ [X_m] \end{bmatrix} \mathbf{u} \tag{D.36}$$

Here the notation is as explained in Section D.1. A single equation should be added to this for the slider displacement d_{sl}:

$$m_{sl}\ddot{d}_{sl} = f_D + f_{sf} \tag{D.37}$$

Here f_{sf} is the friction in the stage guiding. In these equations, $\ddot{\mathbf{d}}_k$, $\ddot{d}_l$, $\ddot{d}_{sl}$, f_D and f_N are the unknowns. If n_k is the number of degrees of freedom k, there are now $n_k + 3$ equations in $n_k + 4$ unknowns. Therefore a condition is still to be added before the model can be solved.

D.3.2 Equations of motion without slider displacement

Slip phase If the contact slips, there is an explicit relation between the normal and tangential contact force. If the situation where $\dot{d}_l > \dot{d}_{sl}$ is called 'positive slip', then in the positive slip state:

$$f_D = \mu f_N \tag{D.38}$$

Now the first right hand term in Equation D.36 can be rewritten:

$$\begin{bmatrix} \mathbf{0} \\ -f_D \\ -f_N \end{bmatrix} = -f_N \begin{bmatrix} \mathbf{0} \\ \mu \\ 1 \end{bmatrix} \tag{D.39}$$

Bringing this to the left hand leads to the full equations:

$$\begin{bmatrix} [M_{kk}] & [M_{kl}] & \mathbf{0} \\ [M_{lk}] & [M_{ll}] & \mu \\ [M_{mk}] & [M_{ml}] & 1 \end{bmatrix} \begin{bmatrix} \ddot{\mathbf{d}}_k \\ \ddot{d}_l \\ f_N \end{bmatrix} + \begin{bmatrix} [Z_{kk}] & [Z_{kl}] \\ [Z_{lk}] & [Z_{ll}] \\ [Z_{mk}] & [Z_{ml}] \end{bmatrix} \begin{bmatrix} \dot{\mathbf{d}}_k \\ \dot{d}_l \end{bmatrix} + \begin{bmatrix} [K_{kk}] & [K_{kl}] \\ [K_{lk}] & [K_{ll}] \\ [K_{mk}] & [K_{ml}] \end{bmatrix} \begin{bmatrix} \mathbf{d}_k \\ d_l \end{bmatrix} = ...$$

$$... \begin{bmatrix} [X_k] \\ [X_l] \\ [X_m] \end{bmatrix} \mathbf{u} \tag{D.40}$$

This is written as:

$$\begin{bmatrix} [M_1] & [M_2] \\ [M_3] & 1 \end{bmatrix} \begin{bmatrix} \ddot{\mathbf{d}} \\ f_N \end{bmatrix} + \begin{bmatrix} [Z_1] \\ [Z_2] \end{bmatrix} \dot{\mathbf{d}} + \begin{bmatrix} [K_1] \\ [K_2] \end{bmatrix} \mathbf{d} = \begin{bmatrix} [X_1] \\ [X_2] \end{bmatrix} \mathbf{u} \tag{D.41}$$

Here $\mathbf{d}$ is the vector of unknown displacements k and l. Algebraic rewriting of these equations leads to:

$$\begin{aligned} \left([M_1] - [M_2]\,[M_3]\right) \ddot{\mathbf{d}} + \left([Z_1] - [M_2]\,[Z_2]\right) \dot{\mathbf{d}} + \left([K_1] - [M_2]\,[K_2]\right) \mathbf{d} &= \left([X_1] - [M_2]\,[X_2]\right) \mathbf{d} \\ \left[M^{slip'}\right] \ddot{\mathbf{d}} + \left[Z^{slip'}\right] \dot{\mathbf{d}} + \left[K^{slip'}\right] \mathbf{d} &= \left[X^{slip'}\right] \mathbf{d} \end{aligned} \tag{D.42}$$

Combining the lower row of Equation D.41 with Equation D.42 leads to:

$$\begin{aligned} f_N = &\left([M_3] \left[M^{slip'}\right]^{-1} \left[Z^{slip'}\right] - [Z_2]\right) \dot{\mathbf{d}} + \left([M_3] \left[M^{slip'}\right]^{-1} \left[K^{slip'}\right] - [K_2]\right) \mathbf{d} + ... \\ &... \left([X_2] - [M_3] \left[M^{slip'}\right]^{-1} \left[X^{slip'}\right]\right) \mathbf{u} = ... \\ &... \left[C_N^{slip'}\right] \begin{bmatrix} \mathbf{d} \\ \dot{\mathbf{d}} \end{bmatrix} + \left[D_N^{slip'}\right] \mathbf{d} \end{aligned} \tag{D.43}$$

The Equations D.42, D.43 and D.38 now provide resp. the constrained equations of motion and the relations for the normal and tangential contact force. With this, the model can be solved.

For 'negative slip' the equations are exactly the same, except the μ-term in the mass matrix becomes negative.

Stick phase In the stick phase, there is no explicit relation between f_D and f_N. Instead, an extra condition is added for the tip displacement:

$$\ddot{d_l} = 0 \tag{D.44}$$

Therefore the Equation D.36 can be rewritten to:

$$\begin{bmatrix} [M_{kk}] & [M_{kl}] & \mathbf{0} & \mathbf{0} \\ [0] & 1 & 0 & 0 \\ [M_{lk}] & [M_{ll}] & 1 & 0 \\ [M_{mk}] & [M_{ml}] & 0 & 1 \end{bmatrix} \begin{bmatrix} \ddot{\mathbf{d}}_k \\ \ddot{d_l} \\ f_D \\ f_N \end{bmatrix} + \begin{bmatrix} [Z_{kk}] & [Z_{kl}] \\ [0] & 0 \\ [Z_{lk}] & [Z_{ll}] \\ [Z_{mk}] & [Z_{ml}] \end{bmatrix} \begin{bmatrix} \dot{\mathbf{d}}_k \\ \dot{d_l} \end{bmatrix} + \begin{bmatrix} [K_{kk}] & [K_{kl}] \\ [0] & 0 \\ [K_{lk}] & [K_{ll}] \\ [K_{mk}] & [K_{ml}] \end{bmatrix} \begin{bmatrix} \mathbf{d}_k \\ d_l \end{bmatrix} = ...$$

$$... \begin{bmatrix} [X_k] \\ [0] \\ [X_l] \\ [X_m] \end{bmatrix} \mathbf{u} \tag{D.45}$$

If this is written as:

$$\begin{bmatrix} [M_1] & \mathbf{0} & \mathbf{0} \\ [M_3] & 1 & 0 \\ [M_{3'}] & 0 & 1 \end{bmatrix} \begin{bmatrix} \ddot{\mathbf{d}} \\ f_N \\ f_D \end{bmatrix} + \begin{bmatrix} [Z_1] \\ [Z_2] \\ [Z_{2'}] \end{bmatrix} \dot{\mathbf{d}} + \begin{bmatrix} [K_1] \\ [K_2] \\ [K_{2'}] \end{bmatrix} \mathbf{d} = \begin{bmatrix} [X_1] \\ [X_2] \\ [X_{2'}] \end{bmatrix} \mathbf{u} \tag{D.46}$$

with $\mathbf{d}$ again the vector of displacements k and l, then the following results:

$$[M_1]\,\ddot{\mathbf{d}} + [Z_1]\,\dot{\mathbf{d}} + [K_1]\,\mathbf{d} = [X_1]\,\mathbf{u}$$

$$\left[M^{stick'}\right]\ddot{\mathbf{d}} + \left[Z^{stick'}\right]\dot{\mathbf{d}} + \left[K^{stick'}\right]\mathbf{d} = \left[X^{stick'}\right]\mathbf{u} \tag{D.47}$$

And in the same way as before:

$$f_N = \left([M_3]\left[M^{stick'}\right]^{-1}\left[Z^{stick'}\right] - [Z_2]\right)\dot{\mathbf{d}} + \left([M_3]\left[M^{stickp'}\right]^{-1}\left[K^{stick'}\right] - [K_2]\right)\mathbf{d} + ...$$

$$... \left([X_2] - [M_3]\left[M^{stick'}\right]^{-1}\left[X^{stick'}\right]\right)\mathbf{u} = ...$$

$$... \left[C_N^{stick'}\right]\begin{bmatrix} \mathbf{d} \\ \dot{\mathbf{d}} \end{bmatrix} + \left[D_N^{stick'}\right]\mathbf{u} \tag{D.48}$$

$$f_D = \left([M_{3'}]\left[M^{stick'}\right]^{-1}\left[Z^{stick'}\right] - [Z_{2'}]\right)\dot{\mathbf{d}} + \left([M_{3'}]\left[M^{stickp'}\right]^{-1}\left[K^{stick'}\right] - [K_{2'}]\right)\mathbf{d} + ...$$

$$... \left([X_{2'}] - [M_{3'}]\left[M^{stick'}\right]^{-1}\left[X^{stick'}\right]\right)\mathbf{u} = ...$$

$$... \left[C_D^{stick'}\right]\begin{bmatrix} \mathbf{d} \\ \dot{\mathbf{d}} \end{bmatrix} + \left[D_D^{stick'}\right]\mathbf{u} \tag{D.49}$$

D.3.3 Equations of motion including slider displacement

Equations of motion for slip state Again the relationship between normal and tangential force in the positive slip state is:

$$f_D = \mu f_N \tag{D.50}$$

Using Equations D.37 and D.50, the force term on the right hand side of Equation D.36 is rewritten:

$$\begin{bmatrix} \mathbf{0} \\ -f_D \\ -f_N \end{bmatrix} = -m_{sl} \begin{bmatrix} \mathbf{0} \\ 1 \\ \frac{1}{\mu} \end{bmatrix} \ddot{d}_{sl} + \begin{bmatrix} \mathbf{0} \\ 1 \\ \frac{1}{\mu} \end{bmatrix} f_{sf} \tag{D.51}$$

If the first term is moved to the left hand side of the equations the following results:

$$\begin{bmatrix} [M_{kk}] & [M_{kl}] & \{0\} \\ [M_{lk}] & [M_{ll}] & m_{sl} \\ [M_{mk}] & [M_{ml}] & \frac{1}{\mu} m_{sl} \end{bmatrix} \begin{bmatrix} \ddot{\mathbf{d}}_k \\ \ddot{d}_l \\ \ddot{d}_{sl} \end{bmatrix} + \begin{bmatrix} [Z_{kk}] & [Z_{kl}] \\ [Z_{lk}] & [Z_{ll}] \\ [Z_{mk}] & [Z_{ml}] \end{bmatrix} \begin{bmatrix} \dot{\mathbf{d}}_k \\ \dot{d}_l \end{bmatrix} + \begin{bmatrix} [K_{kk}] & [K_{kl}] \\ [K_{lk}] & [K_{ll}] \\ [K_{mk}] & [K_{ml}] \end{bmatrix} \begin{bmatrix} \mathbf{d}_k \\ d_l \end{bmatrix} = ...$$

$$... \begin{bmatrix} [X_k] & \mathbf{0} \\ [X_l] & 1 \\ [X_m] & \frac{1}{\mu} \end{bmatrix} \begin{bmatrix} \mathbf{u} \\ f_{sf} \end{bmatrix} \tag{D.52}$$

This is a set of equations with as much as equations as unknowns (the acceleration terms) and is solved using numerical integration. The equations can be written as:

$$\left[M^{slip+}\right] \ddot{\mathbf{d}} + \left[Z^{slip}\right] \dot{\mathbf{d}} + \left[K^{slip}\right] \mathbf{d} = \left[X^{slip+}\right] \mathbf{u}' \tag{D.53}$$

With $\mathbf{d}$ the degrees of freedom and $\mathbf{u}'$ the new input vector:

$$\mathbf{d} = \begin{bmatrix} \mathbf{d}_k \\ d_l \\ d_{sl} \end{bmatrix}, \quad \mathbf{u}' = \begin{bmatrix} f_{ps} \\ V_b \\ V_l \\ f_{sf} \end{bmatrix} \tag{D.54}$$

Note that for slipping in the reverse direction the terms containing μ in the M and X matrices change sign while the rest of the equations stays the same.

To obtain the contact forces f_D and f_N, some algebraic rewriting of Equations D.37 and D.52 is done. This leads to the following:

$$f_D = m_{sl}\ddot{d}_{sl} - f_{sf} = m_{sl} \left[N^{\delta}\right] \ddot{\mathbf{d}} - \left[N^{u}\right] \mathbf{u}' = ...$$

$$... - m_{sl} \left[N^{\delta}\right] \left[M^{slip+}\right]^{-1} \left[Z^{slip}\right] \dot{\mathbf{d}} - m_{sl} \left[N^{\delta}\right] \left[M^{slip+}\right]^{-1} \left[K^{slip}\right] \mathbf{d} + ...$$

$$... \left[m_{sl} \left[N^{\delta}\right] \left[M^{slip+}\right]^{-1} \left[X^{slip}\right] - \left[N^{u}\right]\right] \mathbf{u}' \tag{D.55}$$

where $\left[N^{\delta}\right]$ and $[N^u]$ are resp. $1 \times (n_k + 2)$ and 1×4 matrices with a one on the index corresponding to resp. the slider displacement in $\mathbf{d}$ and stage friction in $\mathbf{u}'$. The above can be written as:

$$f_D = \left[C_D^{slip}\right] \begin{bmatrix} \mathbf{d} \\ \dot{\mathbf{d}} \end{bmatrix} + \left[D_D^{slip}\right] \mathbf{u}' \tag{D.56}$$

Equations of motion for stick state In the stick state, there is no explicit relation between the normal and traction force in the contact point. Therefore the third line in Equation D.36 can be removed. Again the f_D term on the right hand side is expressed in terms of $\ddot{d}_{sl}$ and f_{sf} according to Equation D.37, and an extra row is added for the sticking condition: $\ddot{d}_{sl} = \ddot{d}_l$. Then the following remains:

$$\begin{bmatrix} [M_{kk}] & [M_{kl}] & \mathbf{0} \\ [M_{lk}] & [M_{ll}] & m_{sl} \\ [0] & -1 & 1 \end{bmatrix} \begin{bmatrix} \ddot{\mathbf{d}}_k \\ \ddot{d}_l \\ \ddot{d}_{sl} \end{bmatrix} + \begin{bmatrix} [Z_{kk}] & [Z_{kl}] \\ [Z_{lk}] & [Z_{ll}] \\ [0] & 0 \end{bmatrix} \begin{bmatrix} \dot{\mathbf{d}}_k \\ \dot{d}_l \end{bmatrix} + \begin{bmatrix} [K_{kk}] & [K_{kl}] \\ [K_{lk}] & [K_{ll}] \\ [0] & 0 \end{bmatrix} \begin{bmatrix} \mathbf{d}_k \\ d_l \end{bmatrix} = ...$$

$$... \begin{bmatrix} [X_k] \\ [X_l] \\ [0] \end{bmatrix} \mathbf{u} + \begin{bmatrix} \mathbf{0} \\ f_{sf} \\ 0 \end{bmatrix} \tag{D.57}$$

It is possible to write the equations such that d_{sl} is not a degree of freedom of the model, but the above notation is preferred because then the degrees of freedom are the same as in the slip state, which makes it easier when numerical integration is performed.

In the same way as before, the system is written as:

$$\left[M^{stick}\right] \ddot{\mathbf{d}} + \left[Z^{stick}\right] \dot{\mathbf{d}} + \left[K^{stick}\right] \mathbf{d} = \left[X^{stick}\right] \mathbf{u}' \tag{D.58}$$

The expression for f_D is derived in analogy to before in the slip state. The expression for f_N is derived from Equation D.36:

$$f_N = -M_1 \ddot{\mathbf{d}} - Z_1 \dot{\mathbf{d}} - K_1 \mathbf{d} + X_1 \mathbf{u}' \tag{D.59}$$

where in this case $[M_1] = \begin{bmatrix} [M_{mk}] & [M_{ml}] & 0 \end{bmatrix}$, the same for $[Z_1]$ and $[K_1]$, and $[X_1] = \begin{bmatrix} [X_m] & 0 \end{bmatrix}$

$$f_N = \left([M_1] \left[M^{stick}\right]^{-1} \left[Z^{stick}\right] - [Z_1] \right) \dot{\mathbf{d}} + \left([M_1] \left[M^{stick}\right]^{-1} \left[K^{stick}\right] - [K_1] \right) \mathbf{d} + ...$$

$$... \left([X_1] - [M_1] \left[M^{stick}\right]^{-1} \left[X^{stick}\right] \right) \mathbf{u}' \tag{D.60}$$

This leads to again the same form as before:

$$f_N = \left[C_N^{stick}\right] \begin{bmatrix} \mathbf{d} \\ \dot{\mathbf{d}} \end{bmatrix} + \left[D_N^{stick}\right] \mathbf{u}'$$

$$f_D = \left[C_D^{stick}\right] \begin{bmatrix} \mathbf{d} \\ \dot{\mathbf{d}} \end{bmatrix} + \left[D_D^{stick}\right] \mathbf{u}' \tag{D.61}$$

D.4 Solving the model

To solve the model and simulate the motion of the motor and slider, the system of equations is built in MatLab in the same way as described in the previous sections. What results is three sets of equations: Equation D.53 for the slip state and its equivalent for the reverse slip state, and Equation D.58 for the slip state. Because each of the three time systems of equations describe the dynamics of the model in one of its phases, for each time step the solver should know in which phase the model is at that moment (if it sticks, slips in positive direction or in negative) to determine which set of equations to use for the next time step. Three ways were found to do this, each of which will be described briefly.

D.4.1 Piecewise integration

The most straightforward way to deal with the different phases is to perform time integration in an normal way for a certain phase until a 'transition point' is reached at which the model switches to a different phase. At that point the solver stops and a new integration run is started using the equations of motion for the new phase, with the end state of the previous run as initial conditions.

The transition points are as follows:

- When in positive or negative slip phase, the finger will (at least try to) stick when the relative velocity in the contact point decreases to zero. Therefore for the slip phases the transition point is the following:

$$\dot{d}_{sl} - \dot{d}_l = 0 \tag{D.62}$$

- When in stick phase, the finger will break loose from the strip when the traction force exceeds the maximum possible, namely the friction coefficient times the normal force, so the transition point from stick to slip is defined as:

$$|f_D| = \mu f_N \tag{D.63}$$

  Here the sign of f_D determines if transition is to positive or to negative slip.

Due to the finite step size in numerical integration, the transition points will never be exactly reached. Therefore the solver detects when the transition points are crossed, and then uses an iterative process to approach to the point itself until it is reached within a certain tolerance. In stick phase, Equations D.61 are used to evaluate the contact forces.

D.4.2 Piecewise integration with Hénon's algorithm

This method is basically the same as the previous, but now a different algorithm is used to approach the transition point after the transition is detected. This method is based on the following reasoning. Originally there is a system that is described by:

$$\dot{\mathbf{q}} = f(\mathbf{q}, t) \tag{D.64}$$

where $\mathbf{q}$ is a vector of states and f the functions that describe the dynamics. Now if a transition takes place when $q_s = 0$, where q_s is an arbitrary state in $\mathbf{q}$, and the rest of the states are called $\mathbf{q}_p$, a new system can be defined, in which the variable q_s 'switches position' with the time variable t:

$$\dot{\mathbf{y}} = g(\mathbf{y}, q_s), \;\; \mathbf{y} = \begin{bmatrix} \mathbf{q}_p \\ t \end{bmatrix} \tag{D.65}$$

Here the prime now denotes the derivative to q_s instead of the time derivative, and g is a new set of functions describing the 'inverse dynamics' that can be directly derived from the original f:

$$\dot{\mathbf{y}} = \begin{bmatrix} d\mathbf{q}_p/dq_s \\ dt/dq_s \end{bmatrix} = \frac{1}{dq_s/dt} \begin{bmatrix} d\mathbf{q}_p/dt \\ 1 \end{bmatrix} = \frac{1}{f_s(\mathbf{q}, t)} \begin{bmatrix} f_p(\mathbf{q}, t) \\ 1 \end{bmatrix} = g(\mathbf{y}, q_s) \tag{D.66}$$

With the new system integration steps can be taken in which not t but q_s is prescribed. A single integration step to $q_s = 0$ then gives the time t and state $\mathbf{q}$ at the transition moment with an accuracy defined by the numerical integration scheme. The advantage of this method is that only one integration step is needed to approach the transition point, instead of the slower iterative process used in the previous method. However, in practice it turned out that since the transitions from one to another state occur only now and then, this didn't noticeably contribute to the speed of the complete process, while the drawback is that it couldn't easily be integrated with existing numerical integration functions in MatLab. Therefore in the end this method was not used in the simulations.

D.4.3 Continuous model

As an alternative to the algorithm of the previous paragraphs, a continuous relation between the friction coefficient and relative velocity can be used. The ideal Coulomb friction model can be approached with a continuous function, for instance the arctan function:

$$\mu = -\frac{\pi}{2}\mu_c \arctan\left(c\left(\dot{d}_l - \dot{d}_{sl}\right)\right) \tag{D.67}$$

Here c is a constant determining the steepness of the approximation and μ_c is the friction coefficient used in the coulomb model. Now the normal force is an explicit function of the relative velocity and therefore the system can be solved at any time step using only the slip equations as in Equation D.52.

The obvious advantage is that switching between the two states, is not necessary anymore. However, this method has two main disadvantages:

- The system is not linear anymore because the M-matrix contains μ, which is now a non-linear function of the states.
- The system is very stiff in the area around the zero relative velocity since the arctan function is very steep around 0. Stiff systems in general lead to small time steps and thus a slow integration process, which was indeed observed when this method was used to solve the system with various in-built MatLab solvers. The less steep the arctan function is made, the faster the process but the less accurate the real stick state will be approximated.

When multiple contact nodes would be used, with piecewise integration the problem would arise that the different nodes won't necessarily have their phase transitions exactly at the same time, leading to a large number of transition instants and sets of equations. Then the continuous method could be preferable because it would easily be able to determine the friction force in each of the contact nodes individually and it never changes the system equations. However, since a single contact point is assumed in this research and regarding the above disadvantages of the continuous method, the piecewise method is used for the simulations.

D.5 Postprocessing

D.5.1 Energy transfer and dissipation

Of the electrical power that is put into the system, a part is effectively transferred to the slider, while the rest is dissipated in three different mechanisms: friction in the contact area, mechanical damping and dielectric loss.

Effective power transfer The power effectively transferred to the slider is used to overcome the slider friction and to accelerate the stage. Therefore, for a certain solver step n, the effective power is given by:

$$\dot{q}_{eff} = \left| f_{sf} \dot{d}_{sl} \right| + m_{sl} \dot{d}_{sl} \ddot{d}_{sl} \tag{D.68}$$

Dissipation in contact area The dissipated power in the contact area is given by:

$$\dot{q}_{cl} = \left| f_D \left(\dot{d}_{tip} - \dot{d}_{sl} \right) \right| \tag{D.69}$$

Of course this is zero in the stick phase.

Dissipation due to material damping Mechanical damping is mathematically described with the damping matrix $[Z]$. The dissipated power as a result of this mechanical damping is by definition given by:

$$\dot{q}_{ml} = \dot{\mathbf{d}}^T [Z] \dot{\mathbf{d}} \tag{D.70}$$

And for individual elements:

$$\dot{q}_{ml}^{(e)} = \left(\dot{\mathbf{d}}^{(e)} \right)^T [Z]^{(e)} \dot{\mathbf{d}}^{(e)} \tag{D.71}$$

where $\mathbf{d}^{(e)}$ is the 6×1 vector of displacements of the three nodes defining the element, and $[Z]^{(e)}$ the elemental damping matrix.

Dissipation due to dielectric loss The dielectric loss in piezoelectric material is usually described by describing the capacitance of the piezoelectric system as a combination of a real and complex part:

$$C = C' - jC'' \tag{D.72}$$

The ratio between real and complex part is given by a loss factor tan δ:

$$\tan\delta = \frac{C''}{C'} \tag{D.73}$$

This can be applied to the basic rules of electricity:

$$Z_C = \frac{1}{j\omega C} = \frac{U}{I} \tag{D.74}$$

$$P_C = UI = \frac{U^2}{Z_C} = U^2 j\omega C'(1 - j \cdot \tan\delta) \tag{D.75}$$

Here P_C is the complex electrical power through the capacitor, of which the real part is the dissipated power due to dielectric loss:

$$P'_C = \tan\delta \cdot U^2 \omega C \tag{D.76}$$

For an ideal capacitor with two parallel plates, the capacitance C is given by:

$$C = \varepsilon_r \varepsilon_0 \frac{A}{d} \tag{D.77}$$

where $\varepsilon_r\varepsilon_0$ is the electric permittivity of the material, A the surface area of the electrodes and d the distance of the electrodes.

Therefore, if the inputs V_A and V_B of the model are harmonic signals with frequency F_d and RMS-value $\bar{V}_A$ and $\bar{V}_B$, then the power dissipation in an element on electrode 1 or 4 is given by:

$$\dot{q}_{dl}^{(e)} = \tan\delta \cdot 2\pi F_d \bar{V}_A^2 \varepsilon_z \varepsilon_0 \frac{A^{(e)}}{t} \tag{D.78}$$

and likewise with $\bar{V}_B$ for elements on electrodes 3 and 4. Here tanδ and ε_z are resp. the dielectric loss factor and relative permittivity in z-direction of the piezo-material, $A^{(e)}$ the surface area of the element and t the thickness of the body.

Appendix E

Extended resonance analysis

In this appendix the possible influence of the support structure on the resonance of the piezo-body is investigated. A mesh with 469 linear triangular elements is used in this analysis, the same as used for the simulations in the main part of the report. The second bending resonance of the entirely free (unsupported) body is 49.6 kHz. In the simulations the support was modeled as springs with stiffness $1 \cdot 10^6$ N/m connecting each of the four contact points to the fixed world, which didn't significantly influence the resonance shape and frequency.

E.1 Influence of support parameters on resonance frequency

To investigate the influence of the support structure on the resonance of the body, the support structure is modeled in two different ways:

1. 'Spring support': each of the four support nodes is connected to the fixed world with a spring with stiffness k, as is done in the simulations.
2. 'Mass support': the support is modeled by a point mass m fixed to each of the support nodes.

Spring support Figure E.1a shows the influence of the spring stiffness k on the resonance frequencies. Two different resonance modes are shown:

- The first resonance converges at low stiffness to the second bending mode of the unsupported body at 49.6 kHz. For increasing stiffness, the frequency of this resonance increases and the mode shape changes.
- The second resonance corresponds at low stiffness to a rigid-body displacement. For increasing stiffness, the frequency increases to about 44 kHz and the mode shape looks more and more like the second bending mode of the unsupported body.

Mass support Figure E.1b shows the influence of the mass m in the support points on the resonance frequency. For low mass, the resonance converges to the second bending mode of the unsupported body at 49.6 kHz. For high mass, the resonance converges to the same as 'resonance 2' in case of spring support in Figure E.1a. This is explained by the fact 'infinite mass' and 'infinite stiffness' are both the same situation, namely a fixed constraint to the support nodes.

E.2 Input sensitivity at different support parameters

In Figure E.2 the transfer from model input V_A to the tip displacement d_{tip} is shown for the supported body without contact in the finger for several support parameters:

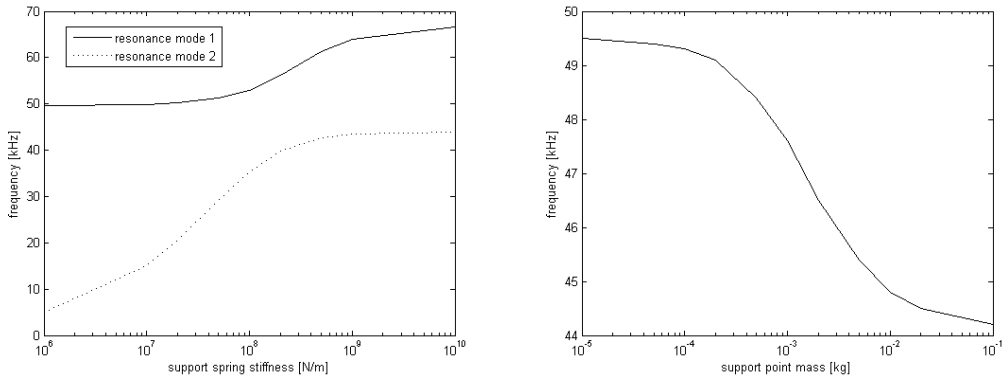

(a) (b)

Figure E.1: Influence of support model on resonance frequency: (a) resonance frequency against support stiffness for 'spring support'; (b) resonance frequency against support mass for 'mass support'.

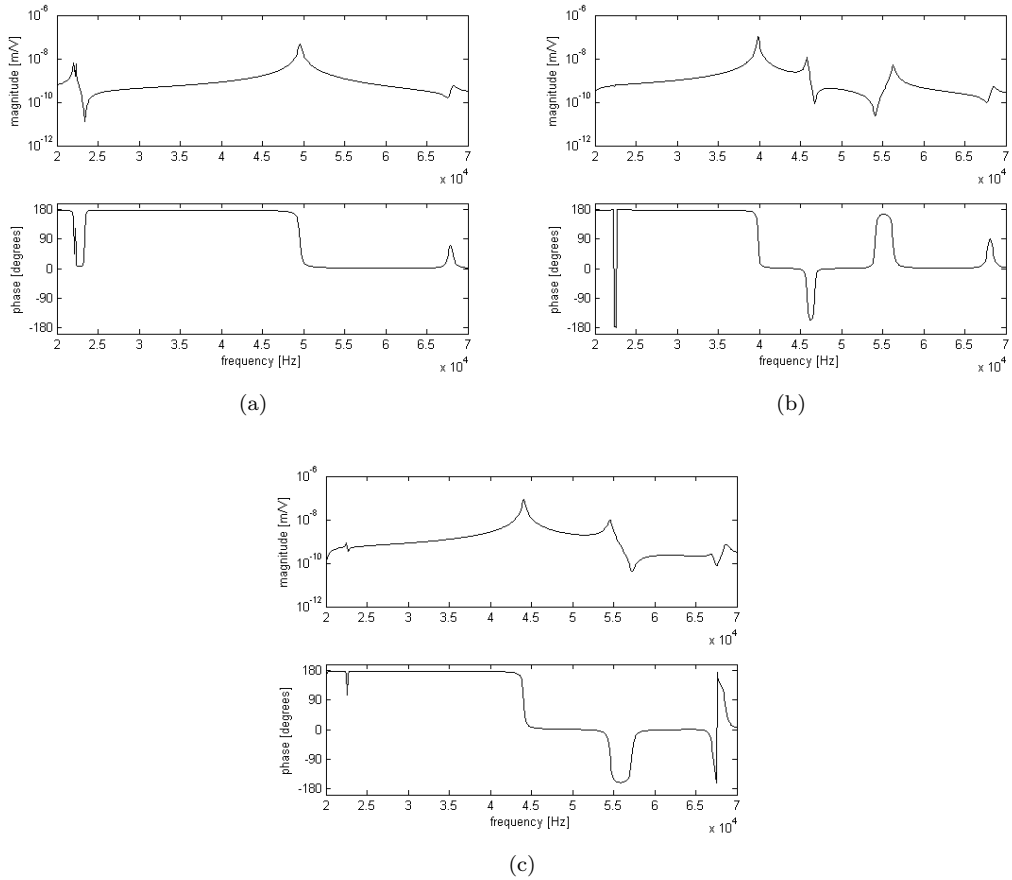

(a) (b)

(c)

Figure E.2: Frequency response of transfer from motor input voltage V_A to tip displacement d_{tip} for (a) no support, (b) spring support with support stiffness $k = 2 \cdot 10^8$ and (c) fixed support.

1. No support (corresponding with spring support or mass support with zero stiffness or mass)
2. Spring support with $k = 2 \cdot 10^8$
3. Fixed support (corresponding with spring support or mass support with infinite stiffness or mass)

For the unsupported body (Figure E.2a), the resonance at 49.6 kHz is clearly visible in the transfer. For fixed support (Figure E.2c), the resonance at 44 kHz (resonance 2 in Figure E.1a for infinite stiffness or the resonance in Figure E.1b for infinite mass) is clearly visible, while the resonance at 68 kHz (resonance 1 in Figure E.1a for infinite stiffness) is visible, but not very dominant. For spring support with $k = 2 \cdot 10^8$ (Figure E.2b), resonances are visible at a.o. 40 and 56 kHz, corresponding to the two resonances in Figure E.1a.

E.3 Conclusion

With the above analysis it is shown that the model of the support structure has significant influence on the resonances of the system, even when the support is modeled with only linear springs or point masses. It is shown that for certain parameters for the support model, the finger tip is effectively excited in resonance at frequencies lower than the 49.6 kHz of the second bending mode of the unsupported body.

Bibliography

[1] R. H. Munnig Schmidt, G. Schitter, and J. van Eijk, *High Performance Mechatronics*, ch. 1,9. IOS Press, 2011.

[2] http://www.mapperlithography.com/.

[3] T. Kunioka, Y. Takeda, T. Matsuda, N. Shimazu, and Y. Nakayama, "Xy stage driven by ultrasonic linear motors for the electron-beam x-ray mask writer eb-x3," *Journal of Vacuum Science and Technology B*, vol. 17, pp. 2917–2920, nov/dec 1999.

[4] Y. A. Deulin, V. P. Michailov, and A. V. Usov, "New type of clean precise high vacuum drive, based on magnetic and dielectric liquids rheology," *Vacuum*, vol. 44, no. 5-7, pp. 469–470, 1993.

[5] T. Hemsel and J. Wallaschek, "Survey of the present state of the art of piezoelectric linear motors," *Ultrasonics*, vol. 38, pp. 37–40, mar 2000.

[6] http://www.nanomotion.com/.

[7] E. A. Deulin, V. P. Mikhailov, Y. V. Panfilov, and R. A. Nevshupa, *Mechanics and Physics of Precise Vacuum Mechanisms*. Springer, 2010.

[8] http://www.vgscienta.com/.

[9] http://www.nsk.com/.

[10] T. G. King, M. E. Preston, B. J. M. Murphy, and D. S. Cannell, "Piezoelectric ceramic actuators: A review of machinery applications," *Precision Engineering*, vol. 12, pp. 131–136, jul 1990.

[11] http://www.piceramic.com/piezo_materials_1.

[12] M. Hermann and W. Schinköthe, "Piezoelectric travelling wave motors generating direct linear motion," in *Proceedings International Conference New Actuators*, (Bremen), pp. 200–203, jun 1996.

[13] K. Uchino, "Piezoelectric ultrasonic motors: an overview," *Smart Material Structures*, vol. 7, no. 3, pp. 273–285, 1998.

[14] http://www.physikinstrumente.com/.

[15] E. Shamoto and T. Moriwaki, "Rigid xyθ table for ultraprecision machine tool driven by means of walking drive," *CIRP Annals - Manufacturing Technology*, vol. 46, no. 1, pp. 301–304, 1997.

[16] S. DeVos, *Development of fast, stiff and high-resolution piezoelectric motors with integrated bearing-driving functionality*. PhD thesis, Katholieke Universiteit Leuven, feb 2006.

[17] T. Yamaguchi, K. Adachi, Y. Ishimine, and K. Kato, "Wear mode control of drive tip of ultrasonic motor for precision positioning," *Wear*, vol. 256, pp. 145–152, 2004.

[18] K. Kosaka, "Wear reduction method for frictionally fast feeding piezoactuator," *Japanese Journal of Applied Physics*, vol. 45, no. 2A, pp. 1005–1011, 2006.

[19] P. Rehbein and J. wallaschek, "Friction and wear behavior of polymer/steel and alumina/alumina under high-frequency fretting conditions," *Wear*, vol. 216, pp. 97–105, 1998.

[20] T. Ishii, S. Ueha, K. Nakamura, and K. Ohnishi, "Wear properties and life prediction of frictional materials for ultrasonic motors," *Japanese Journal of Applied Physics*, vol. 34, pp. 2765–2770, may 1995.

[21] T. Ishii, H. Takahashi, K. Nakamura, and S. Ueha, "A low-wear driving method of ultrasonic motors," *Japanese Journal of Applied Physics*, vol. 38, pp. 3338–3341, may 1999.

[22] J. Wallaschek, "Contact mechanics of piezoelectric ultrasonic motors," *Smart Material Structures*, vol. 7, no. 3, pp. 369–381, 1998.

[23] Y. Tomikawa, M. Yaginuma, S. Hirose, and T. Takano, "An equivalent circuit expression of an ultrasonic motor and measurement of its elements," *Japanese Journal of Applied Physics*, vol. 30, pp. 2398–2401, sep 1991.

[24] M. Aoyagi and Y. Tomikawa, "Simplified equivalent circuit of ultraonic motor and its application to estimation of motor characteristics," *Japanese Journal of Applied Physics*, vol. 34, pp. 2752–2755, may 1995.

[25] M. Houben, "A generic modelling approach for studying the contact mechanism and dynamic behavior of bimodal standing wave piezomotors," in *Proceedings of the euspen International Conference*, may 2008.

[26] R. H. Munnig Schmidt, G. Schitter, and J. van Eijk, *High Performance Mechatronics*, ch. 5, p. 299. IOS Press, 2011.

[27] D. V. Hutton, *Fundamentals of Finite Element Analysis*. McGraw - Hill, 1 ed., 2004.

[28] G. Nader, E. C. N. Silva, and J. C. Adamowski, "Effective damping value of piezoelectric transducer determined by expirimental techniques and numerical analysis," *ABCM Symposium Series in Mechatronics*, vol. 1, pp. 271–279, 2004.

[29] http://www.directindustry.com/prod/anorad/vacuum-compatible-linear-electric-motors-ironless-11763-423359.html.

[30] V. Anisimov, E. Deulin, V. Mikhailov, V. Kasperski, and V. Sytchev, "New high precision magnetic rheology drives for segmented primary mirror of adaptive telescope," *Proceedings of SPIE*, vol. 2871, pp. 641–648, mar 1997.

[31] V. Mikhailov, D. Borin, A. Bazinenkov, and I. Akimov, "Positioning magnetorheological actuator," *Journal of Physics: Conference Series*, vol. 149, no. 1, pp. 1–4, 2009.

[32] http://www.www.pfeiffer-vacuum.de.com/.

[33] Y. Hayashi and T. Yamada, "Development of the harmonic drive rotary feedtrhough," *Vacuum*, vol. 41, no. 7-9, pp. 1948–1950, 1990.

[34] W. Ochonski, "Dynamic sealing with magnetic fluids," *Wear*, vol. 130, pp. 261–268, mar 1989.

[35] I. Anton, I. de Sabata, L. Vékás, E. Potencz, and E. Suciu, "Magnetic fluid seals: some design problems and applications," *Journal of Magnetism and Magnetic Materials*, vol. 65, pp. 379–381, mar 1987.

[36] http://www.telemark.com/.

[37] G. Pritschow, "A comparison of linear and conventional electromechanical drives," *Annals of the CIRP*, vol. 47, no. 2, pp. 541–548, 1998.

[38] M. Versteyhe, *Development of an ultra-stiff piezo stepper with nanometer resolution.* PhD thesis, Katholieke Universiteit Leuven, may 2000.

[39] http://www.wittenstein-rack-pinion.com/.

[40] http://www.schlenkent.com/.

[41] http://www.schneeberger.com/.

[42] J. R. Moser and R. F. Spencer, jr., "Predicting the magnetic fields from a twisted-pair cable," *IEEE Transactions on Electromagnetic Compatibility*, vol. 10, pp. 324–329, sep 1968.

[43] Garcia, "Non-magnetic system for a memory disk test system." U.S. Patent nr. 6344738, feb 2002.

[44] http://www.mumetal.co.uk/.

[45] A. J. Mager, "Magnetic shields," *IEEE Transactions on Magnetics*, vol. 6, pp. 67–75, mar 1970.

[46] Y. Y. Reutov, "Physical interpretation of magnetostatic shielding," *Russian Journal of Nondestructive Testing*, vol. 36, no. 2, pp. 55–67, 2000.

[47] J. A. Kerns, A. del LaPaz, and J. Fabyan, "Magnetic shielding design analysis," Conference 10, Lawrence Livermore National Lab., CA (USA), dec 1983.

[48] M. Reta-Hernández and G. G. Karady, "Attenuation of low frequency magnetic fields using active shielding," *Electric Power Systems Research*, vol. 45, pp. 57–63, apr 1998.